PHYSIK-DEPARTMENT

DEGRADATION MECHANISMS OF PEROVSKITE SOLAR CELLS

Dissertation
von

RENJUN GUO

TECHNISCHE UNIVERSITÄT
MÜNCHEN

TECHNISCHE UNIVERSITÄT MÜNCHEN

Fakultät für Physik

DEGRADATION MECHANISMS OF PEROVSKITE SOLAR CELLS

RENJUN GUO

Vollständiger Abdruck der von der Fakultät für Physik der Technischen Universität München zur Erlangung des akademischen Grades eines

Doktors der Naturwissenschaften (Dr. rer. nat.)

genehmigten Dissertation.

Vorsitzender:	Prof. Dr. David Egger
Prüfer der Dissertation:	1. Prof. Dr. Peter Müller-Buschbaum
	2. Prof. Dr. Ian D. Sharp

Die Dissertation wurde am 19.07.2022 bei der Technischen Universität München eingereicht und durch die Fakultät für Physik am 06.09.2022 angenommen.

Abstract

Metal halide perovskites have shown a promising future for applications in field-effect transistors, light-emitting diodes, sensors, solar cells and photo-detectors due to their excellent optic-electrical properties. The excellent properties of perovskites, for example, strong absorption, the long diffusion length of photo-generated charge carriers and low binding energies make it possible to realize next-generation solar cells with 25.7 % power conversion efficiency (PCE) in a decade. At the same time, perovskite solar cells (PSCs) have shown a powerful photovoltaic application for replacing silicon solar cells not only due to high PCE but also because of their low processing costs. However, long-term stability is a challenging issue for the commercialization of PSCs. So far, using sealing technologies industrialized for organic electronics can suppress extrinsic factors such as oxygen and water-induced degradation of PSCs. However, intrinsic factors like heat and light-induced degradation under the real operation of PSCs cannot be avoided and will still cause degradation of PSCs. This thesis aims to figure out the fundamental degradation mechanisms of PSCs under operational conditions, which can be used for designing strategies to improve the long-term stability of PSCs.

Zusammenfassung

Metallhalogenid-Perowskite haben aufgrund ihrer hervorragenden optisch-elektrischen Eigenschaften eine vielversprechende Zukunft für Anwendungen in Feldeffekttransistoren, Leuchtdioden, Sensoren, Solarzellen und Fotodetektoren. Zu den hervorragenden Eigenschaften von Perowskiten zählen beispielsweise die starke Absorption, die lange Diffusionslänge photogenerierter Ladungsträger und niedrige Bindungsenergien, die es ermöglichen, Solarzellen der nächsten Generation mit 25,7 % Leistungsumwandlungseffizienz (PCE) in einem Jahrzehnt zu realisieren. Gleichzeitig haben sich Perowskit-Solarzellen (PSCs) als leistungsstarke photovoltaische Anwendung zum Ersatz von Silizium-Solarzellen erwiesen, nicht nur aufgrund der hohen PCE, sondern auch wegen ihrer geringen Verarbeitungskosten. Die Langzeitstabilität ist jedoch eine Herausforderung für die Kommerzialisierung von PSCs. Bisher können durch den Einsatz der für die organische Elektronik industrialisierten Versiegelungstechnologien extrinsische Faktoren wie der durch Sauerstoff und Wasser induzierte Abbau von PSCs unterdrückt werden. Intrinsische Faktoren wie wärme- und lichtinduzierte Degradation unter dem realen Betrieb von PSCs können jedoch nicht vermieden werden und werden immer noch eine Degradation von PSCs verursachen. Diese Arbeit zielt darauf ab, die grundlegenden Degradationsmechanismen von PSCs unter Betriebsbedingungen herauszufinden, die für

die Entwicklung von Strategien zur Verbesserung der Langzeitstabilität von PSCs verwendet werden können.

Contents

List of abbreviations

PbI_2	lead iodide
2D	two dimensional
BET	Brunauer-Emmett-Teller
CB	conduction band
CdTe	cadmium telluride
CIGS	copper indium gallium selenide
DA	decoupling approximation
DFT	density function theory
DI water	deionized water
DMSO	dimethyl sulfoxide
DSSC	dye-sensitized solar cell
DWBA	distorted wave Born approximation
EBL	electron blocking layer
EIA	effective interface approximation
EQE	external quantum efficiency
FF	fill factor
FTO	fluorine doped tin oxide, SnO_2:F
FWHM	full width at half maximum
GaAs	gallium arsenide
GISAXS	grazing incidence small angle x-ray scattering

GIWAXS	grazing incidence wide angle x-ray scattering
GIXS	grazing incidence x-ray scattering
HBL	hole blocking layer
HCl	hydrochloric acid
I-V	current-voltage characteristics
ISOS	International Summit on Organic Photovoltaic Stability
ITO	indium doped tin oxide
J-V	current intensity-voltage characteristics
LED	light emitting diode
Li-TFSI	lithium bis(trifluoromethane)-sulfonimide
LMA	local monodisperse approximation
MPPT	maximum power point tracking
OPTP	optical pump Terahertz probe
OPV	organic photovoltaic
PbS	lead sulfide
PCE	power conversion efficiency
PL	photoluminescence
PLQY	photoluminescence quantum yield
PSC	perovskite solar cell
PV	photovoltaic
QFLS	quasi-Fermi level splitting
SCAPS-1D	solar cell capacitance simulator- one dimension
SCLC	space-charge limited current
SDD	sample-detector distance

SEM	scanning electron microscopy
SLD	scattering length density
Spiro-OMeTAD	2,2',7,7'-tetrakis(N,N di- *p*-methoxyphenyl-amine)9,9'-spiro-bi-fluorene
TAS	transient absorption spectroscopy
TCO	transparent conductive oxide
TCSPC	time-correlated single photon counting
TRPL	time-resolved photoluminescence
UV/Vis	Ultra-violent/visible spectroscopy
VASP	Vienna Ab initio simulation package
VB	valence band
XPS	x-ray photoelectron spectroscopy
XRD	x-ray diffraction

1 Introduction

Climate change has been a global challenge in recent decades. Carbon dioxide emission is the key factor in worsening climate change. Developing renewable energies, especially for photovoltaic technologies, is the crucial strategy for suppressing the emission of CO_2.

Photovoltaics (PVs) have a few advantages: 1) the reliability and bank-ability of PV installation; 2) the compatibility of the grid infrastructure. Meanwhile, climate action plans call for 10 terawatts of PV by 2030. Thus, developing PV technology would be a critical way to realize such a goal. A number of solar cells will be introduced below.

For real-world applications of solar cells, the high PCE is the major parameter for decreasing the installation cost. Thus, a PCE competition for all kinds of solar cells is continuing once new types of solar cells are invented. Thus, the history of PCE development will be included. The discussion also includes the pros and cons of different types of solar cells.

The bandgap (1.12 eV) of silicon makes it an ideal material to harvest the sunlight spectrum from 250 nm to 1100 nm. A p-n junction made by p-type and n-type Si enables an efficient conversion from sunlight to electrical power. Through optimizing the device architecture and passivating contacts, the PCE of silicon solar cells has reached 26.7 % [1]. Currently, passivated emitter rear contacts, tunnel oxide passivated contacts, and heterojunction technologies dominate the mainstream of the global market for silicon solar cells. However, the low light absorption coefficient due to the nature of indirect semiconductors limits the application scenarios of such a photovoltaic technology. It is inevitable to use a thicker material (about 100 nm) to absorb sunlight totally, which restricts the possibility of reducing fabrication costs. Also, the high PCE of silicon solar cells needs a very high-quality silicon wafer, which also confines the possibility of a reduction in fabrication costs.

Gallium arsenide (GaAs) own the record efficiency of single-junction solar cells, which is 29.1 %. Such a direct band gap material with 1.42 eV has the best match for solar spectrum and a very high absorption coefficient. Compared with silicon solar cells, a

2 μm thin film can efficiently absorb all sunlight. However, the price of rare metal gallium restricts such solar cells for space application.

Cadmium telluride (CdTe) solar cells have an ideal bandgap (1.43 eV) and high light absorption, which produces a 21.0 % record efficiency. However, the toxicity of Cd and the insufficient Te on the earth prohibit a wide market share for such a technology [1].

Copper indium gallium selenide (CIGS) is a versatile material that can be fabricated by many techniques and installed in different forms. The bandgap of this material can be adjusted from 1.04 to 1.7 eV by modifying the ratio between indium and gallium. The record efficiency of CIGS is 23.35 % [1].

A dye-sensitized solar cell (DSSC) works as a photo-electrochemical cell, where the generation and transport of electrons are caused by the systematic factors of photon energy and chemical reactions. Dye-sensitized solar cells reach a certified record efficiency of 12.25 % [1].

Organic solar cells have achieved a certified PCE of 18.7 % due to the replacement of fullerene type acceptors with non-fullerene acceptors and their derivatives [2]. However, operating organic solar cells under operational conditions for the long term is the big barrier to bringing them to market.

Quantum dot solar cells have reached a certified PCE of 18.1 % due to the use of perovskite nanocrystals [3]. PbS quantum dot solar cells with a certified PCE of 13.8 % have the advantage of absorbing near-infrared sunlight which is not absorbed by other types of solar cells [4]. This offers a promising future for use in tandem solar cells to fully absorb the solar spectrum.

Hybrid perovskite materials are suited for a wide range of optoelectrical applications, including solar cells, light-emitting diodes, and photodetectors, due to their adjustable bandgap, low crystal formation energy, and high defect tolerance. Perovskite solar cells are also a viable technology for future large-scale applications and cheap manufacturing costs due to solution-based techniques and cost-effective ingredients. Perovskite solar cells reach equivalent performance compared to silicon solar cells because of dedicated research and global collaboration. Materials engineering using a two-step solution approach, solvent engineering and compositional engineering produce a power conversion efficiency of more than 20 %. Surface passivation and interfacial engineering have improved the performance of PSCs to 25.7 % [5].

One major barrier to the commercialization of PSCs is their long-term operational stability. To become a competitive technology such as silicon solar cells. The long-term operational stability of PSCs should maintain 90 % of their initial performance after 20 years of operation under real weather conditions (T90). However, the record T90 of PSCs only reached about 5000 hours under real-world conditions [6]. This is far away from 43800 sun-hours (6 sun-hours per day for 20 years). To meet this target, one has to figure out the degradation mechanisms of PSCs and propose possible strategies to improve long-term operational stability.

The other key challenge in the field is the reproducibility in different labs for fabricating highly efficient PSCs, and only a few organisations across the globe can generate devices with certified PCE $>$ 23 %. For the reproducibility of highly efficient PSCs, it is therefore critical to study the underlying limits throughout the manufacturing process.

To end up with these challenges, for this thesis, I aim to improve the reproducibility of device performance and dig the degradation mechanisms of PSCs under operational conditions. I structure this thesis in the following ways: After the introduction, the theoretical background of X-ray scattering and PSCs are introduced in chapter 2. Next, chapter 3 illustrates detailed device fabrication processes for this thesis. In chapter 4, all characterization methods related to this thesis are introduced. In chapter 5, I study how the two-dimensional polymorphs affect the optical properties, morphology, crystal orientation, charge carrier dynamics, and device reproducibilities. In chapter 6, I investigate the degradation mechanisms of perovskite solar cells operated under vacuum and a nitrogen atmosphere using synchrotron radiation-based operando grazing-incidence X-ray scattering methods. In addition, I find the water content in PbI_2 could affect the reproducibilities of PSCs dramatically as shown in chapter 7. Finally, the thesis is concluded by the obtained results in chapter 8.

2 Theoretical Background

This chapter contains the critical theories for understanding the topics discussed in this thesis. In Section 2.1, I discuss the basic concepts of X-ray scattering and the start-of-art scattering methods like GIWAXS and GISAXS. I also show the working principle for PSCs in Section 2.2.

2.1 X-ray Scattering

This section offers an introduction to X-ray scattering techniques for detecting crystal structures and morphologies. Basic concepts of X-ray scattering, X-ray diffraction, GIWAXS and GISAXS are introduced accordingly.

2.1.1 Basic Concepts

Grazing-incidence X-ray scattering (GIXS) methods, in particular, grazing-incidence wide- and small-angle X-ray scattering (GIWAXS, GISAXS), have shown to be an efficient technique for studying the morphology of thin films at various length scales. As a result, GIWAXS and GISAXS have been used in the rapidly evolving field of hybrid perovskites and play an important role in this thesis. Sections 2.1.2, and 2.1.3 provide a brief overview of GIWAXS and GISAXS, respectively. The scattering geometry is depicted schematically as shown in figure 2.1.

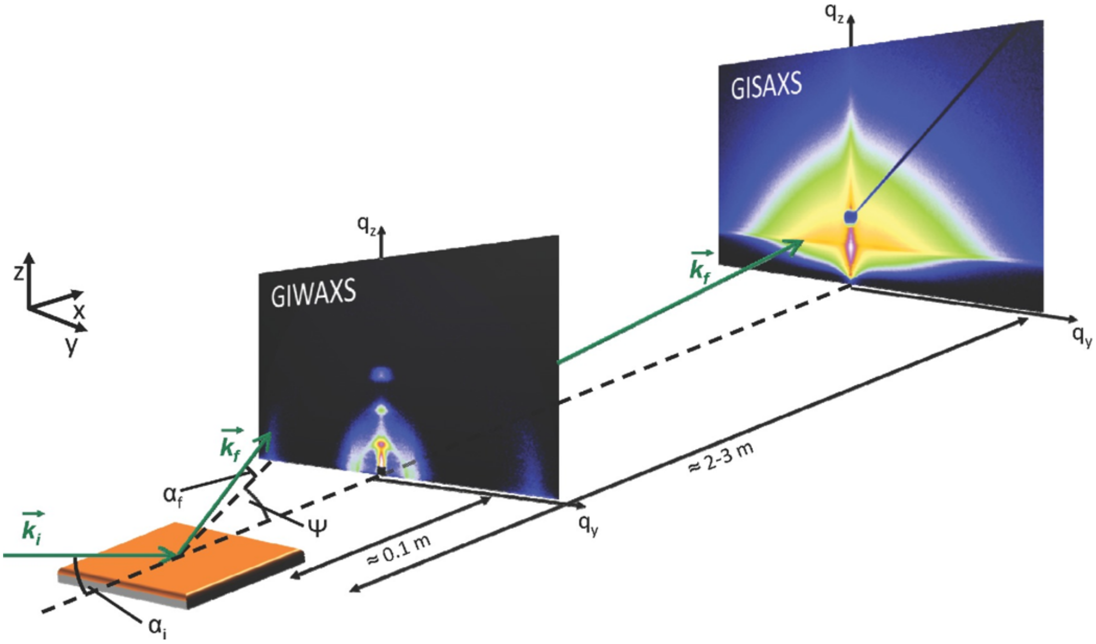

Figure 2.1: Schematic picture of the experimental set-up used in GISAXS or GIWAXS. The detection of diffuse scattering is done with a 2D detector. The sample surface is placed nearly horizontally, inclined by an incident angle α_i. The exit angle is denoted α_f and the out-of-plane angle ψ. The color coding visualizes differences in the scattered intensity. Typical sample-detector distances for GIWAXS and GISAXS are 0.1 m and 2-3 m. Reprinted with permission from [7]. Copyright 2014 Wiley.

The sample reference frame is positioned on the sample surface, pointing in the direction of the X-ray beam and z along the surface normal. The incident beam with $\overrightarrow{k}$ shoots on the sample at a very small angle α_i where α_i is typically smaller than 1° (for X-ray energy greater than 6–8 keV) and around the critical angle α_c, resulting in a lengthy footprint. As a result, for $\alpha_i > \alpha_c$, the beam penetrates the film and the diffused signals are scattered from a rather big volume of samples on scales relevant to common photovoltaic systems. As a result, GIXS can obtain high statistical information of the structures buried underneath to the real-space information collected by scanning electron microscopy on tiny areas of the sample surface [7, 8].

The in-plane exit angle α_f and out-of-plane angle ψ are used to describe scattered waves with momentum $\overrightarrow{k_f}$ (in regard to the scattering plane). The scattering vector is

$$\overrightarrow{q} = \overrightarrow{k_f} - \overrightarrow{k_i} = \begin{pmatrix} \cos\alpha_f \cos\psi - \cos\alpha_i \\ \cos\alpha_f \sin\psi \\ \sin\alpha_i + \sin\alpha_f \end{pmatrix} \tag{2.1}$$

GIXS, in general, provides solid statistics across a large sample volume while being non-destructive. Different length scales can be examined depending on the sample–detector distance (SDD): Crystallographic information (particularly regarding crystal orientation) with GIWAXS, (mesoscale) domains and their organisation with GISAXS. When paired with high-brilliance synchrotron (or high-flux neutron) sources, the counting time is reduced to milliseconds (minutes), and GIXS may be used to study chemical and physical processes in-situ or operando. GIWAXS is also supplementary to (specular) X-ray diffraction (XRD), which explores a tiny portion of reciprocal space along the surface normal (q_z direction) [7, 8].

2.1.2 X-ray Diffraction

A typical method for investigating crystalline materials is X-ray diffraction (XRD). According to Bragg's law, a parallel monochromatic X-ray beam with wavelength λ hits crystal surfaces at a distance d_{hkl} and produces intensity through constructive interference:

$$n\lambda = 2d_{hkl}\sin\theta \tag{2.2}$$

In a Bragg–Brentano measurement setup, the source and (point) detector are varied while maintaining an angle of 2θ with each other, and the diffraction vector $\vec{q}$ is oriented normal to the surface of the sample. The intensity of a diffraction peak is determined by the arrangement of N_j atoms throughout the crystal (specifically, the electron density ρ_e at position $\vec{r} = (x_j + y_j + z_j)$ and is thus highly dependant on the atomic structure factor F_{hkl} and, in turn, the atomic form factor f_j, which measures the effectiveness of the electron group in each atom's ability to scatter X-rays at any angle.

$$I_{hkl} \propto |F_{hkl}|^2 \tag{2.3}$$

$$F_{hkl}(\vec{q}) = \sum_{j=1}^{m} N_j f_j exp[2\pi i(hx_j + ky_j + lz_j)] \tag{2.4}$$

$$f_j(\vec{q}) = \int_V \rho_e(\vec{r}) exp[2\pi i(\vec{q} \cdot \vec{r})]dV \tag{2.5}$$

Thus, $F_{hkl}(\vec{q}) = 0$ unless the Laue condition for reciprocal lattice a^*, b^*, and c^* vectors is satisfied.

$$\vec{G} = ha^* + kb^* + lc^* \equiv \vec{q} \tag{2.6}$$

The crystal phase of the probed material can be determined by considering the relative location of the generated reflexes (often depicted in dependency of the Bragg angle 2θ). The peak shape conceals further information about the structure: Apart from instrumental effects, peak broadening is related to crystal size D and micro-strain, as discovered by Stokes and Wilson in 1944 [9]:

$$\Delta \cos\theta = \frac{k\lambda}{D} + 4\epsilon \sin\theta \Longrightarrow \tag{2.7}$$

$$D = \frac{k\lambda}{\triangle \cos\theta - \epsilon 4 \sin\theta} = \frac{k\lambda}{y - \epsilon x} \tag{2.8}$$

$$\epsilon = \frac{\Delta \cos\theta}{4 sin\theta} = \frac{y}{x} \tag{2.9}$$

The first half of this equation is the well-known Scherrer equation, which was developed in 1918 and connects crystal size D to peak full-width-half-maximum (FWHM) Δ [10]. The crystallite form factor K is frequently estimated as K = 0.9, implying a spherical (or random) crystal shape; a cuboid crystal shape, as predicted for hybrid perovskites, is better described by K = 1 [11]. If micro-strain is taken into account, graphing $\delta\cos\theta$ versus 4 $\sin\theta$ in a Williamson–Hall plot yields D from the intersection of a linear fit with the vertical axis, which is obtained from the slope $\frac{y}{x}$. This analysis is solely limited to isotropic crystal orientations (i.e. powder diffraction).

In the laboratory, X-rays are frequently created by the emission of a Cu anode, which has a particular spectrum with high intensities for the Kα_1 (transition from L3 to K, 1.5406 Å) and Kα_2 (transition from L2 to K, 1.5444 Å) doublets [12]. If no costly filtering lenses are utilised, they generally overlap, widening the peak even further.

The peak shape is critical for correcting additional instrumental broadening effects caused by beam size and divergence. The adjustment is quadratic if the data is fitted with a Gaussian peak shape:

$$\beta_{obs}^2 = \beta_{size}^2 + \beta_{strain}^2 + \beta_{instr}^2 \tag{2.10}$$

With a Lorentzian peak shape, the correction is linear:

$$\beta_{obs} = \beta_{size} + \beta_{strain} + \beta_{instr} \tag{2.11}$$

Thus, the corrected FWHM is in the Gaussian case:

$$\Delta = \sqrt{\beta_{obs}^2 + \beta_{instr}^2} \tag{2.12}$$

$$\tag{2.13}$$

and in the Lorentz case:

$$\Delta = \sqrt{\beta_{obs} + \beta_{instr}} \tag{2.14}$$

$$\tag{2.15}$$

2.1.3 Grazing-Incidence Wide-Angle X-ray Scattering

The 2D detector in grazing-incidence wide-angle X-ray scattering (GIWAXS) is located near the sample, allowing for large diffraction angles equivalent to XRD. As a result, the physics of this measuring approach are identical, and equations 2.2 and 2.3 also apply. In contrast to XRD, the incidence angle α_i in GIWAXS is fixed. The scattering signal is made up of each Bragg angle 2θ, and it is typically collected by an area detector, containing information on crystal phase and orientation along the substrate surface normal. Thus, crystal orientation is defined by the azimuthal angle χ to the normal component q_z of the scattering vector, whereas random orientation results in the creation of Debye–Scherrer rings with a homogeneous distribution of intensity. Since GIWAXS investigates scattering signals produced by a set incident beam $\vec{k_i}$, the scattered wave-vector $\vec{k_f}$ represents a sphere geometry in reciprocal space (Ewald sphere), and the reciprocal lattice points corresponding with its surface satisfy the Laue condition. With using 2D detectors, the detector image must be adjusted as a result, which causes a missing-wedge area in the reshaped GIWAXS images [8].

Measurement Principle

An incident X-ray beam with a fixed incidence angle hits a scattering center (lattice point) in a crystal resting on a substrate. Its coordinate system in real space is supplied by x, y, and z. The reciprocal lattice vectors $a^*, b^*, and\ c^*$ (drawn in two dimensions for simplicity as shown in 2.2) span the lattice in reciprocal space. The origin of reciprocal space O is built at twice the wavevector $\vec{k_i}$, which is also the radius of the (3-dimensional) Ewald sphere. The surface of the Ewald sphere crosses specific lattice points (blue), which satisfy the Laue condition $\vec{G} \equiv \vec{q}$, implying that momentum is transferred to the final wavevector $\vec{k_f}$, and the momentum transfer is defined by $\vec{q}$.

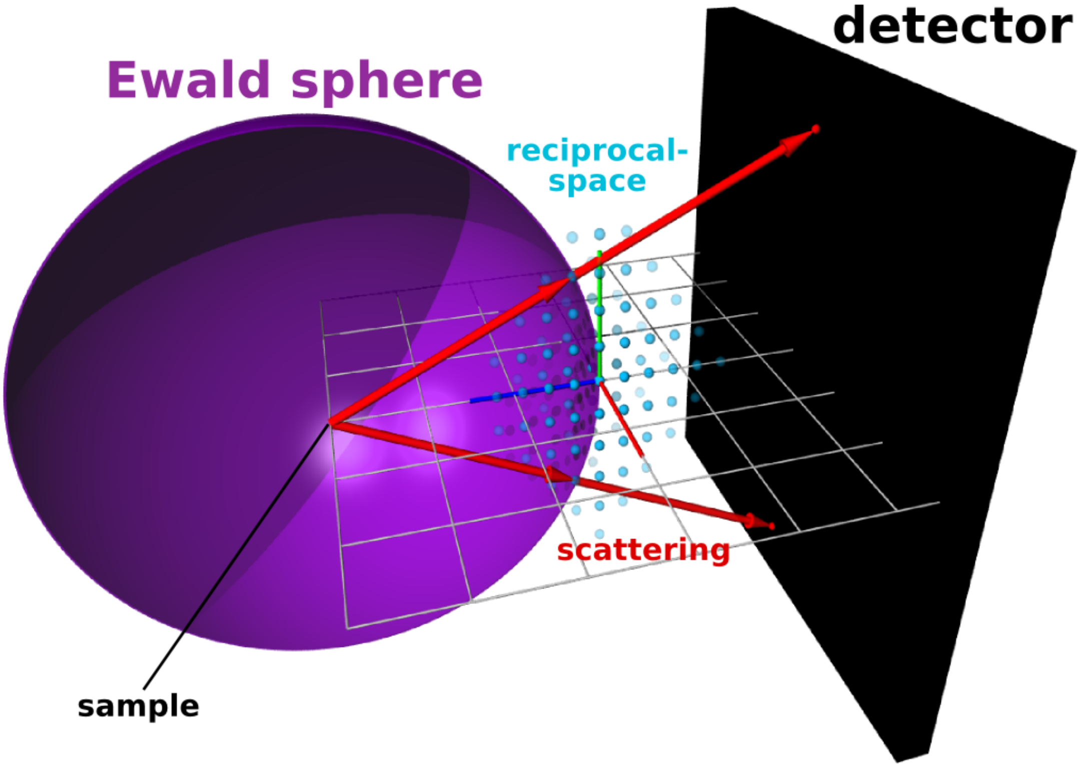

Figure 2.2: In an x-ray scattering experiment, a reciprocal-lattice (blue dots) is examined. The signal on the detector is caused by the junction of the Ewald sphere and the reciprocal-space peaks. It is worth noting that the experiment does not investigate the 'true' q_z axis (green). Reprinted with permission from [13]. Copyright 2022 MediaWiki.

The angle formed by these two wavevectors (in real and reciprocal space) is equal to two. Because this circumstance is valid for all lattice points, parallel (dashed black) lines may be constructed by connecting the scattering centre and the other lattice point. As a result, the wavevector transfer contributes in the q_x direction. The scattering angle 2θ may be characterised in real space by an azimuthal contribution (in the sample reference frame) and an out-of-plane contribution α_f. The momentum transfer $\vec{q}$ is projected in two dimensions onto a (flat) detector, and so contributes significantly to q_x in both directions (hence the coordinate system q_{xy} and q_{xz} in Figure 2.1). By employing Equation 2.1, the momentum transfer may be transferred from the reciprocal space coordinate system to the real-space coordinate system. As a result, there are three possible methods to show GIWAXS data without sacrificing information (see Figure 2.3):

(1) converting detector pixels to the in-plane ψ and out-of-plane angles α_f (only minor deviations are visible at high angles);
(2) depicting q_z versus $q_r = \sqrt{q_x^2 + q_y^2}$, which requires a transformation that results in a

distorted detector image and a missing wedge around $q_r = 0$ or $\chi = 0$;
(3) plotting total q = $|\vec{q}|$ versus azimuthal angle (on the detector plane).

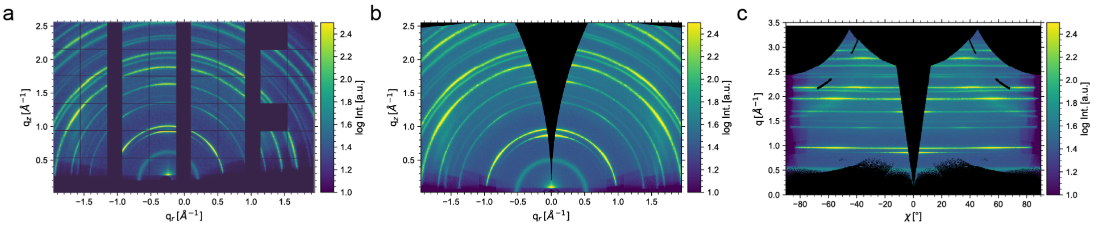

Figure 2.3: Possible representations of 2D GIWAXS data include the following: (a) detector images collected from a Lambda 4.5M detector, (b) q transformation resulting in a missing wedge due to the inaccessibility of lattice sites with $q_r = 0$, and (c) complete q vs. χ representation.

Date Treatment

Because of the measurement geometry used in GIWAXS, the detector picture is only a distorted representation of the reciprocal crystal lattice, and so specific corrections must be added to allow for its entire reconstruction. These adjustments are mostly due to the large scattering angles 2θ and, therefore, have only a minor influence in GISAXS.

For the data analysis described in this thesis, the term ”pseudo-XRD” refers to an integration over all angles that theoretically results in a scattering pattern similar to powder XRD (after applying the corrections discussed below); A ”cake cut” is a slice over a narrower angular range. Azimuthal (”tube”) cuts are made along the q location of the (hkl) reflex (Debye–Scherrer ring) of interest to analyse crystal orientations.

Averaging across a wide sample area (as in grazing-incidence geometry) implies averaging over a large number of crystal orientations. As a result, a reciprocal lattice vector with random orientations defines a so-called orientation sphere around the origin of reciprocal space, a Debye–Scherrer ring seen on the detector is the (circular) intersection of the orientation sphere and the Ewald sphere [14]. A polar angle in the crystal orientation sphere denotes the orientation with respect to the substrate normal; an azimuthal (equatorial) angle denotes the in-plane orientation distribution, which is not available using GIWAXS. By contrast, the ”azimuthal” angle χ of the Debye–Scherrer ring engraved on the area detector corresponds to the orientation sphere’s polar angle. For the sake of clarity, the term azimuthal angle χ refers to throughout this work. The FWHM from peaks in the cake-cut is massively broadened in GIWAXS due to the convolution of the scattering signal with the beam shape from the large footprint.

The **flat field correction**and the **dark field correction** account for the different sensitivities of individual pixels on the area detector; while the first is performed directly on the detector server using manufacturer-supplied calibration files, the second can be omitted by masking individual ”dead” or ”hot” pixels.

The **solid angle correction** takes the measurement geometry into account since the nominal pixel area $A_0 = L_x L_y$ encompasses a range of solid angles relative to the scattering centre. The adjustment is as follows:

$$C_\Omega = \frac{\Delta\Omega_0}{\Delta\Omega_{2\theta}} \tag{2.16}$$

$$\Delta\Omega_0 = \frac{A_0}{r_0^2} \tag{2.17}$$

$$\Delta\Omega_{2\theta} = \frac{A_{2\theta}}{r_{2\theta}^2} \tag{2.18}$$

Where $\Delta\Omega_0$ and r_0= SDD denote the solid angle and distance of the scattering centre to the pixel at the direct beam position on the detector (x_0, y_0), respectively, and $A_{2\theta} = A_0 \cos 2\theta$, and $r_{2\theta} = \mathrm{SDD}/cos2\theta$ denote the effective pixel area, solid angle, and distance of a pixel (x_j, y_j) at the oblique scattering angle which is shown in below equation, respectively.

$$2\Theta = \arctan \frac{\sqrt{L_x^2(x_j - x_0)^2 + L_y^2(x_j - x_0)^2}}{SDD} \tag{2.19}$$

As a result, the intensity of the scattering is normalised to the intensity at the direct beam point.

Due to the very short SDD and broad scattering angles, various factors must be considered when calculating the chance of a scattered photon being detected by a pixel (**efficiency corrections**). Photons dispersed at various oblique scattering angles 2θ travel varying lengths through a material with a linear mass attenuation coefficient m, and hence the attenuation is varied according to the below equation:

$$C_M = (exp[-\mu_m r_{2\theta}])^{-1} \tag{2.20}$$

No attenuation is required for measurements made in vacuum, and $\mu_m = 0$. Additionally, a photon striking a detector pixel at a large oblique angle 2θ has a larger likelihood of absorption than a photon striking at a lower angle, since its journey:

$$d_2 = \frac{d_0}{\cos 2\theta} \tag{2.21}$$

through the single photon counter with thickness d_0 is longer. Thus, the linear mass attenuation coefficient d of the sensor material (usually silicon) results in the absorption variation correction as follows:

$$C_D = ([1 - exp(-\mu_d d_{2\theta}])^{-1} \tag{2.22}$$

As a result, absorption of X-rays by the sample may be ignored, and so no absorption correction is required.

Polarization correction is needed because Synchrotron sources generate X-rays with a large proportion of horizontal (linear) polarisation (usually about 98 %), which generates a dipole oscillation of the electrons in the investigated material in the polarisation direction. As a result of this energy loss, a portion of the photons' energy is lost to electron excitation a reducing the scattering intensity in this direction. However, even when beams are not polarised, the dipole emission profile has a small effect on the scattering intensity. To compensate for this impact, one should connect the angle ξ between the polarisation direction and the exit wavevector k_f through:

$$C_p = \zeta_h \left|\sin\xi\right|^2 + (1-\zeta_h)\cos^2\alpha_f = \zeta_h(1-\cos^2\alpha_f \sin^2\psi) + (1-\zeta_h)\cos^2\alpha_f) \tag{2.23}$$

where the horizontal polarization fraction of the beam locates between 0 and 1.

In summary, the corrected intensity of each pixel I_{corr} is corrected by:

$$I_{corr} = I_{raw} C_{FF} C_{\Omega} \frac{C_M C_D}{max(C_M C_D)} \frac{1}{C_P} \tag{2.24}$$

There is some controversy in the literature about whether the intensities of azimuthal GIWAXS cuts should be amplified by a factor $\sin\chi$ [14–16]. This follows from the preceding illustration of the orientation sphere: With an isotropic crystal orientation in the sample plane but a limited film thickness, the sample resembles a ”2D powder,” in contrast to a true ”3D powder” sample generally measured in transmission geometry. The primary rationale for the adjustment is that crystals with an in-plane orientation spread their scattering intensity evenly over the equator of the orientation sphere, while crystals with an out-of-plane orientation concentrate their intensity towards the poles. Thus, if the orientation sphere is intersected with the Ewald sphere, the resultant ring on the detector will have a higher intensity for out-of-plane orientation even though the crystal orientation is isotropic. Corrections for two-dimensional and three-dimensional powder are implemented in GIXSGUI as distinct Lorentz corrections and evaluated [17]. It should conclude that since the modifications distort the results, they should not be used on highly crystalline hybrid perovskite thin films. A probable reason is that, in contrast to less organised semi-crystalline polymer films, perovskite crystals as high crystalline materials do not qualify as a 2D powder.

Drawbacks

While GIWAXS is capable of presenting powerful crystallographic information on thin films, it has a number of limitations that should be addressed during data processing.

The most significant is the inaccessible wedge-shaped area around $q_r \approx 0$, which can be retrieved only partially by repeated observations at higher α_i. If a fit is employed to estimate the peak intensity concealed in this region, it should be compared to other reflexes that do not fall inside the missing wedge.

The SDD is a source of uncertainty since it is on par with the normal sample size and the dimensions of the beam’s imprint on the sample: This results in a significant widening of the Debye–Scherrer rings on the detector, which becomes more pronounced with increasing scattering angles. This is because the scattering centres are distributed across the footprint, resulting in a wide range of detector distances and not a single SDD. Thus, crystal sizes may be extracted using the Scherrer equation only when the instrumental broadening at the specified measurement conditions is minimal in comparison to the size widening, which limits it to semi-crystalline polymers studied with a highly focused X-ray beam. Incorrect sample height modification further alters the SDD substantially.

2.1.4 Grazing-Incidence Small-Angle X-Ray Scattering

The sample-to-detector distance is set far from the sample in grazing-incidence small-angle X-ray scattering (GISAXS), with typical sample–detector distances exceeding 1 m. The accessible length scales ranging from nanometers to micrometres, making them useful for exploring crystal shapes and relative size distributions. The refractive index of X-rays (and neutrons) is near unity and is:

$$n = 1 - \delta + i\beta \tag{2.25}$$

For "hard" X-rays (> 8 keV), the scattering event is elastic.

$$\left|\vec{k_i}\right|^2 = \left|\vec{k_f}\right|^2 = k \tag{2.26}$$

GISAXS is mostly determined by the dispersion, which is determined by the scattering length density (SLD). Thus, GISAXS is very sensitive to materials; when the film scatters X-rays, the signals are scattered from the film surface at the critical angle α_c, leading to an enhanced intensity for $\alpha_f = \alpha_c$ at the Yoneda peak [18]. Thus, the GISAXS signal is evaluated by executing the Yoneda peak of materials by horizontal line cuts, and the decline of intensity provides information about the inner morphology of film in comparison to its surrounds. However, converting reciprocal-space data to real-space structures requires sophisticated modelling that accounts for scattering and reflection between scattering objects and the substrates. Additionally, the form of the scattered items must be taken into account. The **distorted wave Born approximation (DWBA)** is a widely used method for data modelling. It differentiates between four different scattering events and defines the superposition of scattered intensity. The interactions between X-rays and scattering objectives inside the film are modelled by using form and structure factors that correspond to the shapes and distances of the domains in real space [7, 8, 19–22].

Diffuse X-Ray Scattering

Levine et al. produced the first GISAXS observations in 1989, however Y. Yoneda is credited with finding the "anomalous surface reflection of X-rays" [18, 23]. At modest scattering angles, the probed region of the Ewald sphere may be regarded as sufficiently flat, and hence the detector picture immediately translates to q_y and q_z as shown in Figure 2.1, without the need for further corrections as in GIWAXS. The critical angle may be estimated using Snell's equation for shallow angles.

$$n = \sin\left[90^\circ - \alpha_c\right] = \cos\alpha_c \approx 1 - \frac{\alpha_c^2}{2} \tag{2.27}$$

as

$$\alpha_c(\lambda) \approx \sqrt{2\delta(\lambda)} \tag{2.28}$$

As previously stated, small incidence angles cause anomalous scattering from "rough surfaces," i.e. photon out-coupling below the sample's critical angle α_c, which results in the Yoneda peak. For multi-component systems, understanding the substance of interest is critical. Henke et al. (http://henke.lbl.gov) provide the atomic form factors f_j for each element at various X-ray energies by:

$$f_j = f_j^0 + f_j'(\lambda) + f_j''(\lambda) \tag{2.29}$$

where f_0 may be approximated by the number of electrons Z_j of an element j (for X-rays) with the dispersion correction $f_j'(\lambda)$ and $f_j''(\lambda)$. The scattering length at point $\vec{r}$ is:

$$\rho(\vec{r}) = r_e \rho_e(\vec{r}) \tag{2.30}$$

where r_e is the material's particular electron density and $\vec{r}$ is the classical electron radius (Thomson scattering length).

$$r_e = \frac{1}{4\pi\epsilon_0}\frac{e^2}{m_e c^2} \approx 2.818 \times 10^{-15} \text{ m} \tag{2.31}$$

with the speed of light c , the elementary charge e , the electron rest mass m_e, and the permittivity constant ϵ_0. Thus, the scattering length density (SLD) of a material is calculated by adding the contributions of each element and weighting them by the stoichiometric proportion c_j.

$$SLD(\vec{r}) = \rho(\vec{r}) \frac{\sum_j c_j \left(f_j^0 + f_j'(\lambda) + f_j''(\lambda)\right)}{\sum_j Z_j} \tag{2.32}$$

Alternatively, by inserting $Z_j N_A = M_j$, the particular molar mass M_j may be used. Thus, the dispersion and absorption coefficients are location and wavelength dependent:

$$\delta(\vec{r},\lambda) = \frac{\lambda^2}{2\pi}\Re(SLD) = \frac{\lambda^2}{2\pi}\rho(\vec{r})\frac{\sum_j c_j \left(f_j^0 + f_j'(\lambda)\right)}{\sum_j Z_j} \tag{2.33}$$

$$\beta(\vec{r},\lambda) = \frac{\lambda^2}{2\pi}\Im(SLD) = \frac{\lambda^2}{2\pi}\rho(\vec{r})\frac{\sum_j c_j f_j''(\lambda)}{\sum_j Z_j}. \tag{2.34}$$

With the approximations $f_j^0 \approx Z_j$ and $f_j' \ll f_j^0$ and for constant λ this becomes:

$$c\delta(\vec{r}) = \frac{\lambda^2}{2\pi}\rho(\vec{r}) \tag{2.35}$$

$$\beta(\vec{r}) = \frac{\lambda}{4\pi}\mu(\vec{r}) \tag{2.36}$$

with μ being the X-rays' linear mass attenuation coefficient. For hard X-rays, the orders of magnitude are:

$$c\delta = \mathcal{O}\left(10^{-6}\right) \tag{2.37}$$

$$\beta = \mathcal{O}\left(10^{-7}\right) \tag{2.38}$$

The scattering arises from an interface between two domains j and j_0 with differing refractive indices, and the scattering contrast Δ is given by the differences in δ and β:

$$|\Delta|^2 = \Delta\delta^2 + \Delta\beta^2 \tag{2.39}$$

The typical absorption length $1/\mu$ establishes a limit on the depth inside a film to which a scattered photon may re-enter, and the so-called scattering depth Λ can be determined using the incoming l_i and outgoing X-ray paths l_f:

$$\Lambda = \frac{\lambda}{\sqrt{2}\pi\left(l_i + l_f\right)} \tag{2.40}$$

$$l_{i,f} = \left(\sin^2\alpha_c - \sin^2\alpha_{i,f} + \sqrt{\left(\sin^2\alpha_{i,f} - \sin^2\alpha_c\right)^2 + \left(\frac{\mu\lambda}{2\pi}\right)^2}\right)^2 \tag{2.41}$$

The total differential scattering cross section is used to calculate the probability of a scattering event:

$$\frac{d\sigma}{d\Omega}(\vec{q}) = \frac{1}{V}\left\langle \sum_j \sum_{j'} F_{j'}^*(\vec{q})F_j(\vec{q}) \exp\left[i\vec{q}\cdot\left(\overrightarrow{r_j} - \overrightarrow{r_j'}\right)\right]\right\rangle \tag{2.42}$$

where V is the scattering volume, $r_{j,j'}$ the center positions of two scattering domains j and j' , and $F_j(\vec{q})$ and $F_{j'}(\vec{q})$ are the domains' form factors (analogous to the atomic form factors).

$$F_j(\vec{q}) = \int_j \left(\rho\left(\overrightarrow{r_j}\right) - \rho\left(\overrightarrow{r_{j'}}\right)\right) \exp\left[i\vec{q} \cdot \overrightarrow{r_j}\right] d \tag{2.43}$$

with the term $\left(\rho\left(\overrightarrow{r_j}\right) - \rho\left(\overrightarrow{r_{j'}}\right)\right)$ relating to the scattering contrast in Equation 2.37. The notation $\langle\rangle$ signifies the averaging over all possible rotations. Writing $F^*_{j'}(\vec{q})F_j(\vec{q}) = F^2(\vec{q})$ and adding an interference function called structure factor $S(\vec{q})$ that is related to the interparticle arrangement, this can be reduced to:

$$\frac{d\sigma}{d\Omega}(\vec{q}) = \frac{N_j}{V} F^2(\vec{q}) S(\vec{q}) \tag{2.44}$$

with

$$S(\vec{q}) = \frac{1}{N_j} \left\langle \sum_j \sum_{j'} \exp\left[i\vec{q} \cdot \left(\overrightarrow{r_j} - \overrightarrow{j'}\right)\right] \right\rangle. \tag{2.45}$$

The expression introduces extra interaction terms for disordered systems, i.e. those with uneven domain sizes or distributions:

$$\left\langle F^*_{j'}(\vec{q})F_j(\vec{q}) \right\rangle = |\langle F(\vec{q})\rangle|^2 + \delta_{j,j'} \left(\left\langle \left|F^2(\vec{q})\right|^2 \right\rangle - \left|\left\langle F^2(\vec{q}) \right\rangle\right|^2 \right) \tag{2.46}$$

with the Kronecker delta $\delta_{j,j'}$,which are removed due to the **decoupling approximation** (DA)'s disregard for correlations between the distributed type and their relative arrangement [24].

$$\frac{d\sigma}{d\Omega}(\vec{q}) \propto N |\langle F(\vec{q})\rangle|^2 S(\vec{q}). \tag{2.47}$$

This implies $\left(\left\langle |F^2(\vec{q})|^2 \right\rangle = |\langle F^2(\vec{q})\rangle|^2\right)$ and , the interference function is equal to the structure factor $S(\vec{q})$ of a suitable mono-disperse system without any extra terms. Poly-disperse systems with domains greater than the beam's coherence length may be considered as locally mono-disperse using the **local mono-disperse approximation** (LMA), which results in the incoherent cross-section for a particular kind of scatter [25].

$$\frac{d\sigma}{d\Omega}(\vec{q}) \propto N \left\langle |F(\vec{q})|^2 S'(\vec{q}) \right\rangle \tag{2.48}$$

$S'(\vec{q})$ is a local interference function that includes incoherent components. As a result, unlike the **DA**, a strong correlation between the sizes of surrounding domains is predicted.

Accounting for Reflection Geometry

Multiple scattering effects are induced due to the existence of a reflecting contact (the substrate). In terms of the small scattering angle, the diffuse scattering from a ”rough surface” reads:

$$\frac{d\sigma}{d\Omega}(\vec{q}) = \frac{A\pi^2}{\lambda^4}|\Delta|^2\,|T_i|^2\,|T_f|^2\,P(\vec{q}) \tag{2.49}$$

where A is the sample area which is exposed, $|T_{i,f}|$ refers to the Fresnel transmission coefficients for the incoming and outgoing beam, which both have a maximum at α_c leading to the enhanced intensity of the Yoneda peak. This is why horizontal cuts are often made at this spot. The diffuse scattering factor is denoted by P($\vec{q}$). In the so-called **distorted-wave Born approximation** (DWBA), several scattering events are examined [22]:

$$P(\vec{q}) \propto NS'(\vec{q})F^2_{DWBA}(\vec{q}) \tag{2.50}$$

by three extra terms of the type $F_{DWBA}(\vec{q})$ about reflection occurring before to and/or after diffraction at an object. The importance of these contributions is significantly dependent on the refractive index of the substrate and decreases as the exit angles α_f increase.

Data Modelling

To convert the information contained in the GISAXS experiments' reciprocal-space data to actual space, I assume a model of abstract geometric forms as scattering objects spread over a reflecting surface. The program used to generate out-of-plane scattering curves is based on a deduction by David Magerl, which was developed for Python 2.7 by Christoph J. Schaffer and fine-tuned by D. Magerl and L. Bieβmann, and was further upgraded by Lennart K. Reb, Manuel A. Reus.

To use the **LMA** for simplicity; contributions from various kinds of scattering events are therefore considered individually, and hence easily summarised:

$$P(\vec{q}) \propto \sum_j N_j S'_j(\vec{q}) F_j(\vec{q}) \tag{2.51}$$

If one modifies the equations published by R. Lazzari in the compendium for the program IsGISAXS using the approximations indicated above [24]. After Hosemann et al., the mean inter-domain distance D_c of a perturbed system reads:

$$S'(\vec{q}) = -\frac{1-\phi^2(\vec{q})}{1+\phi^2(\vec{q})-2\phi(\vec{q})\cos\left[|\vec{q}|D_c\right]} \tag{2.52}$$

with

$$\phi(\vec{q}) = \exp\left[\pi\omega_D^2 D_c^2 |\vec{q}|^2\right] \tag{2.53}$$

where ω_D is the breadth (standard deviation) of a Gaussian (normal) distribution centred on D_c [25].

When a cut at constant q_z is considered (which is approximated as $q_z \approx 0$), Equation 2.50 simplifies, and the distance between two scattering centres D_c is given by:

$$S'\left(q_y\right)\big|_{q_z\approx 0} = -\frac{1-\exp\left[\pi\omega^2 D_c^2 q_y^2\right]^2}{1+\exp\left[\pi\omega^2 D_c^2 q_y^2\right]^2 - 2\exp\left[\pi\omega^2 D_c^2 q_y^2\right]\cos\left[q_y D_c\right]} \tag{2.54}$$

This is the interference function of a **one-dimensional paracrystal**, and so implicitly adopts the **effective interface approximation (EIA)**, which ignores vertical correlations of the scattering intensity [20, 24].

If one considers basic rotationally averaged geometrical forms as scattering objects, specifically spheres (for full isotropy) and cylinders (accounting for the vertical constraint by the substrate and film surface). The various form factors are as follows:

$$F_{sph}(\vec{q}) = 4\pi R^3 \frac{\sin[qR] - qR\cos[\vec{q}\cdot\vec{r}]}{(qR)^3} \exp\left[iq_z R\right] \tag{2.55}$$

for spheres with radius R , and

$$F_{cyl}(\vec{q}) = 2\pi R^2 H \frac{J_1\left(q_r R\right)}{q_r R} \sin\left[q_z \frac{H}{2}\right] \exp\left[iq_z \frac{H}{2}\right] \tag{2.56}$$

for cylinders with radius R and height H , with $J_1\left(q_r R\right)$ being the first-kind Bessel function of first order. Again applying the **EIA**, the expressions simplify:

$$l \left|F_{cyl}\left(q_y\right)\right|^2\Big|_{q_z\approx 0} \approx \left(R\frac{J_1\left(q_y, R\right)}{q_y}\right)^2 \tag{2.57}$$

$$\left|F_{sphi}\left(q_y\right)\right|^2\Big|_{q_z\approx 0} \approx \left(\frac{\sin\left[q_y R\right] - q_y R\cos\left[q_y R\right]}{q_y^3}\right)^2 \tag{2.58}$$

In order to introduce poly-dispersity into the system, the domains are represented using a discrete Gaussian distribution with 1000 points.

$$\mathcal{G}(R) = \frac{1}{\omega_R\sqrt{2\pi}} \exp\left[-\frac{(R-\langle R\rangle)^2}{2\omega_R^2}\right] \tag{2.59}$$

with the average domain radius $\langle R\rangle$.

$S(\vec{q}) = 1$ in the so-called **Guinier limit** for a low scattered concentration, which in the case of a (more or less) dense hybrid perovskite film might indicate that the micrometer-sized domains (crystals) are larger than the resolution limit and the resolved structures are sparse.

The generated model curves reflect the diffuse scattering factor $P(\vec{q}) = 1$, which is proportional to the number of scatters N_J and consequently to the domain size. This relationship is eliminated by normalising the form factors during the first fitting rounds (which obliterates the significance of the intensity value); for relative comparisons of scattering intensities, the data is fitted without normalisation. The set of fitting parameters, namely $\langle R\rangle, \omega_R, D_c, \omega_D$, may then be modified separately to overlap the data. A three-parameter Lorentzian function is used to approximate the instrumental resolution around $q_y = 0$.

$$\mathcal{L}_{\text{res}}\left(q_y, \omega_{\text{res}}, I_{\text{res}}\right) = I_{\text{res}}\left(1 + \left(\frac{q_y}{\omega_{\text{res}}}\right)^2\right)^{-1} \tag{2.60}$$

Using a width ω_{res} that is tuned to replicate the centre scattering rod, i.e. the first 2-3 data points. To account for extra factors, such as surface roughness, a linear backdrop is utilised.

2.2 Perovskite Solar Cells

Hybrid perovskites have the formula ABX_3 (where A is MA^+, FA^+, Cs^+, B is Pb^+, and Sn^+, and X is a halide ion such as I^-, Br^-, or Cl^- [26]. Their extraordinary tunable optoelectronic characteristics, along with their high crystallinity, particularly for solution-processed materials, have sustained attention throughout the years [8, 27–30]. However, until 2009, hybrid perovskites were viewed as a viable alternative to the notoriously unstable dyes used in dye-sensitized solar cells (DSSCs) [31]. Although the first power conversion efficiency (PCE) was very low and the device declined within seconds, further research improved the device's stability, resulting in PCE reaching 10% in late 2012 [32]. Strong competition between research groups, most notably those led by Henry Snaith (University of Oxford) [33], Michael Grätzel (École Polytechnique Fédérale de Lausanne, EPFL) [34], and Sang II Seok (Korea Research Institute of Chemical Technology, KRICT) [35], resulted in unprecedented rapid progress, ultimately resulting in PCE values well above 25% and good stability in a fully printable architecture [36].

2.2.1 Working Principle for Solar Cells

When a photon with higher energy than the bandgap energy E_g of a semiconductor is absorbed, the bound photo-excited species ("exciton") are in thermal equilibrium with the Sun. They soon thermalize to the band boundaries, though, and the extra energy is dissipated. Depending on the material's dielectric constant, ϵ, the exciton with binding energy E_{binding} is dissociated into two free charge carriers, an electron and a hole with decreased effective masses m_e^* and m_h^*:

$$E_{binding} = -\frac{m_{e,h}^* e^4}{8\epsilon\epsilon_0 h^2} \tag{2.61}$$

The electron-hole pair is now thermally matched to the lattice, its distributions are characterised by a Fermi-Dirac distribution function:

$$n_{e,h} = N_{CB,VB} \exp\left[-\frac{\left|E^{CB,VB} - E_F^{CB,VB}\right|}{k_B T}\right] \tag{2.62}$$

where $N_{CB,VB}$ are the effective densities of states, $E^{CB,VB}$ are the energy levels, and $E_F^{CB,VB}$ are the respective quasi-Fermi levels of the conduction band (CB) and the valence band (VB), the latter being the electrochemical potential of either species. The split of the Fermi level E_F is divided owing to the presence of extra charge carriers in either energy band. The maximum energy of solar cells is governed by the potential difference $E_F^{CB} - E_F^{VB}$, the free energy per electron-hole pair. According to Fick's law, a chemical potential gradient $\nabla\mu$ over the device causes a diffusion current density J_{diff}:

$$J_{diff} = -D\frac{en_{e,h}}{k_B T}\nabla\mu \tag{2.63}$$

where D is the diffusion coefficient.

An extra electrical potential gradient $\nabla\phi$ (due to an external field, for example) results in a drift current density J_{drift}.

$$J_{drift} = -\sigma\nabla\phi \tag{2.64}$$

with σ representing conductivity. Free charges (electrons and holes) are produced as a consequence of exciton dissociation due to the gradient in the combined electrochemical potential, and the net charge current density J is:

$$J = J_e + J_h = \frac{\sigma_e}{e}\nabla E_F^{CB} + \frac{\sigma_h}{e}\nabla E_F^{VB} \tag{2.65}$$

Thus, when J=0, the highest possible voltage is the open-circuit voltage:

$$eV_{OC} = E_F^{CB} - E_F^{VB} \tag{2.66}$$

When the Fermi level E_F of both electrodes is aligned, the resultant current is referred to as short-circuit current density J_{SC}. Because electrical power is zero in both circumstances, the maximum power point tracking (MPPT) involves a trade-off between free energy and the number of charge carriers.

Without illumination, the current-voltage curve of a solar cell is almost identical to that of an ideal diode.

$$I = I_0\left(\exp\left[\frac{eV}{k_B T}\right] - 1\right) \tag{2.67}$$

where I_0 is the so-called dark current, which represents the diode's leakage current and hence a measure of device recombination. The J-V curve changes with illumination as a result of the increased current produced by extracted photo-generated charge carriers, the photo-current I_{ph}. This is given by the Shockley equation in an ideal solar cell:

$$I = I_0\left(\exp\left[\frac{eV}{k_B T}\right] - 1\right) - I_{ph} \tag{2.68}$$

A series resistance R_s compensates for transport losses in various solar cell layers, and a parallel shunt resistance R_p reduces photocurrent flow via the diode through alternative current pathways, and the non-ideality of the diode by the ideality factor n $\in [1, 2]$:

$$I = I_0 \left(\exp \left[\frac{e\,(V - IR_s)}{nk_B T} \right] - 1 \right) - \frac{V - IR_s}{R_p} - I_{ph}. \tag{2.69}$$

The resistances' influence on the J-V characteristic substantially affects the solar cell's extracted power, as represented by the following equations:

$$R_s = \left(\frac{dI}{dV} \right)^{-1}_{V=V_{OC}} \tag{2.70}$$

$$R_p = \left(\frac{dI}{dV} \right)^{-1}_{V=0} - R_s. \tag{2.71}$$

2.2.2 Power Conversion Efficiency of Solar Cells

In general, power conversion efficiency (PCE) of solar cells η refers to the ratio of the maximum power yielded $P_{\max}$ per cell area A under the incoming power flow E_{in}:

$$\eta = \frac{P_{\max}}{E_{in} A} = \frac{V_{MPP} I_{MPP}}{E_{in}} \tag{2.72}$$

To translate this into readily available photovoltaic characteristics, the fill factor (FF) establishes a relationship between $P_{\max}$ and the V_{OC} and I_{SC}:

$$FF = \frac{P_{\max}}{P_{\text{ideal}}} = \frac{V_{MPP} I_{MPP}}{V_{OC} I_{SC}} \tag{2.73}$$

The theoretical maximum fill factor is around 89 %; Martin A. Green discusses alternative more realistic fill factors that also allow for a decoupling of parasitic losses from R_p and R_s [26].

William Shockley and Hans Queisser were the first to determine a photovoltaic efficiency limit based only on thermodynamic considerations [37].

This so-called Shockley-Queisser limit sets the maximum PCE at 32.9 % for a homojunction solar cell with a band gap of 1.34 eV and unconcentrated sunlight with an AM1.5 spectrum and only one photogenerated exciton per photon. Their fundamental considerations are as follows:

- the likelihood of absorption (which they assume to be 1)
- losses due to entropy: dark
- body radiation caused by the temperature of the solar cell

The principle of detailed balance is considered from radiative recombination of electrons and holes, inverse absorption, and thermodynamic equilibrium as a consequence of a driving force (intrinsic carrier concentration generated thermally)

- a "matching impedance factor" (which is the FF)

The efficiency of particular energy conversion processes has expanded on these premises and expressed them according to:
- loss of spectral information: There is no absorption of photons below the bandgap's cut-off energy:

$$\eta_{abs} = -\frac{J_{SC}}{e}\frac{E_{ph}^{>E_g}}{E_{ph}} \tag{2.74}$$

- thermalization: relaxing of charge carriers inside bands to their band boundaries, bringing them into thermal equilibrium with the crystal lattice

$$\eta_{\text{thermalization}} = \frac{E_g + 3k_BT}{E_{ph}} \tag{2.75}$$

One more reduction of $\approx 3k_BT$ relates to the position of quasi-Fermi levels at the given cell temperature T:
- conversion of electron-hole pair's energy to chemical energy ($eV_{OC} < E_g$):

$$\eta_{\text{thermodynamic}} = \frac{eV_{OC}}{E_g + 3k_BT} \tag{2.76}$$

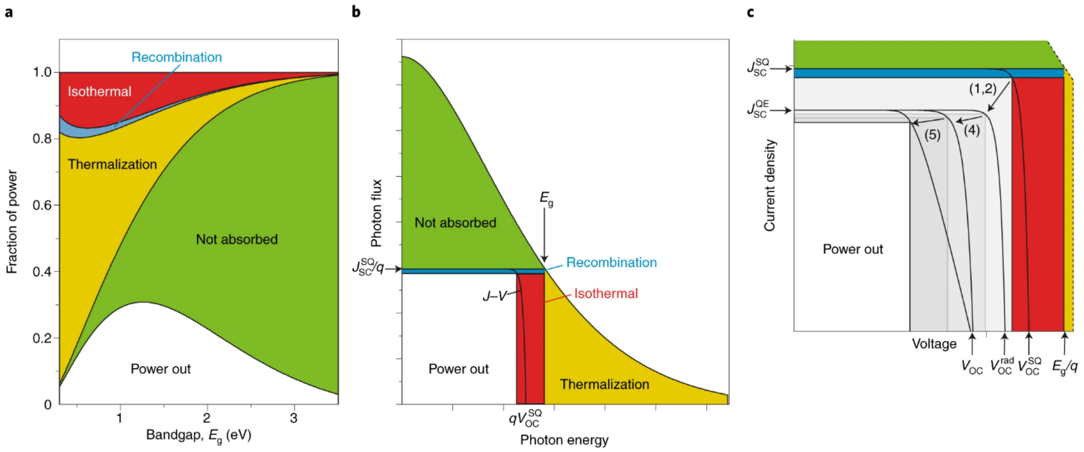

Figure 2.4: a, Illustration of losses within the SQ model as a function of the bandgap (always at maximum power point) using for the solar spectrum a 5,800 K black-body spectrum normalized to 100 mW cm^{-2}. b, Energy losses for a given bandgap energy depicted as a function of photon flux versus photon energy. By dividing the photon flux by the elementary charge q and multiplying the energy with q, the axes can also be read as current density versus voltage. The black curve denotes the current versus voltage curve, and the maximum output power is obtained for a maximum area of the white rectangle (‘Power out’), likewise a minimum area for the recombination and isothermal dissipation losses. c, Current–voltage curves of a solar cell and the power losses occurring on relaxing the SQ assumptions 1 and 2 (combined), 4 and 5. The maximum output power (illustrated by the rectangles) reduces stepwise from the SQ value P^{SQ}_{max} to the real value P^{real}_{max} . The cell temperature T_{cell} is kept at the SQ value T^{SQ}_{cell} such that assumption 3 is still valid. Violations of assumptions 1–5 are kept at a level such that the real device is still a useful solar cell. Reprinted with permission from [38]. Copyright 2019. Nature Photonics.

Thus, the total efficiency is defined as the sum of the individual contributions:

$$\eta = \eta_{\text{abs}}\ \eta_{\text{thermalization}}\eta_{\text{thermodynamic}}FF \tag{2.77}$$

Charge carrier mobility or even trapping, non-radiative recombination, and reflection of light, e.g. from the glass cover, result in other losses. The most prominent concepts to overcome the Shockley-Queisser limit are the use of concentrated sunlight, or carrier multiplication, i.e. multiple exciton generation by one photon, tandem cells or photon up/down conversion. The latter might be an intrinsic property of hybrid perovskites which possess a photon recycling mechanism [39]. According to calculations by Brendel et al., the theoretical efficiency limit for non-concentrated sunlight is around 43 %, and even 85 % if concentrator optics are used [40]. Figure 2.4a shows the famous plot of the SQ limit in black with the other contributions represented in the same color code as the equivalent in the energy flow diagram presented in Figure2.4b.

The increasing temperatures also cause a decrease in PCE and is expressed by:

$$\frac{dV_{OC}}{dT} = \frac{V_{OC} - V_{g0}}{T} - \gamma \frac{k_B}{e} \tag{2.78}$$

where $eV_{g0} = E_{g0}$ is the band gap energy extrapolated to 0 K , and $\gamma = 3$ is a characteristic material constant.

2.2.3 Architectures of Perovskite Solar cells

PSCs are made using solution-based fabrication and have the architecture as shown in figure2.5, but the most efficient PSCs mainly use expensive raw materials like gold and organic electron-blocking materials (ETMs) such as spiro-OMeTAD.

Figure 2.5: Architecture of perovskite solar cell including electrodes, electron or hole blocking layer, perovskite layer, transport conducting layer and substrate

PSCs consist of a transparent conductive oxide coated glass substrate, a hole-blocking layer, a perovskite layer, an electron-blocking layer, and a back electrode material (metal or carbon) (Figure2.5B). In mesoscopic PSCs produced as a result of DSSCs research, the perovskite absorber sensitises a mesoporous oxide layer (e.g., $meso - TiO_2$) that serves as a scaffold [41, 42].

In planar PSCs, the perovskite layer is inserted between a planar HBL, for example, compact TiO_2, SnO_2, or C_{60} and its variants and a planar EBL, for example, spiro-OMeTAD, PTAA, and PEDOT:PSS [43, 44]. Depending on the order in which the HBL and EBL are deposited, the structure may be classified as formal (conventional) or inverted [45,46]. One should note that designing and fabricating inverted devices is not a straightforward reversal of the formal device structure, and the two device architectures often need careful construction of acceptable HBLs and EBLs, particularly in light of solvent constraints. The perovskite is coated on a three-layer scaffold composed of a printing mesoporous TiO_2 layer, a ZrO_2 spacer layer, and a carbon electrode in triple mesoscopic PSCs [47,48]. Carbon electrodes are used as the metal back contacts in these devices, which do not need a hole-conducting layer.

2.2.4 Efficiency Limitation

While Figure 2.6 demonstrated the significant efficiency potential of the bare perovskite materials, the next step is to disentangle the variables restricting the FF and V_{OC} losses in the PSCs. To achieve this aim, the efficiency potential of the combination of different perovskite/transport layers by using intensity-dependent QFLS measurements once again was accessed. The J-V curve of the standard cell is shown in Figure 2.6 in comparison to the pseudo J-V curve of the intensity-dependent V_{OC}. Additionally, the picture depicts the pseudo J-V curves for the active layer and EBL junction, the optical p-i-n architecture (glass/PTAA/PFN-Br/perovskite/C_{60}), the bare film, the treated perovskite film with oxides as determined by the QFLS(I) (providing a 95 % EQE). Finally, the curve in the radiative limit (S-Q limitation) for different perovskite components. FFs and open-circuit voltages are highlighted in Figure 2.6 b, and the area around the maximum power point is zoomed in Figure 2.6 c and d to emphasise the dependent influence of the limit of efficiency processes on the V_{OC} and the FF [49].

The distinction between the J-V curve (PCE = 21.2 % with a 95 % EQE) and the pseudo J-V curve from the V_{OC} (I) measurement (pseudo PCE = 23.7 %) indicates the transport losses in PSCs (blue colour in figure 2.6 c), the pseudo J-V curve from the V_{OC} measurement is also same to the pseudo J-V curve from the p-i-n architecture (pseudo PCE = 23.5 %) obtained from the QFLS (I). This shows that non-radiative losses are minimally caused by electrodes in devices; this fact is especially significant in light of the formation of the built-in electric field in PSCs, which I shall examine in further detail below. Furthermore, the optical pseudo J-V curve of the p-i-n architecture is almost equivalent to that of the perovskite/C_{60} film (pseudo PCE = 23.5 %). This demonstrates that this interface is responsible for the majority of recombination loss in the device, which is consistent with our earlier findings [50]. The extra loss of 67 mV owing to the C_{60} interface may be determined by comparing the neat material's pseudo J-V curve (pseudo PCE = 24.8 %) to the perovskite/C_{60} film's pseudo J-V curve (purple colour in figure 2.6 c) [49].

Finally, concerning the treated perovskite film with a PCE of 27.3 %, if one speculates that trioctylphosphine oxide passives defects on the top surface only, as previously discussed, one can attribute the difference between the base and treated films to surface recombination (red colour in figure (c)) [51]. Figure 2.6 b demonstrates that the pseudo FF is approximately similar in the bare material, the perovskite/C_{60} film, and the p-i-n architecture, but rises by approximately 2 % (to 88.7 %) upon passivation, bringing the efficiency near to the radiative limit (orange colour in figure 2.6 c) for the specific band-gap. It is also worth noting that the trioctylphosphine oxide-passivated 83–17 triple cation film has a PLQY of up to 22.6 %, compared to 0.8 % for the unpassivated film. One should note that this PLQY increase is comparable to earlier findings obtained by layering trioctylphosphine oxide on top of MAPI, demonstrating that trioctylphosphine oxide passivates identical surface defects in the case of (83–17) triple cation perovskite and MAPI [52]. Additionally, this indicates that recombination in the perovskite bulk is extremely low in comparison to surface recombination. Nonetheless, one should recognise that trioctylphosphine oxide is not a successful passivation technique in full PSCs, since it may generate an insulating barrier that also inhibits the efficient extraction of majority carriers. As a result, similar passivation solutions should be sought that produce comparable luminescence yields without impairing charge transport and collecting behaviour [49].

2.2.5 Long-term Operational Stability of Perovskite Solar Cells

Their high-power harvests and low-production costs have attracted serious industry attention from established companies and have led to the founding of multiple start-up companies. However, for commercial products, long-term stability is crucial. Thus, for perovskites to succeed, an informed discussion on a detailed degradation study is required.

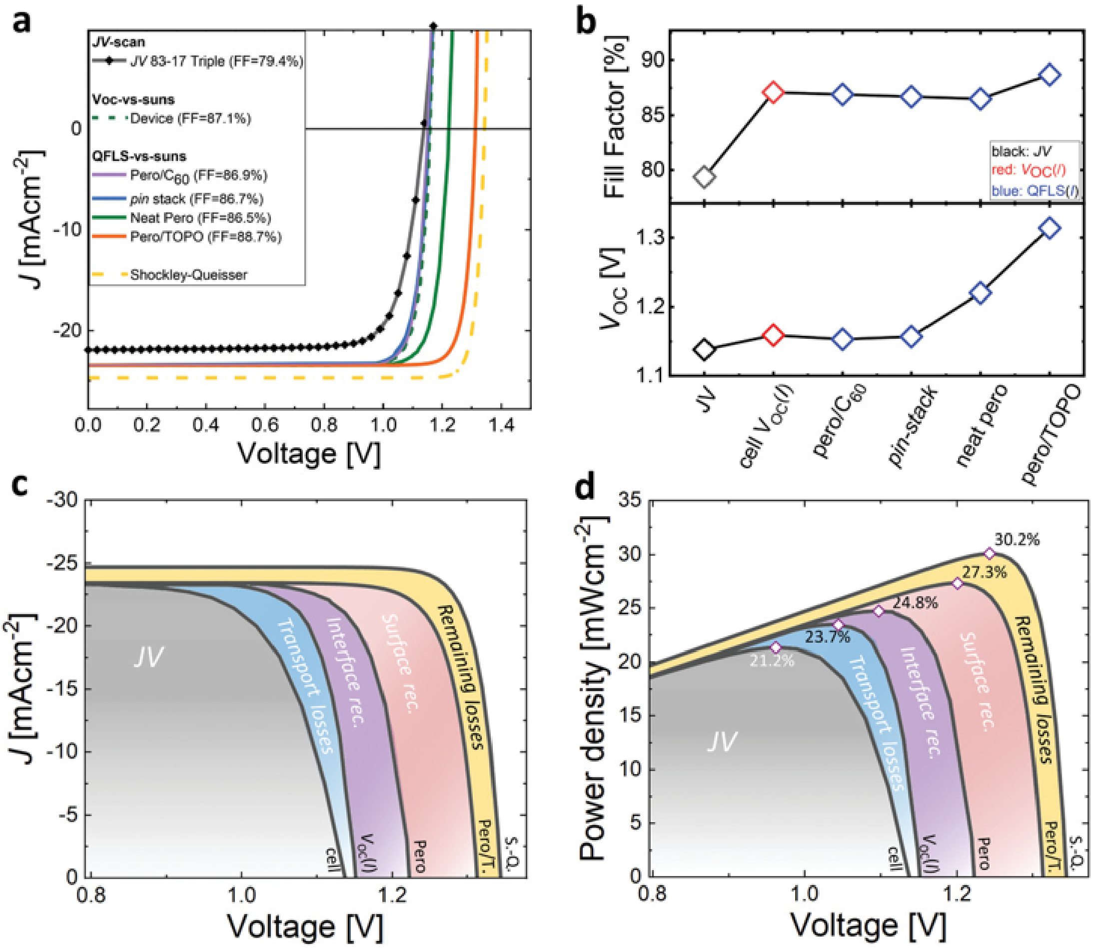

Figure 2.6: a) Current-density versus voltage (J-V) curves of triple cation cells (black line) in comparison to pseudo-JV (pJ-V) curves produced from intensity-dependent V_{OC}(I) and QFLS measurements on plain perovskite, perovskite/C_{60}, optical pin-stack, and full device (solid lines). b) The assumed forward and open-circuit voltages for each film. c,d) J-V curves deciphering the loss mechanisms due to insufficient charge transport (difference between the J-V and pJ-V curves from the intensity-dependent V_{OC}); interfacial losses (difference between the pJ-V curve of the neat material and the optical p-i-n architecture on glass); losses at the perovskite surface (difference between the pJ-V curves of the neat and treated neat materials); and remaining losses in the pass I note that an EQE of 95% was assumed for all J-V and pJ-V curves except the Shockley–Queisser curve in order to focus on FF and V_{OC} losses in this section. Notably, the optical architecture of p-i-n pJ-V curve is virtually similar to the pJ-V curve from V_{OC}(I), and so is omitted from (c) and (d) for simplicity. figure 2.6 d also illustrates the inferred efficiency at the maximum power point for each sample, allowing for the identification of efficiency losses caused by the various recombination processes. Reprinted with permission from [49]. Copyright 2018. Wiley.

Figure 2.7 shows that different architectures have different degradation behavior under operational conditions. In addition, one puzzling observation in degrading high-performance PSCs is the possible presence of "reversible losses" i.e., the efficiency improvement obtained by remeasuring after a recovery process under dark environments as shown in Figure 2.7 a. Figure 2.7 b displays the maximum power point tracking and the stabilized PCE obtained after dark recovery for a typical p-i-n PSC using a state-of-the-art device. Notably, the ageing behavior is symmetric to that of n-i-p PSCs. Under MPP tracking, n-i-p PSCs lose part of their initial efficiency, while the performance of inverted PSCs enhances. Similarly, after storage in the dark for several hours, the n-i-p solar cells recover partially, while inverted PSCs lose efficiency ("reversible behaviors"). This example highlights the significance of creating a new ageing standard that systematically incorporates reversible energy losses/gains under relevant solar cell operating settings, including impacts of day and night cycle, even though the cause of this effect needs more in-depth investigation [53].

To meet the increasing demand for renewable energy, new PV technologies must offer long-term stability except for high power conversion efficiency (PCE). For instance, the lifetime expectation for a PV module in a power plant is 20–25 years, to match the reliability of silicon-wafer-based modules [54, 55]. At present, the long-term operational stability of emerging PV technologies such as organic photovoltaic (OPV) and halide perovskite solar cells (PSCs) is not meeting this target. How to improve the long-term operational stability of devices is stopped by the very limited understanding of the failure of module modes. The existing qualification stability tests defined in the International Electrotechnical Commission (IEC) standards on terrestrial PV modules (such as IEC 61215) are tailored for the silicon panels to screen for well-established degradation mechanisms at the module level [56].

However, emerging PV have fundamentally distinct material properties and advanced device architectures. Thus, these stability test protocols may not be applied to OPV and PSCs. In fact, many studies have confirmed that the operational stability of these devices cannot be fully evaluated by the procedures developed for the silicon panels, which led to a few studies that tried to understand the degradation mechanisms in these emerging PV systems. Unfortunately, the assessment and reporting procedures of these studies are not standardized, which hindered data comparison. This further leads to a failure of investigation for various degradation factors and mechanisms. Regarding such disadvantages, a consensus statement for stability assessment and reporting for perovskite photovoltaic based on the International Summit on Organic Photovoltaic Stability (ISOS) procedures has been suggested [56].

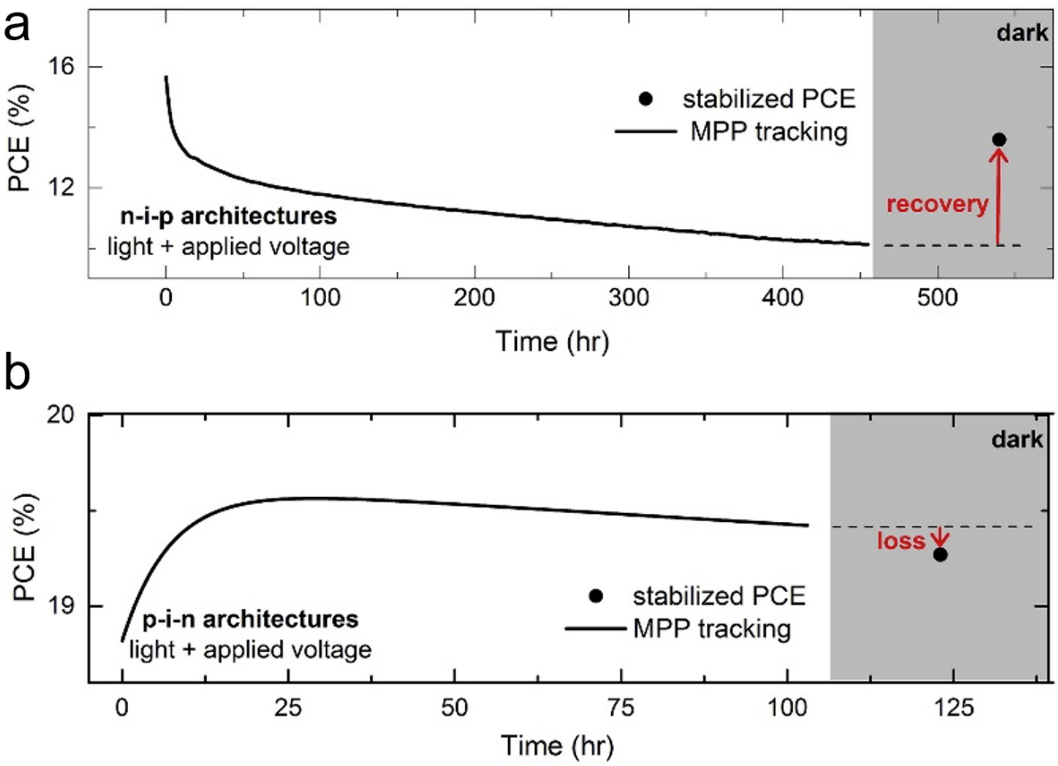

Figure 2.7: Initial Efficiency Losses and Dark Recovery/Losses. (A) Ageing planar and mesoporous regular (or n-i-p) perovskite devices show significant efficiency recovery after resting in the dark ("reversible loss"). The device is left at the open circuit in dark conditions. (B) Planar inverted (or p-i-n) perovskite devices show an initial gain in efficiency and a loss after resting in the dark ("reversible bonus"). The analysis of ageing data for inverted devices is novel and a direct consequence of applying the insights gained for regular device architectures. Reprinted with permission from [53]. Copyright 2018. Elsevier.

3 Device Fabrication

This chapter covers the sample preparation procedures, which are the basis for this thesis. The structure is structured as follows: the basic fabrication protocol for cleaning substrates, the preparation of the hole blocking layer, the perovskite layer, and the electron blocking layer, the electrodes. The descriptions in this section are extracted from the respective publications [57–62].

3.1 Substrate Cleaning

3.1.1 ITO or FTO Substrate

The patterned indium doped tin oxide (ITO from Lumtec, LT-G001) substrates (25 mm × 25 mm) are immersed and washed in diluted Hellmanex® III (2:98 in DI water) solution (Sigma-Aldrich, Z805939-1EA), deionized water, acetone (Carl Roth, 9372.5), isopropanol (Carl Roth, CP41.3) and ethanol (Carl Roth, K928.4) in the ultra-sonication bath for 10 minutes each. Before use, the substrates are executed in an oxygen plasma (0.4 mbar, 168 W, 10 min).

3.2 Hole Blocking Layer

3.2.1 SnO_2 Film

The tin (IV) oxide 15 % in H_2O colloidal dispersion (Alfa Aesar, 44592) is diluted with deionized water with a volume ratio of 1:4, and is shaken for 2 hours at room temperature.

Before spin-coating the diluted tin oxide solutions, the substrates are exposed to oxygen plasma for 10 min with 168 W. The tin oxide solution is spin-coated at 3000 r.p.m. (1000 r.p.m./s) for 30 s, followed by annealing at 150 ℃ for 30 minutes.

3.3 Perovskite Layer

3.3.1 Perovskite Component $(MAPbBr_3)_{0.13}(FAPbI_3)_{0.87}$

The MAFA perovskite solution is prepared by first mixing the powders methylammonium bromide (22.4 mg, Greatcellsolar, MS301000), lead bromide (73.4 mg, Alfa Aesar, A19406), formamidinium iodide (172 mg, Greatcellsolar, MS150000) and lead iodide (485 mg, Sigma-Aldrich, 554359-5G). Then, 640 μL DMF (Acros, 348435000) and 160 μL DMSO (Acros, 348441000) are added to the mixed powders. The obtained mixture is dissolved and stirred at 70 ℃ for 30 minutes, followed by stirring at room temperature for 30 minutes. The solution is used up within 2 hours after preparation.

After the substrates cooled down, the substrates are transferred into a nitrogen-filled glove box. The perovskite precursor is spin-coated on ITO/SnO_2 substrates at 6000 r.p.m. (800 r.p.m./s) for 30 s, and rapidly adding 70 μL chlorobenzene into the center of substrates under a vertical angle at 5 s before ending, followed by 40-60 minutes annealing at 100 ℃.

3.3.2 Perovskite Component $Cs_{0.1}FA_{0.9}PbI_3$

The $Cs_{0.1}FA_{0.9}PbI_3$ perovskite solution was mixed by caesium iodide (31.2 mg, abcr GmbH, AB207757), formamidinium iodide (192.6 mg), and PbI_2 (576.3 mg) in 800 μL DMF and 200 μL DMSO. The obtained solution was stirred at room temperature for 2 hours.

For the $Cs_{0.1}FA_{0.9}PbI_3$ component, one should slowly add 120 μL chlorobenzene into the center of substrates under a vertical angle at 15 s before ending, followed by 15 minutes annealing at 150 ℃.

3.3.3 Perovskite Component p-f-PEAI Doped $(MAPbBr_3)_{0.15}(FAPbI_3)_{0.85}$

A lead excess mixed perovskite precursor solution is prepared by dissolving FAI (1.0 M), PbI_2 (1.05 M), MABr (0.2 M), and $PbBr_2$ (0.2 M) in a mixed solvent of anhydrous DMF and DMSO (4:1, volume ratio). After stirring at 70 °C for 30 min, the perovskite precursor stirs for an additional 30 min at room temperature. One should blend the perovskite power and p-f-PEAI powder to obtain the perovskite precursors with desired p-f-PEAI concentration. The precursors are spin-coated in a nitrogen-filled glove box.

3.3.4 Two Step Perovskite Component Fabrication

599 mg PbI_2 was stirred in a mixed DMF: DMSO (950 μL: 50 μL) solution at 70 ^{o}C for 6 hours. Then, 0.1, 1, and 10 μL deionized water was added to the PbI_2 solution. After that, different PbI_2 solutions were spin coated at 1500 rpm for 30 s on substrates. Then, substrates were placed on the hot plate for a 30 s annealing at 70 ^{o}C. Next, a mixed solution prepared by FAI:MAI:MACl (60 mg: 6 mg: 6 mg) power dissolved in 1 ml of 2-propanol spin coated on PbI_2 films with a 1500 rpm with a 20 min storage in a nitrogen-filled glove box before annealing. Then, obtained films were annealed at 150 ^{o}C for 15 min under an air atmosphere (relative humidity with 30 – 40 %).

3.4 Electron Blocking Layer

The spiro-OMeTAD solution is mixed of spiro-OMeTAD (72.3 mg, Sigma-Aldrich, 902500), 1 mL chlorobenzene (Acros, 443001000), 17.5 μL Li-TFSI (520 mg/mL ,Sigma-Aldrich, 544094) in acetonitrile (Sigma-Aldrich, 2710004), and 28.8 μL 4-tert-butylpyridine (Sigma-Aldrich, 142379).

When the substrates are cooled down, one should dynamically spin-coat spiro-OMeTAD solution on ITO/SnO_2/perovskite substrates at 4000 r.p.m for 20 s. Then, all the substrates are stored in a dark-desiccator with silica gel (< 10 % relative humidity) for 24 hours to increase the conductivity of the spiro-OMeTAD layer.

3.5 Metal Electrodes

An 80 nm thick Au layer was evaporated on the spiro-OMeTAD layer with 2 nm (0.2 Å/s) and 78 nm (1.2 Å/s) at a pressure of 10^{-5} bar.

4 Characterization Methods

In this section, the characterization methods are summarized in 4 parts: 1) spectroscopic and electronic methods (UV-vis spectroscopy, X-ray photoelectron spectroscopy, photoluminescence spectroscopy, time-resolved photoluminescence spectroscopy, transient absorption spectroscopy, solar cells performance, external quantum efficiencies); 2) operando grazing incidence small/wide angle X-ray scattering; 3) morphology characterization (scanning electron microscopy); 4) theoretical simulation (density function theory and drift-diffusion simulation). The descriptions in this section are extracted from the respective publications [57–59].

4.1 Spectroscopic and Electronic Characterization

Two functions are served by spectroscopic and electronic characterisation methods: On the one hand, fundamental material properties such as absorption behaviour aid in evaluating the quality of thin films and their potential for photovoltaic devices; on the other hand, photovoltaic characterization, i.e. current-voltage sweeps under the simulated sunlight, is critical for verifying the tested materials' functionality in their aimed application or identifying new research directions.

4.1.1 UV-vis Spectroscopy

UV-Vis spectroscopy could calculate the amount of light absorbed by materials by comparing the intensity of light passing through a sample to that passing through a reference sample or blank. This method is applicable to many materials, including liquids, solids, thin films, and glass.

Measurements of UV–vis spectroscopy were carried out using a PerkinElmer Lambda 650S for this study [63]. Two lights are included in the instrument: A deuterium lamp produces light in the ultraviolet (UV) spectrum beginning at 190 nm, while a tungsten-halogen lamp produces light from the visible zone to the near-infrared zone up to 900 nm. The reflecting monochromator composes of a mirror for switching the required light source at 319.3 nm. Monochromatic light is produced by the combination of a filter wheel assembly, collimating mirrors, and a holographic grating with 1440 lines/mm. The obtained signal has a resolution of 0.17 nm and an accuracy of 0.15 nm after passing through a slit typically set to 2 nm width [64].

The sample and reference beams are separated by using a beam splitter (chopper running at 46 Hz). The sample is placed for both the transmission geometry and the reflection geometry of a 150 mm diameter integrating (Ulbricht) sphere whose white covering acts as a diffuse reflector (Lambertian surface) and evenly distributes dispersed light from the sample to all other places inside. An R955 photo-multiplier acts as a detector for the difference between the reference beam coming from the side. An auto-zero (empty beam) measurement is made before each series of measurements to calibrate the instrument in its standard configuration. The measurements are fixed at a scanning rate of 266.75 nm/min, and the observed intensity is compared to the empty beam measurement by using commercial software [64].

4.1.2 X-ray Photoelectron Spectroscopy

The X-ray photoelectron spectroscopy characterization in this thesis collaborates with Fujian Institute of Research on the Structure of Matter, Chinese Academy of Science.

Photoelectric effects on the surface of materials induced by X-ray could be used to analyse the elements, relative chemical components and their chemical states. Such a technique is developed for X-ray photoelectron spectroscopy (XPS). Also, it could be used to characterize the electronic structure and the electronic state density in the materials. XPS could efficiently identify both the elements present and related elements. Especially, this technique combines with ion-beam etching, and this makes it possible for a line or a depth profile for the material instead of a surface-sensitive feature. In most studies, this technique is used to study the chemical reactions for many situations when the samples are cut, exposed to heat, sensitive gases or solution, ultraviolet radiation and so on [65].

The chemical composition of films in this work was measured using XPS (Kratos Ultra) with an Al K α radiation source 1486.6 eV, and all the binding energies were calibrated by referencing the Fermi level and Au 4f peak position of the Ar ion sputter-clean gold foil.

4.1.3 Photoluminescence Spectroscopy

The photoluminescence spectroscopy characterization collaborates with the Department of Chemistry, University of Munich (LMU).

Materials absorb photons with a higher energy level than electrons in materials, the materials could emit photons. Such a phenomenon is named photoluminescence. After the electrons' excitation process, more photons would be re-radiated due to different relaxation processes. The photons absorption and radiation processes could happen at a femtoseconds (fs) level for many inorganic semiconductors. While such processes could spend milliseconds (ms) due to the phosphorescence processes for molecules. Even in some extreme situations, the relaxation processes could last for minutes or hours. The steady-photoluminescence spectra are usually used to characterize the bandgap of materials [66].

In this thesis, photoluminescence spectroscopy was performed with a Picoquant Fluotime 300 spectrofluorometer, using an excitation wavelength of 370 nm.

4.1.4 Time-resolved Photoluminescence Spectroscopy

The time-resolved photoluminescence (TRPL) spectroscopy characterization collaborates with the Department of Chemistry, University of Munich (LMU).

TRPL is usually used to investigate quick electrical deactivation processes which produce radiative photons for materials. The lifetime of molecules could locate at a few picoseconds (ps) or nanoseconds (ns). The environments like solvent, temperature or atmosphere could affect the lifetime of radiative photons. Förster Resonance Energy Transfer, quenching, solvation dynamics, and molecule rotation could dominate the decay kinetics. Hence, the changes in decay processes regarding both lifetime and kinetics could reflect the surrounding atmosphere information or offer information for the reaction kinetics [67]. For semiconductor materials like perovskite materials, TRPL with fluence-dependent measurements could offer the non-radiative recombination rates k_1 and radiative recombination k_2.

In this thesis, TRPL spectroscopy was performed with a Picoquant Fluotime 300 spectrofluorometer, using an excitation wavelength of 370 nm.

4.1.5 Transient Absorption Spectroscopy

Transient absorption spectroscopy (TAS) characterization in this thesis collaborates with Cavendish Laboratory, University of Cambridge.

Ultrafast TAS could observe the changes of absorbance/transmittance for samples with the feature of non-linear spectroscopy. After the excitation of pulsed light, the absorbance of samples decays as a function of time at specific wavelength ranges. For experiments, a combination of the 'pump' light and the 'probe' light aimed to measure the absorbance of materials produced by pulsed fs or ns lasers would have different values, which indicates ground state bleaching. If the investigated processes are slow, a continuous probe light or an accumulation for spectrophotometric procedures would be suggested to enhance noise-to-signal ratios. In addition, TAS could also be measured as a function of time, and this could also offer decay kinetics for materials. Compared with TRPL, TAS could detect the dark states of materials, which can not be observed by TRPL [68].

The femtosecond 400 nm pump and white-light probe were used as the illumination source for light soaking. The white light continuum generated by a non-collinear optical parametric amplifier consisted of a visible pulse light between 520 nm and 780 nm operated at a 1 kHz repetition rate, with an average power of 400 μW. The white-light pulse was equally divided into probe and reference, before being focused onto the sample to an effective beam radius of 100 μm, corresponding to energy per pulse of 630 $\mu\text{J} \cdot cm^{-2}$ for each split beam and a carrier density of 10^{20} cm^{-3} at the perovskite film.

The sample film was loaded into a cube cell with spectroscopic windows on the front and back in a glove box. Before the optical measurements, the cell was connected to a vacuum pump (HiCube 80 Eco), being pumped overnight in the dark until the pressure stabilized at 3.4×10^{-3} Pa. The vacuum pump was kept working continuously during the measurement to ensure stable pressure. The visible broadband beam was generated in a home-built non-collinear optical parametric amplifier and the white light was split into two separate beams, one probe and one reference beam. The 400-nm pump beam was created by sending the 800-nm fundamental beam of the Solstice Ace through a second harmonic generating beta barium borate crystal of 1 mm thickness (Eksma Optics). The pump was blocked by a chopper wheel rotating at 500 Hz while a computer-operated a mechanical delay stage to adjust the delay between the pump and the probe. The transmitted probe and reference pulses were collected by a silicon dual-line array detector (Hamamatsu S8381-1024Q), which was driven and read out by a custom-built board (Stresing Entwicklungsbüro).

4.1.6 Solar Cells Characterization

The current-voltage curves of solar cells could be characterized by changing a variable resistor across the cell and measuring the voltage and current for the whole device. Although this is relatively simple, it is time-intensive and wire resistance sensitive. Hence, more complicated electronics are employed in practice. The most typical approach is to employ a changeable voltage source like Keithley source meters that can also sink current. To increase accuracy, I_{SC} and V_{OC} are frequently measured independently from the rest of the curve (by setting the voltage and current to zero, separately). The I-V curve has a steeply fluctuating slope, which poses extra issues. Hence, programming the voltage steps of solar cells properly is critical to achieving reliable results [69].

The current density-voltage (J-V) data were recorded using a Keithley 2611B source meter under the illumination of the solar simulator (class ABA, LOT-Quantum design GmbH) with a light intensity of 100 mW cm^{-2}, which was calibrated with a reference solar cell (Fraunhofer ISE019-2015). The solar cells were measured with a scanning speed of 50 mVs^{-2} (voltage step of 10 mV and integration time of 100 ms). There were 6 (or 8) gold top electrodes with a dimension of 2.5×10.0 mm (or 3.5×10.0 mm) for each substrate on a substrate with a size of 25×25 mm. The active area was controlled by a metal shadow mask (0.12 or 0.19 cm^2) to avoid overestimation of the photocurrent.

4.1.7 External Quantum Efficiencies

The proportion between total change carriers gathered by the solar cells to the number of total photons illuminated on the solar cells with certain energy is regarded as the external quantum efficiency (EQE). The EQE spectra are usually shown as a function of wavelength or energy (see Figure 7.18). In solar cells, all photons from sunlight with energy above the bandgap of materials could be totally absorbed, and all produced charge carriers are collected, the EQE of solar cells would be one at the specific wavelength. For photons from sunlight with energy lower than the bandgap of materials, the EQE of solar cells at this wavelength would be zero [70].

The external quantum efficiencies (EQEs) were measured by Oriel® Quantum Efficiency Measurement Kit from the Newport company. The light source spectrum response was calibrated by the silicon detector. The measurements were performed using the Oriel Instruments QEPVSI-b system with a Xenon arc lamp (Newport 300 W, 66902) chopped at 30 Hz and a monochromatic instrument (Newport Cornerstone 260). The EQE intensity was measured and normalized in the wavelength range of 350 to 900 nm.

4.2 Operando Grazing Incidence Small/Wide Angle X-ray Scattering

4.2.1 Conditions of the Synchrotron Radiation-based Operando Grazing-incidence X-ray Scattering Methods

The operando grazing-incidence wide-angle X-ray scattering (GIWAXS) studies on the MAFA PSCs were done via the ISOS-L-1I protocol (with continuous voltage-bias scan and illumination) to unify the experimental assessment. ISOS-L-1I stands for the intrinsic photo-stability at room temperature (similar to ISOS-L-1 except that the atmosphere is inert). The pressures were kept at 5×10^{-1} Pa for the vacuum condition and 1.01×10^{5} Pa for a pure nitrogen atmosphere, respectively. The entire operando measurement chamber was stabilized at 25.0 ± 0.7 °C with a water-cooling system, which was monitored by an infrared thermometer.

4.2.2 Operando GIXS Technology

The operando experiments were executed at beamline P03 at Deutsches Elektronen-Synchrotron (DESY, Hamburg) during two separate beamtimes to ensure reproducibility. The wavelength of the monochromatic X-ray beam was set to 11.65 keV and 11.70 keV to avoid the absorption edge of lead (around 13 keV) and thus minimize X-ray radiation damage. 2D GIWAXS data were collected at an incident angle of 0.4° with Pilatus 300K (Dectris Ltd., pixel size 172 μm) and LAMBDA 4.5M (X-Spectrum GmbH, pixel size 55 μm) detectors. 2D GISAXS data were collected at the same incident angle (0.4°) with Pilatus 1M and Pilatus 300K detectors. The parameters of beam center and the sample-to-detector distance (SDD) of GISAXS detector images were calibrated via fits of the patterns of LaB_6 powders using the DPDAK package. The parameters of beam center and the sample-to-detector distance of GIWAXS detector images were calibrated via fits of the patterns of CeO_2 powders using the DPDAK package. The GISAXS detector images were further treated via the DPDAK package based on Python 2.7 [71]. The reciprocal q-space GIWAXS scattering images, the line cuts and azimuthal integrations of the scattering data were obtained with the GIXSGUI MATLAB plug-in [17]. To calibrate the intensity of different scattering images, one should normalize it to the ionization energy of the incident X-ray beam for each frame.

4.3 Morphology Characterization

4.3.1 Scanning Electron Microscope

All SEM measurements in the present thesis are performed at Walter-Schottky-Institut/ZNN of TU Munich.

The scanning electron microscope as one type of electron microscope can offer the surface images of materials by scanning of focused stream of electrons on the sample surfaces. Through the interaction between the electron beam and the atoms in samples, the surface morphology and element composition of samples can be detected. For creating one image, the SEM combines the beam location and the received signal intensity together by scanning a raster scan pattern. Generally, atoms stimulated by the electron beam would emit secondary electrons, which would be collected by a secondary electron detector, namely, the Everhart–Thornley detector. The received number of secondary electrons determines the signal intensity of samples, which is highly dependent on the morphology of samples. In addition, some SEM could achieve resolutions better than 1 nm by optimizing various factors such as the electron spot size, and interactions between the volume of the electron beam and the sample [72].

In this work, the surface morphology was probed with a field-emission scanning electron microscopy (SEM, Zeiss NVision 40) with an acceleration voltage of 5 kV at a working distance of 3.5 mm, and an aperture size of the primary electron gun at around 10 μm.

All data are collected with the software SmartSEM.

4.4 Theoretical Simulation

Density Function Theory

In the physics, chemistry, and materials science fields, density-functional theory (DFT) is a computational quantum mechanical modelling method. DFT is widely used to examine the electronic structure (or nuclear structure), particularly the ground state, of many-body systems, primarily atoms, molecules, and condensed phases. According to this theory, functionals may determine the properties of a many-electron system. Thus, the many-body systems could be explained by functions or functions of another function. Spatially dependent electron density dominates the functionals of the DFT [73].

Computational Methods. The Gibbs free energy of the mixed cation and mixed halide hybrid perovskite $(\mathrm{MAPbBr_3})_x\,(\mathrm{FAPbI_3})_{1-\mathrm{x}}$ was evaluated via

$$\Delta G(x) = \Delta U(x) - T\Delta S(x) + P\Delta V \tag{4.1}$$

where the $\Delta U(x)$ and $\Delta S(x)$ are mixing energy and entropy of alloys. T, P and Δ V are the temperature, pressure and the change in the volume of the system. The mixing energy Δ U(x) is defined as:

$$\Delta U(x) = U_x - (1-x)U_{FAPbI_3} - xU_{MAPbBr3} \tag{4.2}$$

where U_x, U_{FAPbI_3} and U_{MAPbBr_s} are the calculated DFT total energies per formula unit of $(\mathrm{MAPbBr})_3)_2\,(\mathrm{FAPbI_3})_{1-\pi}$ and the pure $\mathrm{FAPbI_3}$ and $\mathrm{MAPbBr_3}$, respectively. The mixing entropy was

$$\Delta S(x) = -k_B[x\ln x + (1-x)\ln(1-x)] \tag{4.3}$$

in which $\mathrm{k_B}$ is the Boltzmann constant. Without the P Δ V term, the expression of free energy is

$$\Delta F(x) = \Delta U(x) - T\Delta S(x) \tag{4.4}$$

where $\Delta U(x)$ and Δ S(x) follow from the Equations (9) and (10). The free energy upon illumination was estimated following the method mentioned in literature [74, 75]. We assumed that when $(\mathrm{MAPbBr}_3)_{\mathrm{x}}(\mathrm{FAPbI}_3)_{1-\mathrm{x}}$ was under illumination, pairs of photo-generated charge carriers were generated uniformly in the material at a density (per formula unit) n, then the free energy becomes

$$\Delta U_x^* = \Delta U_x + nE_g(x) \mid \tag{4.5}$$

for the unmixed state $(1-x)\mathrm{FAPbI}_3 + x\mathrm{MAPbBr}_3$, it was assumed that all charge carriers funnel into the FAPbI_3, so the total energy of photoexcited FAPbI_3 becomes

$$\Delta U_{P_A}^* = \Delta U_{F_A} + n\frac{1}{1-x}E_g^{FA} \tag{4.6}$$

using Egs. (10) and (11) in Eq. (7), with U_z and U_{FA} substituted by U_x^* and U_{FA}^*. We obtained

$$\Delta U^*(x) = \Delta U(x) + n\left(E_g(x) - E_g^{FA}\right) \tag{4.7}$$

The free energy of mixing of $(\mathrm{MAPbBr}_3)_{\mathrm{P}}(\mathrm{FAPbI}_3)_{1-\pi}$ under the photo illumination becomes

$$\Delta F^*(x) = \Delta F(x) + n\left(E_g(x) - E_g^{FA}\right) \tag{4.8}$$

The slope of ΔF_{mix} referred to the phase stability of materials:

$$\Delta F_{\mathrm{epp}} = \frac{\sigma^2 \Delta F_{\mathrm{mix}}}{\sigma x^2} \tag{4.9}$$

which indicated that mixed phases maintained stable when the curvature was convex ($0 < x < 0.2$ in this case), while mixed phases started to separate when the curvature was concave ($0.2 < x < 1$ in this case).

The DFT calculations were performed using the Vienna Ab initio Simulation Package (VASP). A revised Perdew-Burke-Ernzerhof generalized gradient approximation functional was used for the exchange-correlation functional. The supercell method was employed for the simulation of the alloy $(\mathrm{MAPbBr}_3)_x(\mathrm{FAPbI}_3)_{1-x}$ ($x = 0.2, 0.3, 0.5, 0.8$). Accordingly, $1\times5\times1, 2\times2\times1, 2\times5\times1$ supercells were constructed for x $= 0.2(0.8), 0.5, 0.7$.

Drift-diffusion Simulation

The gradient difference of charge carriers (holes or electrons) in semiconductor materials under external stimuli like light, heat or electricity could produce the current to flow through a semiconductor. This process is named diffusion. By contrast, the drift current is caused by the migration of charge carriers as a result of the force placed on them by an electric field. Diffusion currents may flow in the same direction as or opposite to drift currents. Thus, for simulating the operational conditions of semiconductors, one has to consider both the drift and diffusion of charge carriers for a reliable simulation [76].

The drift–diffusion equation describes the diffusion and drift currents in combination as below:

Poisson Equation:

$$\frac{\partial}{\partial x}\left(\varepsilon(x)\frac{\partial\psi}{\partial x}\right) = -\frac{q}{\varepsilon_0}\cdot\left[-n + p - N_A^- + N_D^+ + \frac{1}{q}\rho_{def}(n,p)\right] \tag{4.10}$$

Continuity:

$$-\frac{\partial j_n}{\partial x} + G - U_n(n,p) = \frac{\partial n}{\partial t} \tag{4.11}$$

$$-\frac{\partial j_p}{\partial x} + G - U_p(n,p) = \frac{\partial p}{\partial t} \tag{4.12}$$

Constitutive relations:

$$j_n = -\frac{\mu_n}{q}\frac{\partial E_{Fn}}{\partial x} \tag{4.13}$$

$$j_p = -\frac{\mu_p}{q}\frac{\partial E_{Fp}}{\partial x} \tag{4.14}$$

In these equations: n and p indicates free carrier concentrations; $\rho_{def}(n,p)$ indicates defect distributions; N_A^- *and* N_D^+ indicates charged dopants; j_n *and* j_p indicates the electron and hole current densities; $U_(n,p)$ indicates the net recombination rates; G indicates the generation rate; μ_n and μ_p indicate the mobility of charge carriers; $E_{Fn,Fp}$ indicates the quasi-Fermi level of materials.

In this work, I use SCAPS-1D (a Solar Cell Capacitance Simulator) to build the device model as an n-i-p structure of PSCs [77]. Detailed parameters are illustrated in Tables 4.1 to 4.8 and extracted from the literature [59].

Table 4.1: ITO parameters

Description	Parameters
Electron mobility in ITO ($cm^2/(Vs)$)	10^7
Hole mobility in ITO ($cm^2/(Vs)$)	10^5
Metal work function (eV)	4.7
Relative to E_f(eV)	0.4
Relative to Ey or Ec_s(eV)	0.4596

Table 4.2: SnO_2 parameters

Description	Parameters
Thickness (nm)	20
Bandgap (eV)	3.7
Electron affinity (eV)	4.3
Dielectric permittivity (relative)	10
CB effective density of state ($1/cm^3$)	10^{18}
VB effective density of state ($1/cm^3$)	10^{20}
Electron thermal velocity (cm/s)	10^7
Hole thermal velocity (cm/s)	10^7
Electron mobility ($cm^2/(Vs)$)	230
Hole mobility (cm^2/Vs))	21

Table 4.3: Perovskite parameters

Description	Parameters
Thickness (nm)	600
Bandgap (eV)	1.6
Electron affinity (eV)	3.9
Dielectric permittivity (relative)	23
CB effective density of state ($1/cm^3$)	7.79×10^{18}
VB effective density of state ($1/cm^3$)	2.37×10^{20}
Electron thermal velocity (cm_s)	10^7
Hole thermal velocity (cm/s)	10^7
Electron mobility ($cm^2/(Vs)$)	22
Hole mobility ($cm^2/(Vs)$)	22
Effective mass of electrons	0.1
Effective mass of holes	0.21
Radiative recombination coefficient (cm^3/s)	3.16×10^{-12}

Table 4.4: Spiro-OMeTAD parameters

Description	Parameters
Thickness (nm)	200
Bandgap (eV)	3.1
Electron affinity (eV)	2.1
Dielectric permittivity (relative)	4
CB effective density of state ($1/cm^3$)	2.5×10^{18}
VB effective density of state ($1/cm^3$)	1.8×10^{19}
Electron thermal velocity $\big(cm_{s)}$	10^7
Hole thermal velocity (cm/s)	10^7
Electron mobility ($cm^2/(Vs)$)	0.02
Hole mobility ($cm^2/(Vs)$)	0.02

Table 4.5: Gold parameters

Description	Parameters
Electron mobility in ITO	10^5
Hole mobility in ITO	10^7
Metal work function (eV)	5.6
Relative to E_f	-0.4
Relative to Ev or E_g	-0.4749

Table 4.6: Perovskite/SnO_2 interface parameters

Description	Parameters
Capture cross section electrons (cm^2)	10^{-19}
Capture cross section holes (cm^2)	10^{-17}
Total density (integrated over all energies) ($1/\mathrm{cm}^2$)	10^{11}

Table 4.7: Perovskite/Spiro-OMeTAD interface parameters

Description	Parameters
Capture cross section electrons (cm^2)	10^{-17}
Capture cross section holes (cm^2)	10^{-19}
Total density (integrated over all energies) ($1/\mathrm{cm}^2$)	10^{11}

Table 4.8: $\mathrm{PbI_2}$ parameters

Description	Parameters
Thickness (nm)	2
Bandgap (eV)	2.2
Electron affinity (eV)	3.4
Dielectric permittivity (relative)	4
CB effective density of state ($1/\mathrm{cm}^3$)	2.5×10^{18}
VB effective density of state ($1/\mathrm{cm}^3$)	1.8×10^{19}
Electron thermal velocity (cm / s)	10^7
Hole thermal velocity (cm/ s)	10^7
Electron mobility ($\mathrm{cm}^2/(\mathrm{Vs})$)	0.02
Hole mobility ($\mathrm{cm}^2/(\mathrm{Vs})$)	0.02

5 Bulk Passivation for Perovskite Solar Cells

This chapter is extracted from the published article: Tailoring the orientation of perovskite crystals via adding two-dimensional polymorphs for perovskite solar cells (Guo, Renjun, et al., Journal of Physics: Energy 2.3 (2020): 034005, DOI: https://doi.org/10.1088/2515-7655/ab90d0). Reproduced from reference [57] with permission from IOP Publishing Ltd, copyright 2020.

Organic-inorganic perovskite materials are attracting increasing attention for their use in high-performance solar cells due to their outstanding properties, such as long diffusion lengths, low recombination rate and tunable bandgap. Finding an effective method of defect passivation is thought to be a promising route for improvements towards narrowing the distribution of the power conversion efficiency (PCE) values, given by the spread in the PCE over different devices fabricated under identical conditions, for easier commercialization. In this work, I add 2-(4-fluorophenyl)ethyl ammonium iodide (p-f-PEAI) into the bulk of mixed cation lead halide perovskite thin film. I investigate the influence of different p-f-PEAI concentrations on the optical properties, morphology, crystal orientation, charge carrier dynamics and device performance. I observe that introducing the proper amount of p-f-PEAI changes the preferential orientation of the perovskite crystals, promotes the strength of crystal textures, and suppresses non-radiative charge recombination. Thus, I obtain a narrower distribution of the PCE of perovskite solar cells without sacrificing reached PCE values. This is an important step toward better reproducibility on the way towards the commercialization of perovskite solar cells.

5.1 Background

Today, organic-inorganic halide perovskites have become one of the most attractive photovoltaic materials due to their excellent optoelectronic properties and low-temperature fabrication processability [78–81]. The power conversion efficiency (PCE) of single-junction perovskite solar cells (PSCs) started at 3.8 % in 2009 and reached certified 25.2 % in 2019 [31, 82]. Although this tremendous progress has been achieved, the spread of the PCE over different devices fabricated under identical conditions is limiting the potential commercialization of this type of emerging solar cell.

Previous studies suggested that the distribution of the PCE of solar cells is related to the recombination process in the bulk, at the grain boundaries and the interfaces of the light-harvesting layer [83]. Due to having commonly polycrystalline perovskite films, these films contain substantial structural disorders, such as grain boundary defects and crystallographic defects [84]. From the literature, theoretical studies indicate that trap-assisted defects dominate the distribution of the PCE over different devices under identical conditions, whereas several experiments show that suppressing defects in perovskite films is essential for enhancing the performance of PSCs [85, 86]. Mixed cation lead halide perovskites such as $(MAPbBr_3)_{0.13}(FAPbI_3)_{0.87}$ enabled PSCs with high efficiency and notable stability, which both will be needed in real-world devices [87]. Thus, in the present work, I focus on mixed cation lead halide perovskite $(MAPbBr_3)_{0.13}(FAPbI_3)_{0.87}$.

Among the routes to increase the distribution of the PCE of PSCs, the method of using two-dimensional polymorphs for passivating 3D perovskite films appears very promising. Phenylethyl ammonium iodide (PEAI) became one of the most important materials to improve the PCE of PSCs [88, 89]. From density function theory based calculations Zhou et al. speculated that 2-(4-fluorophenyl)ethyl ammonium iodide (p-f-PEAI) was passivating defects and thereby increasing the device performance [90]. Encouraged by this work, I introduce p-f-PEAI into the bulk of $(MAPbBr_3)_{0.13}(FAPbI_3)_{0.87}$ perovskite films to enhance the distribution of the PCE while maintaining the performance of PSCs in terms of maximum PCE at the same time. When p-f-PEAI reacts with PbI_2 or $PbBr_2$, it forms $(p-f-PEAI)_2Pb(I_xBr_{1-x})_4$ which is called a 2D perovskite.

In contrast, our original component $(MAPbBr_3)_{0.13}(FAPbI_3)_{0.87}$ is a 3D perovskite. I tune the p-f-PEAI-to-MA/FA mixing ratio by substituting different amounts of MA/FA (fixed at a molar ratio of 0.15:0.85 in the initial solution) with p-f-PEAI cations. I use grazing-incidence wide-angle X-ray scattering (GIWAXS) to analyze the orientation changes of doped perovskite crystals caused by adding different amounts of p-f-PEAI [30]. Moreover, I use time-resolved photoluminescence (PL) to investigate the charge carrier dynamics in mixed cation lead halide films with different concentrations of p-f-PEAI [91]. The results show that 3D perovskites doped with p-f-PEAI exhibit not only a stronger preferential orientation of the perovskite structure but also show an improved distribution of the PCE in devices. In the present study, I achieved a champion device efficiency of 18.4 % alongside a substantially improved distribution of the PCE.

5.2 Light Absorption and Photoluminescence Spectra

Figure 5.1 (a) shows the UV-vis spectra of the perovskite films coated on ITO glasses for different doping concentrations including the reference sample (x= 0.00). The concentration x= 0.02 results in improved absorption as compared with the reference. Further increasing the amount of the p-f-PEAI increases the absorption for the probed wavelength range [92]. At a concentration of x= 0.08, an absorption peak occurs at around 540 nm due to the formation of the $(p-f-PEAI)_2Pb(I_{0.85}Br_{0.15})_4$ phase. The PL spectra of doped p-f-PEAI films show a redshift of the emission peak wavelength. Compared with the reference sample, it shifts from 760 nm (x= 0.00) to 785 nm (x= 0.08). It is well-known that redshift to 840 nm is beneficial for the light-harvesting of perovskite solar cells under AM 1.5G conditions due to the increasing absorption of sunlight [93]. The formation of the $(p-f-PEAI)_2Pb(I_{0.85}Br_{0.15})_4$ phase causes an extended tail-absorption in near ultra-violet spectrum. However, I do not observe a second PL peak in the steady-state PL spectra corresponding to the peak located at around 540 nm in the absorption spectrum of the sample with the concentration of x= 0.08. The absence of this peak in the PL data could result from strong non-radiative recombination centers in the $(p-f-PEAI)_2Pb(I_{0.85}Br_{0.15})_4$ phase so that the hole-electron pairs are recombining immediately after formation.

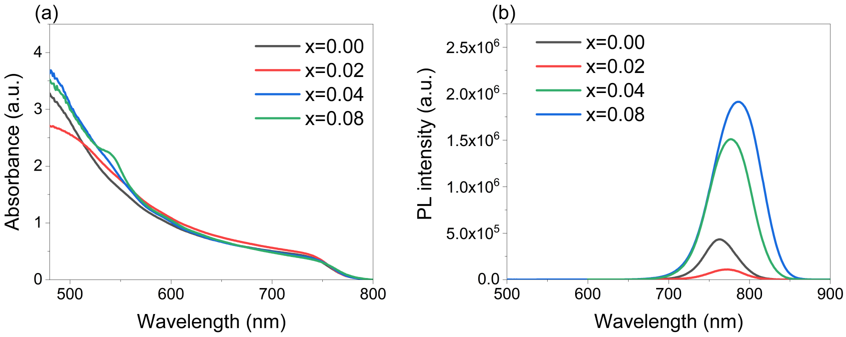

Figure 5.1: Figure.1 (a) UV-Vis spectra and (b) Photoluminescence (PL) spectra of p-f-PEAI doped mixed cation lead halide perovskite $(MAPbBr_3)_{0.13}(FAPbI_3)_{0.87}$ films with concentrations x=0.00 (black), 0.02 (red), 0.04 (blue), and 0.08 (green). Reprinted with permission from [57]. Copyright 2019, IOP Publishing.

5.3 Surface Morphology

To evaluate the effect of our passivation strategy on the morphology of the perovskite films, I perform scanning electron microscopy (SEM) measurements. Figure 5.2 illustrates the changes in the surface structures for the different p-f-PEAI concentrations. With increasing the amount of p-f-PEAI, the size of the perovskite crystals decreases, and the size distribution narrows. At a concentration x=0.08, the distribution of crystal sizes is narrowest showing that adding p-f-PEAI is beneficial for homogenizing the crystal sizes. The real grain structure shows a dense, pinhole-free morphology in term of all films. The statistical grain size distribution is shown in Figure 5.3.

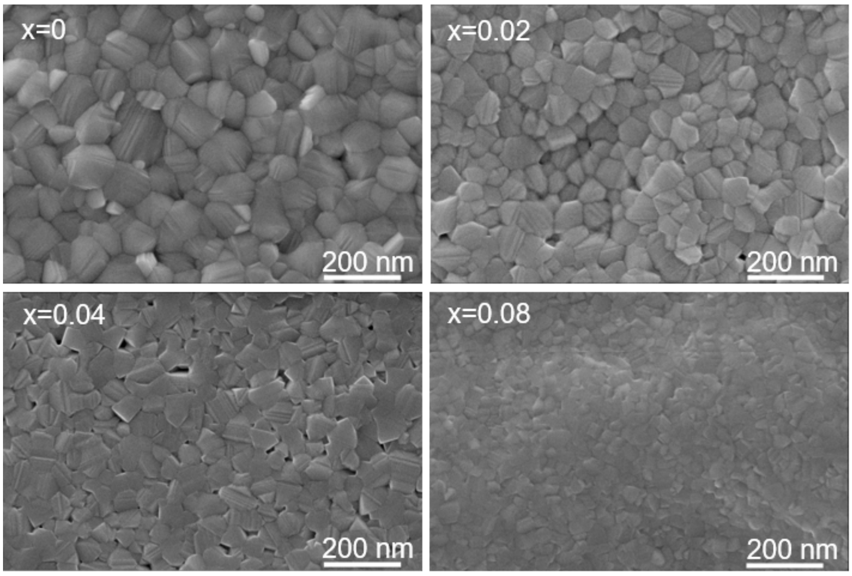

Figure 5.2: SEM images showing surface structures of post-annealed films with different p-f-PEAI concentrations as indicated, grown on ITO substrates. Reprinted with permission from [57]. Copyright 2019, IOP Publishing.

5.4 Structure Analysis

To investigate the structural changes in the different perovskite films and to confirm the formation of $(p-f-PEAI)_2Pb(I_{0.85}Br_{0.15})_4$ phases with increasing the amount of p-f-PEAI, I characterize the perovskite films with grazing-incidence wide-angle X-ray scattering (GIWAXS). Figure 5.4 (a)-(d) shows reshape and corrected 2D GIWAXS data. For further analysis, an azimuthal integration of the 2D GIWAXS data is done. The resulting data are shown in Figure 5.4 (e). At a concentration of x= 0.08, the formed

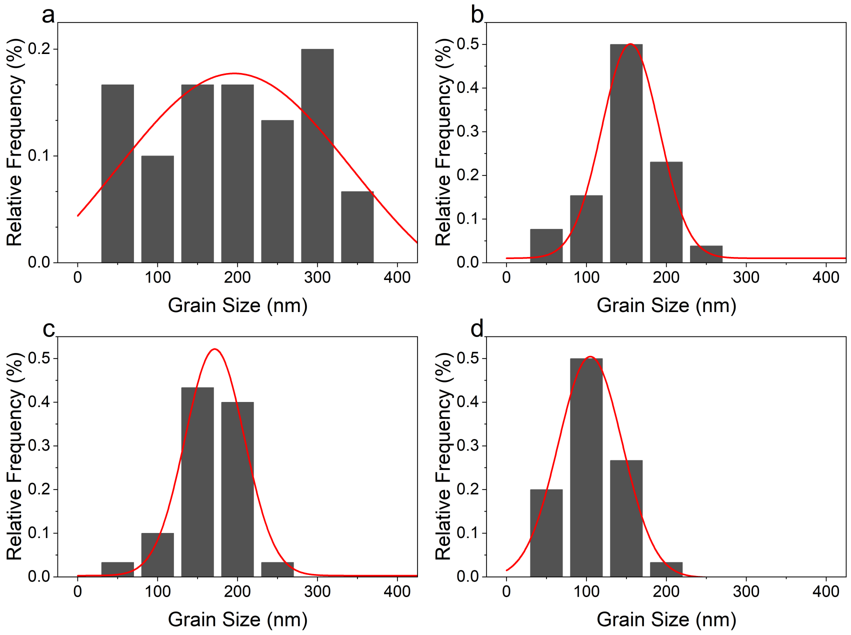

Figure 5.3: Grain size of post-annealed films with different p-f-PEAI concentrations (a) x= 0.00, (b) x= 0.02, (c) x= 0.04, (d) x= 0.08 determined from the SEM images. Reprinted with permission from [57]. Copyright 2019, IOP Publishing.

$(p-f-PEAI)_2Pb(I_{0.85}Br_{0.15})_4$ phase is still visible at q= 0.3 nm^{-1}.

In contrast, at lower concentrations, the scattering data do not show Bragg peaks of the 2D perovskite. As seen in the tube cuts of the (001) perovskite, Bragg peak from the 2D GIWAXS data and the corresponding Gaussian fit (Figure 5.4(f)), an extremely small amount of p-f-PEAI can already result in a new face-on texture formation for the cubic phase of perovskite films as seen in the (001) Bragg peaks. Thus, parts of the crystals have (001) crystal planes oriented parallel to the substrate, while the original edge-on texture component still persists. Therefore, the addition of p-f-PEAI can change the preferential orientation of perovskite crystals inside the film but still maintains the original texture. With the increasing amount of p-f-PEAI, the preferential textures of the (001) Bragg peaks of the perovskite films do not change anymore, while the strength of both, edge-on and face-on preferential orientation increases.

The XRD data confirms the consumption of excess PbI_2 due to the addition of p-f PEAI as well as the formation of the 2D perovskite phase with the increasing amount of p-f-PEAI (Figure 5.4(g)). Compared with the undoped perovskite film, the intensity of the PbI_2 (001) peak (located at $2\theta = 12.6^o$) decreases strongly with increasing the amount of p-f PEAI. For the perovskite film with x= 0.02 and x= 0.04 the PbI_2 phase is still existing.

For the films with a ratio of x= 0.04 and 0.08, scattering peaks of the 2D perovskite phase (number sign) and two related uncertain intermediate phases (sigma and delta) are found in the literature. Figure 5.4 (h) shows the crystal orientation modification by adding p-f-PEAI. In contrast to the rather random edge-on orientation distribution for x= 0.00, the crystal tends to preferentially align in the plane when p-f-PEAI is added. I note that sketched unit cells in Figure 5.4(h) just schematically depict the crystal orientation rather than the true crystal grain sizes.

5.5 Charge Carrier Dynamics

An understanding of what governs charge-carrier recombination is highly crucial as recombination competes with an efficient charge collection in solar cells. In order to study the charge carrier dynamics of different p-f-PEAI concentrations used for doping the perovskite films, I perform TRPL measurements for perovskite films on glass substrates. The results are shown in Figure 5.5.

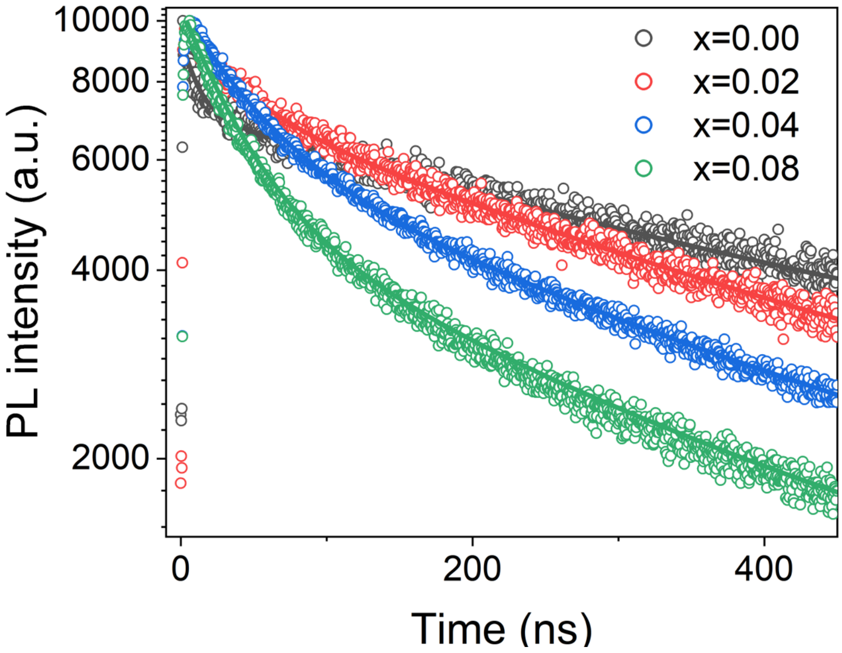

Figure 5.5: Time-resolved PL probed at 763, 773, 787, 777 nm for perovskite films with p-f-PEAI concentrations of x= 0.00 (black), 0.02 (red), 0.04 (blue), 0.08 (green), respectively and corresponding fits based on a two-phase exponential decay (lines). Reprinted with permission from [57]. Copyright 2019, IOP Publishing.

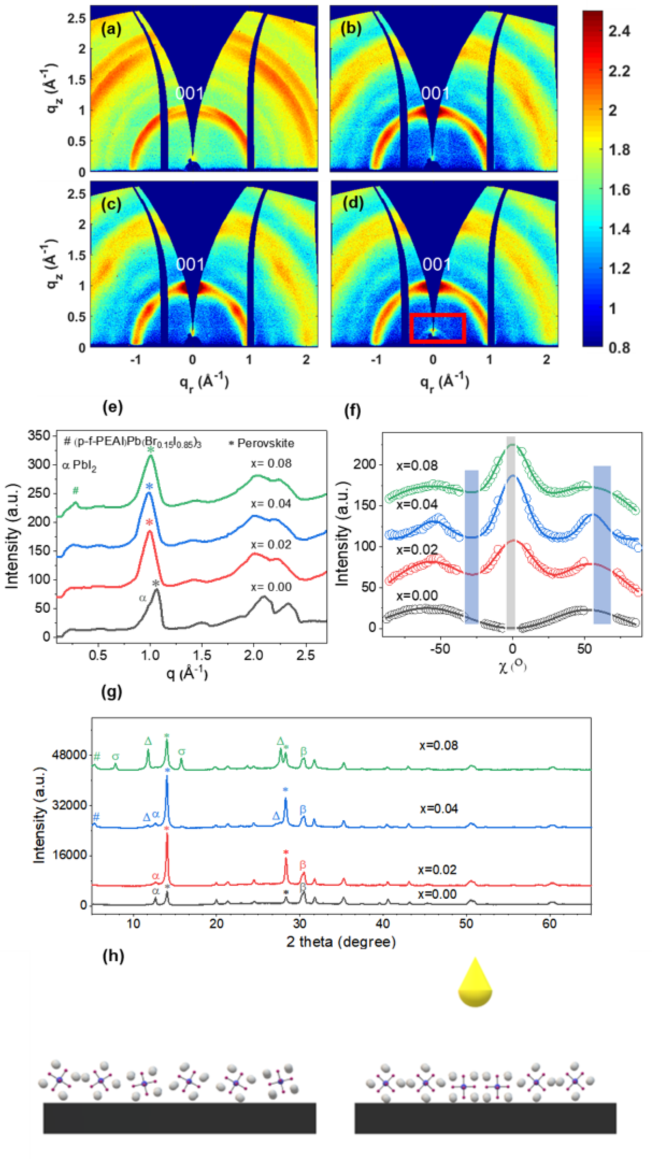

Figure 5.4: 2D GIWAXS data of the perovskite films with different p-f-PEAI concentrations of x = 0.00 (a), 0.02 (b), 0.04 (c), 0.08 (d). (e) Azimuthal integrals from the 2D GIWAXS data for different p-f-PEAI concentrations x. Characteristic Bragg peaks of the 3D-perovskite (star), PbI_2 (alpha) and of $(p-f-PEAI)_2Pb(I_{0.85}Br_{0.15})_4$ (number sign) are highlighted. (f) Tube cuts of the (001) perovskite Bragg peak from the 2D GIWAXS data (symbols) and corresponding fits with Gaussian functions (solid line) for different p-f-PEAI concentrations x. Blue columns mark detector gaps and the grey column is the missing wedge. (g) XRD data of the perovskite films with different p-f-PEAI concentrations. Characteristic Bragg peaks of the $(p-f-PEAI)_2Pb(I_{0.85}Br_{0.15})_4$ (number sign), intermediate phases (sigma and delta), PbI_2 (alpha), 3D perovskite (star) and ITO (beta) are highlighted. (h) Schematic diagram depicting the orientation of the perovskite phase in the reference film (x = 0.00) and in the films with added p-f-PEAI. Reprinted with permission from [57]. Copyright 2019, IOP Publishing.

In general, there are three underlying recombination mechanisms in perovskite materials, which are radiative recombination, Shockley-Read-Hall recombination, Auger recombination and surface recombination [94]. A range of different recombination mechanisms is expressed via

$$\frac{dn}{dt} = -k_1 n - k_2 n^2 - k_3 n^3 \tag{5.1}$$

where n is the charge-carrier density, k_1 is typically related to monomolecular recombination, k_2 is related to bimolecular recombination, and k_3 is the Auger recombination constant [95, 96]. I use a two-phase exponential decay function with a time offset (t_0 is fixed at the highest intensity point, y_0 is the offset of data) which has been used before for previous publications to fit time-resolved PL data [97].

$$y = y_0 + A_1 e^{\frac{-(t-t_0)}{\tau_1}} + A_2 e^{\frac{-(t-t_0)}{\tau_2}} \tag{5.2}$$

The results are summarized in Table 5.1. I attribute the recombination mechanism of the fast decay component (τ_1) to a fast energy transport (such as a charge carrier quench), while the slower decay component could be related to radiative recombination (τ_2) [98,99]. Comparing the pristine perovskite film with the p-f-PEAI doped perovskite film, I can deduce from an increased τ_1 that p-f-PEAI could decrease the charge carrier quenching effect significantly. A quench-reduced bulk layer can contribute to more photocurrent in the potential device. However, as a side effect, the insulating nature of p-f-PEAI and the p-f-PEAI related perovskite phases increase the number of non-radiative recombination centers in the perovskite layer, as seen from a decreased value of τ_2. Thus, I observe a trade-off process with adding different concentrations of p-f-PEAI into the perovskite solution. In the overall weighting metric, the x= 0.02 sample exhibits apparently improved carrier dynamics, which is in good agreement with the corresponding device performance as seen in Figure 5.6(f).

5.6 Performance

To probe the impact of different p-f-PEAI concentrations on the performance of PSCs, I fabricate devices with a functional stack as ITO/SnO_2/perovskite/Spiro-OMeTAD/Au. Figure 5.6 (a)-(d) illustrates an enhancement of the distribution of the PCE for PSCs after adding p-f-PEAI with the concentration of x= 0.02. The improvement results mainly from

Table 5.1: Parameters from fits to the time resolved PL data of doped perovskite films using a two-phase exponential decay (equation 5.2).

Sample	$A_1(\%)$	$\tau_1(\text{ns})$	$A_2(\%)$	τ_2
x=0	24	11.6 ± 0.6	76	503.5 ± 6.4
x=0.02	24.5	40.9 ± 1.4	75.5	408.0 ± 5.3
x=0.04	41.6	53.6 ± 0.6	59.4	391.6 ± 3.7
x=0.08	54.6	41.7 ± 0.4	45.4	301.9 ± 3.0

a short-circuit current increases due to the suppression of the carrier quenching effect, and from a narrowing of the distribution of short-circuit current. Simultaneously, the open-circuit voltage and the fill factor are improved slightly. Due to these reasons, the maximum PCE of 18.4% is achieved for the device with x= 0.02 which has $J_{SC} = 22.25\ mA/cm^2$, $V_{OC} = 1.12$ V, and FF = 74 %. At concentrations of x=0.04 and 0.08, the formation of insulating 2D perovskite phases and related intermediate phases in the PSCs could harm the charge carrier separation process due to their high binding energy compared to pristine 3D perovskite [99]. I minimized the hysteresis behavior of our reference and doped PSCs by using SnO_2 as the electron transport layer (Figure 5.6 (e)). Figure 5.6 (f) illustrates how the J-V curves of the respective champion devices for the different p-f-PEAI concentrations change. Figure 5.6 (g) shows the dark J-V curves of PSCs with different concentrations of p-f-PEAI doping and Table 5.2 provides the device parameters of the solar cells.

Table 5.2: Device parameters of PSCs with different concentrations of p-f-PEAI doping.

Sample	V_{OC}	J_{SC}	**Fill Factor**	**PCE**
x= 0.00	1.10 ± 0.01	21.1 ± 1.9	70.1 ± 2.8	16.5 ± 1.5
x= 0.02	1.11 ± 0.01	22.0 ± 0.4	72.4 ± 1.3	17.7 ± 0.6
x= 0.04	1.13 ± 0.01	22.4 ± 0.5	58.5 ± 1.1	14.8 ± 0.3
x= 0.08	0.92 ± 0.16	15.8 ± 0.6	40.0 ± 2.2	5.8 ± 1.0

With the above observations, I show that the surface morphology of perovskite films can be modified by adding p-f-PEAI. In addition, a small amount of p-f-PEAI doping can not only slightly improve the light absorption of the perovskite film in terms of the AM 1.5G spectrum, but also can dramatically change the preferred crystal orientation while maintaining the original crystal texture. Moreover, the addition of p-f-PEAI can enhance the texture strength. However, with an increasing amount of p-f-PEAI, the preferential

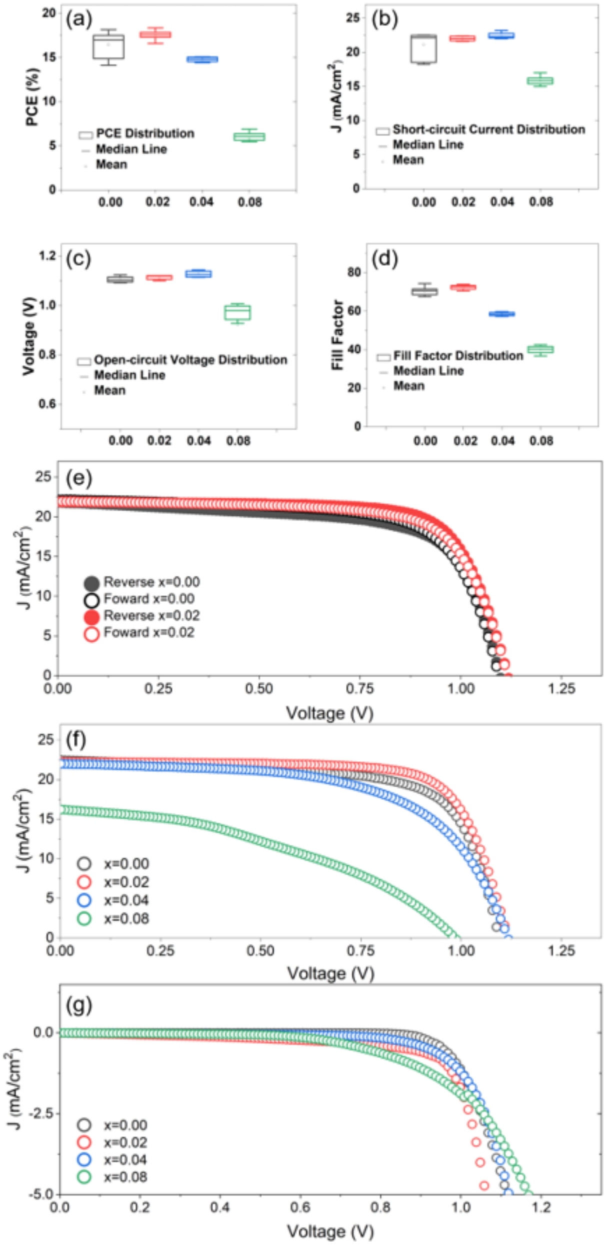

Figure 5.6: (a)-(d) Solar cell parameters from the J-V characterization (a) PCE, (b) Jsc, (c) Voc and FF (d) of PSCs fabricated with different p-f-PEAI concentrations. (e) Hysteresis behavior of PSCs with different concentrations of p-f-PEAI doping (x= 0.00 and 0.02). (f) J-V curves of champion devices and (g) dark J-V curves with different concentrations of p-f-PEAI doping (x= 0.00, 0.02, 0.04, and 0.08). Reprinted with permission from [57]. Copyright 2019, IOP Publishing.

texture seen in the (001) Bragg peak of perovskite films does not change anymore, while the strength of both, edge-on and face-on preferential orientation increases. Hence, I deduce that the forming of new textures is not the main reason for improving the electrical properties. Recently, Zheng et al. proposed that the promotion of a (100) texture strength occurred, restricting the grains' tilt during growth and eventually resulting in a (100)-orientation-dominant film that is of lower defect density than a randomly oriented film [100].

An excess of PbI_2 can enhance the electronic quality of the perovskite film [101,102]. Thus, charge carrier quenching of the perovskite film is suppressed at a concentration x=0.02 due to the passivation effect of doping with p-f-PEAI and PbI_2. The observed improvements regarding light absorption and the carrier quenching is passivated when I continue to increase the ratio of p-f-PEAI to x= 0.04 and x= 0.08, but $(p-f-PEAI)_2Pb(I_{0.85}Br_{0.15})_4$ crystals form, as seen in the XRD data (at 5^o in Figure 5.4 (g)). At the p-f-PEAI concentrations of x= 0.04 and x= 0.08 in the perovskite films, the $(p-f-PEAI)_2Pb(I_{0.85}Br_{0.15})_4$ and relative intermediate phases crystals coexist. The insulating nature of the p-f-PEAI related perovskite phases could be a barrier to the charge separation process in a real device. Thus, the performance of real devices for x= 0.04 and x= 0.08 decreases. In addition, non-radiative recombination increases with increasing the amount of p-f-PEAI and p-f-PEAI related phases. Therefore, the best performance of the device with x=0.02 seems to be a result of the interplay between p-f-PEAI-induced passivation of deep traps, stronger textures, and the presence of excess PbI_2.

5.7 Summary

To conclude, I have revealed that, by adding different concentrations of p-f-PEAI, a new face-on texture of the cubic phase of the perovskite films forms, while the texture strength also is enhanced. TRPL measurements indicate that there is a trade-off process for the p-f-PEAI doping of the perovskite materials regarding the charge carrier dynamics. I speculate that the change of morphology and texture strength, due to the doping with p-f PEAI, seems to suppress the charge carrier quenching effect and be beneficial for charge extraction. Furthermore, by well regulating the p-f-PEAI content, I improve the distribution of the PCE of PSCs without sacrificing the achievable PCE. Therefore, the promotion of texture strength could affect the charge carrier dynamics of perovskite films. Equally importantly, I have shown an important step towards the production of PSCs, which have both, a high and reproducible PCE at the same time. Such developments are necessary on the way to real-world outdoor applications. I believe that this will have an impact on the continuing developments in perovskite-related optoelectronic devices, and pave the road to further understanding structure-dependent material properties and developing theoretical models.

6 Atmosphere Affecting Degradation Mechanisms of Perovskite Solar Cells

This chapter is extracted from the published article: Degradation mechanisms of perovskite solar cells under vacuum and one atmosphere of nitrogen (Guo, Renjun, et al., Nature Energy 6.10 (2021): 977-986., DOI: https://doi.org/10.14459/2021mp1620140). Reproduced from reference [59] with permission from Springer Nature Limited, copyright 2021.

Extensive studies have focused on improving the operational stability of perovskite solar cells, but few have surveyed the fundamental degradation mechanisms. One aspect overlooked in earlier works is the effect of the atmosphere on device performance during operation. Here I investigate the degradation mechanisms of perovskite solar cells operated under vacuum and a nitrogen atmosphere using synchrotron radiation-based operando grazing-incidence X-ray scattering methods. Unlike the observations described in previous reports, I find that light-induced phase segregation, lattice shrinkage and morphology deformation occur under vacuum. Under nitrogen, only lattice shrinkage appears during the operation of solar cells, resulting in better device stability. The different behaviour under nitrogen is attributed to a larger energy barrier for lattice distortion and phase segregation. Finally, I find that the migration of excessive PbI_2 to the interface between the perovskite and the hole transport layer degrades the performance of devices under vacuum or nitrogen.

6.1 Background

Solution-processed hybrid halide perovskite materials have attracted strong interest for next-generation thin-film photovoltaic applications due to their high power conversion efficiency (PCE) and low fabrication costs compared to silicon photovoltaics [103]. Moreover, the possibility of fabrication on flexible substrates opens up promising manufacturing routes and novel application fields are explored, such as light-weight photovoltaic devices for space applications [62]. With solvent engineering, compositional tuning and optoelectronic fine-tuning [86, 104, 105], the highest PCE of perovskite solar cells (PSCs) have reached 25.5 %, which is challenging the highest PCE of monocrystalline silicon solar cells [82]. Although there is such a rapid increase in PCE, challenges remain. More research effort is required to increase the stability of the materials and the longevity of the devices as long-term operational stability remains the main challenge for real-world applications of solution-processed hybrid halide perovskite materials.

Light-induced phase segregation within the perovskite absorber is known to limit the actual long-term operational performance of PSCs. Mahesh et al. revealed that an open-circuit voltage penalty arises from halide segregation [106]. According to Slotcavage and co-workers, phase segregation could be caused by lattice strain, halide migration and crystalline reorganization [107]. In addition, a number of studies indicated that light-induced lattice dynamics had relevance for the structure and consequently the long-term stability of PSCs. Meanwhile, previous studies showed opposing opinions because not all such lattice distortion phenomena were confirmed under operational conditions. For example, Li et al. showed that mixed cations lead iodide PSCs experienced lattice distortion after a long-term light exposure test in nitrogen [74]. Kim et al. reported that photo-induced lattice symmetry ($65mW/cm^{-2}$) for mixed hybrid perovskites ($FA_{0.79}MA_{0.16}Cs_{0.05}Pb(I_{0.83}Br_{0.17})_3$) could suppress the recombination of charge carriers [108]. Tsai et al. observed that light-induced lattice expansion relaxed lattice strain and decreased energetic barriers at the interfaces in vacuum, thus improving the PCE of solar cells compared with the initial performance [109]. However, Rolstion and co-workers debated that the lattice expansion for mixed cation lead iodide perovskite was not light-induced but instead heat-induced thermal expansion of lattice under illumination in the nitrogen atmosphere [110]. In contrast, Liu et al. revealed that $CH_3NH_3PbI_3$ ($MAPbI_3$)-based PSCs experienced lattice compression under operational conditions in air [111]. Hutter et al. emphasized that increasing atmospheric pressure via nitrogen could compress the lattice of mixed halide perovskite materials, thereby increasing the activation barrier for phase segregation [112,113]. On the other hand, vacuum could increase the outgassing process and induce stronger ion migration and defect formation [114]. Moreover, one possibility of bringing all these different findings for different photo-induced lattice distortion behaviors in different studies would be that the composition of the perovskite could affect the preferred orientation of crystals and the strain of perovskite film [115].

Although the above studies discussed light-induced lattice behavior systematically, all experiments were executed under different atmospheres and used different perovskite systems. This makes it very difficult to compare the results of these studies in order to achieve a comprehensive understanding of the real nature of light-induced lattice effects from the present literature. It is no doubt that different macroscopic operation conditions (especially for different atmospheres) have an important influence on the microscopic behavior in PSCs [116]. To this end, Khenkin and co-workers proposed experimental procedures based on the International Summit on Organic Photovoltaic Stability (ISOS) protocols [56]. Although the ISOS protocol suggests using inert atmospheres like vacuum or nitrogen as the standard, the effects of those two atmospheres, vacuum or nitrogen, on the morphology and optoelectronic properties of PSC devices have not been investigated in detail yet. To direct scientific progress toward real-world applications, the microscopic and macroscopic behavior of PSCs needs to be fully understood in vacuum and nitrogen atmosphere.

In the present study, I report that operating mixed cation lead mixed halide perovskite solar cells $(MAPbBr_3)_{0.13}(FAPbI_3)_{0.87}$ under a standard one-sun illumination (AM 1.5G) can cause significant lattice compression and phase segregation in vacuum. The intrinsic different textures of perovskite alloy could offer a pathway for phase segregation. Meanwhile, phase segregation introduces the coherent phase boundary to decrease the film strain. Continuous operation in nitrogen atmosphere only has a minor effect on the lattice dynamics. Theoretical calculations reveal that the thermodynamic driving force for phase segregation is an automatic process in vacuum under operation because of negative activation energy. However, the activation energy is atmosphere-dependent, which can suppress the lattice compression and phase segregation by the application of an atmosphere like nitrogen. Grazing-incidence small-angle X-ray scattering (GISAXS) reveals that small-sized crystallites are formed under operation in vacuum, while the crystal size distribution is stable under operation in nitrogen atmosphere. I observe that devices degrade to different extents under these two exemplary conditions, thereby highlighting the importance of the used experimental protocol. Phase segregation happens under the operation in vacuum. It leads to the formation of the low bandgap minority phase, resulting in a minor decrease of V_{OC}. Using X-ray photoelectron spectroscopy (XPS) and drift-diffusion device modelling, I find that bias-induced migration of excess lead iodide into interfaces between the perovskite and the hole-transporting layer contributes to a voltage penalty in both atmospheres. In vacuum, the broken crystals serve as pinholes for the perovskite layer, introducing shunting pathways into the device, and decreasing fill factor and open-circuit voltage (V_{OC}) at the same time.

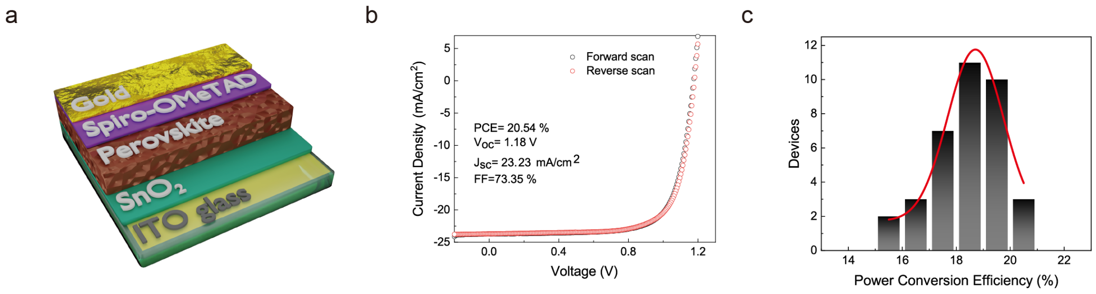

Figure 6.1: (a) Sketch of the device architecture of fabricated planar MAFA perovskite solar cells. (b) J-V scan of the champion device for MAFA perovskite solar cells and related device parameters. (c) Histogram of PCE obtained from 36 fabricated MAFA PSCs with red line displaying a Gaussian fit. Reprinted with permission from [59]. Copyright 2021, Nature energy.

6.2 Structure and Performance of the Devices Analysed

I fabricate planar MAFA PSCs via the anti-solvent method, as previously reported [90]. Fig. 1a presents the device architecture of the studied PSCs. The PCE of the champion device equals the certified record of MAFA perovskite solar cells (Fig. 6.1b) [87]. Fig. 6.1c shows the related histogram of the PCE data for 36 devices. The narrow steady-state photoluminescence spectrum and the sharp edge in the absorbance spectrum for MAFA perovskite films suggest uniformity and phase purity (Fig. 6.2a). Top view scanning electron microscopy (SEM) and cross-section SEM images show smooth perovskite films, indicating the formation of condensed grains without pin-holes (Fig. 6.3 b and c). X-ray diffraction data (Fig. 6.3a and b) show Bragg reflexes from $delta - FAPbI_3$ and PbI_2 phases. The existence of these phases in perovskite films was reported to boost the PCE of perovskite solar cells [87, 90]; however, an excessive amount of PbI_2 leads to a poor device performance [117]. These material properties and device efficiencies are of critical importance for this state-of-the-art research about degradation.

6.3 Structural Changes during Operation of the Devices

Through the operando grazing-incidence wide-angle X-ray scattering (GIWAXS) studies on the MAFA PSCs via the ISOS-L-1I protocol (with continuous voltage-bias scan and illumination in inert atmospheres), I find lattice shrinkages in different extents under different atmospheres. Pictures of the operando set-up are shown in Fig. 6.4 and Fig. 6.6d. The detailed experimental conditions and data treatment are listed in the Methods section. The scattering depth for the MAFA perovskite is 660 nm at the used incident angle of 0.4^o, which ensures that I measure the statistical bulk information of the PSCs

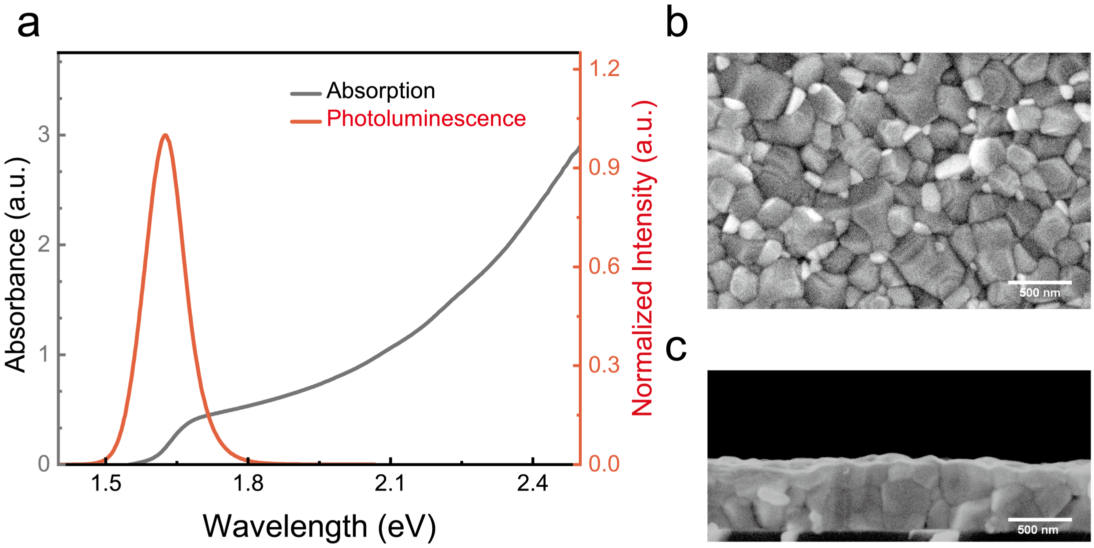

Figure 6.2: Photoluminescence and absorption spectra, SEM images of MAFA perovskite films. (a) The light absorption spectrum for MAFA perovskite films fabricated on ITO substrates (black line) and the normalized photoluminescence spectrum of MAFA perovskite films fabricated on glass substrates (red line). (b) SEM top view image showing the surface morphology. (c) SEM cross-section image giving a side view of the perovskite film morphology. Reprinted with permission from [59]. Copyright 2021, Nature energy.

(Fig. 6.5).

Under vacuum, the time evolution of 2D GIWAXS data demonstrates a significant lattice shrinkage and phase segregation into the minority phase $FAPbI_3$ and the majority phase $(MAPbBr_3)_{0.17+x}(FAPbI_3)_{0.83-x}$ during the operation of the PSCs (Fig. 6.6a and c). The (100) Bragg peak position of the MAFA perovskite experiences a dramatic shift after 45 min of illumination (increasing from 0.998 $Å^{-1}$ to 1.018 $Å^{-1}$), proving a dramatic decrease of the interplane spacing of the crystal. This initial shift of the (100) Bragg peak position is followed by a slight back shift (decreasing from 1.018 $Å^{-1}$ to 1.010 $Å^{-1}$), coinciding with the phase segregation as seen in the (210) Bragg peak. In contrast, the time evolution of the line profiles, azimuthally integrated from the 2D GIWAXS scattering data, indicates that the MAFA perovskite undergoes only a slight lattice shrinkage in nitrogen (Fig. 6.6b).

Since different Bragg peaks reflect different lattice spacings in the materials, I assign the Bragg peak (hkl) of the cubic structure with the following equation:

$$d_{hkl} = a\sqrt{h^2 + k^2 + l^2} \tag{6.1}$$

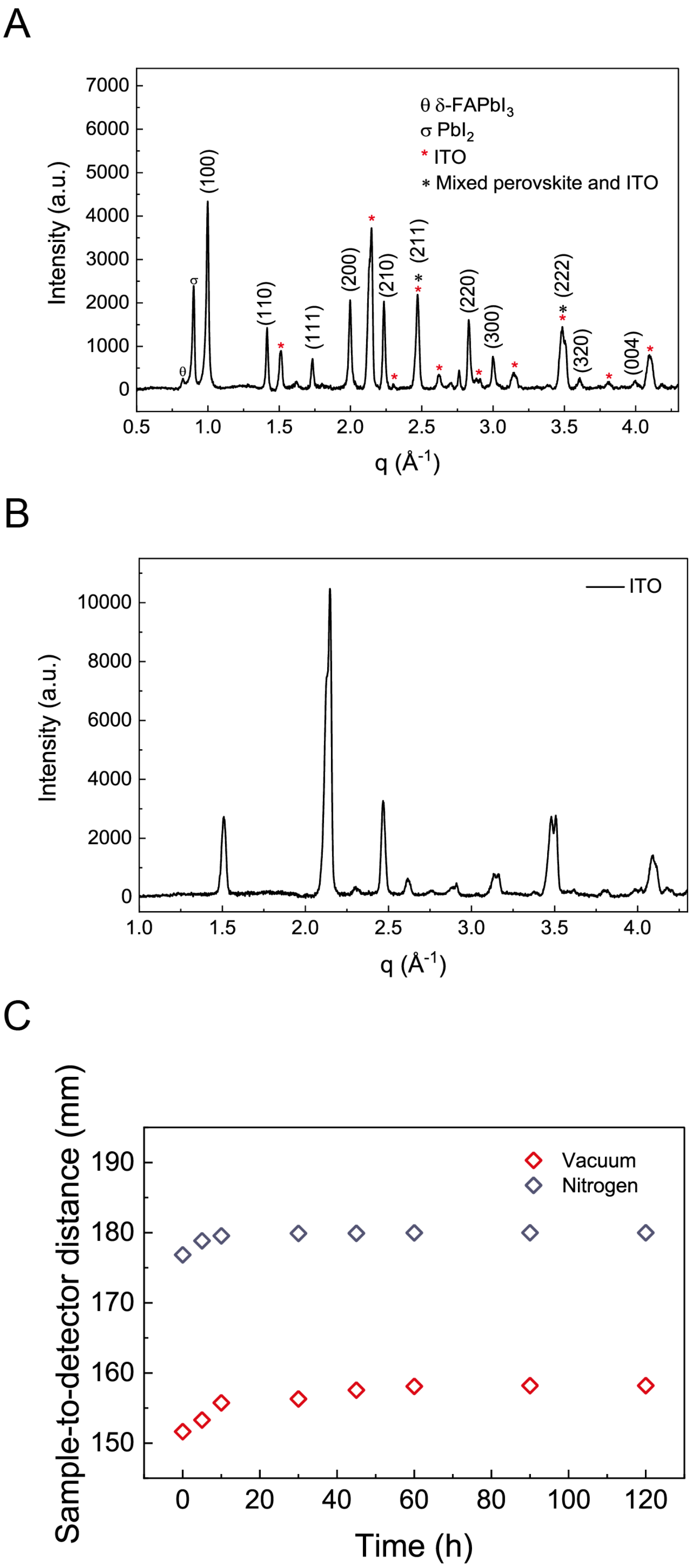

Figure 6.3: X-ray diffraction spectra for the MAFA perovskite film and ITO. (a) XRD data of MAFA perovskite film with index Bragg peak positions. (b) XRD data of ITO substrates. (c) Sample-to-detector distance calibration via the ITO peak position for measurements in vacuum (red) and nitrogen (blue). Reprinted with permission from [59]. Copyright 2021, Nature energy.

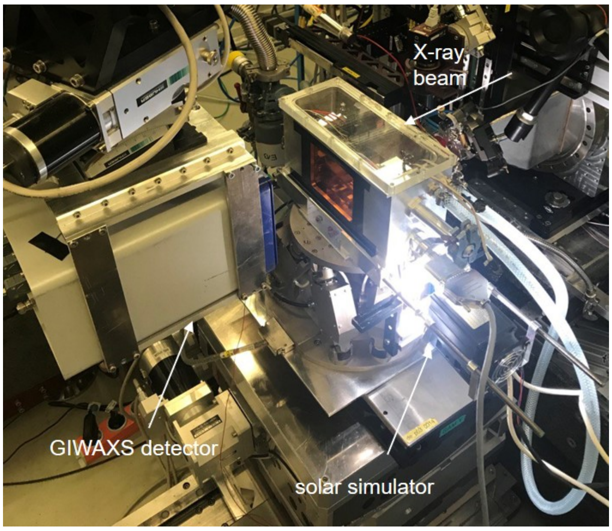

Figure 6.4: Synchrotron radiation-based operando set-up. Photograph of the operando set-up used in the experiments at DESY beamline P03 with characteristic components indicated. The X-ray beam position is as close as possible to the metal electrodes ($< 1\ \mu$m) or on top of the metal electrodes as indicated in the text. Reprinted with permission from [59]. Copyright 2021, Nature energy.

where refers to the lattice parameters, interplane spacing, and Miller indices, respectively. According to the cubic model, the degree of lattice shrinkage extracted from the (110) and (111) Bragg peaks is different compared to the measured data of the (100) Bragg peak for the whole illumination period (Fig. 6.6d and Fig. 6.7a and b). Therefore, the lattice shrinkage of the MAFA perovskite is non-uniform under the operation in both atmospheres because lattice constants are different in different lattice planes. In addition, Fig. 6.7c shows that the emergence of Bragg peaks around 1.6 $\AA^{-1}$ indicates the forma-

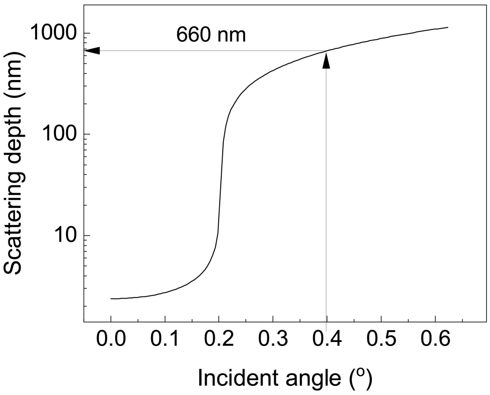

Figure 6.5: Penetration depth of the X-ray beam as a function of the incident angle. At the used incident angle, the scattering depth is 660 nm. Reprinted with permission from [59]. Copyright 2021, Nature energy.

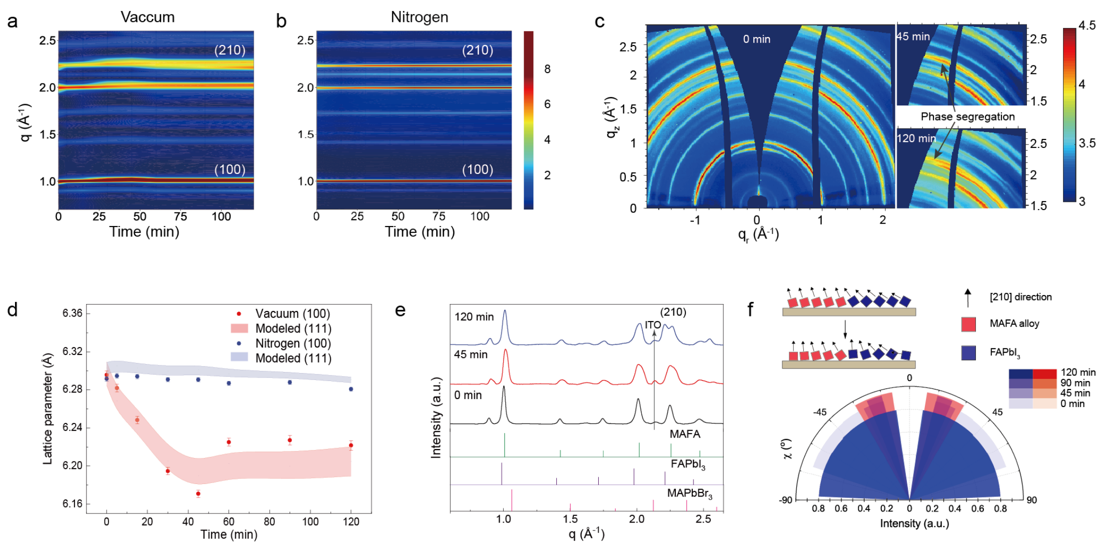

Figure 6.6: Structure evolution of MAFA PSCs operating in different atmospheres. (a,b) Time-evolution of operando synchrotron radiation-based GIWAXS data plotted as azimuthally integrated line profiles of 2D GIWAXS data for the operation of MAFA PSCs under vacuum (a) and nitrogen (b) based on the ISOS-L-1I protocol. (c) Temporal evolution of 2D GIWAXS data transferred to q-space and collected under vacuum during the operation of the solar cell for 0, 45 and 120 minutes. (d) Lattice evolution for different atmospheres (vacuum in red, nitrogen in blue) as a function of illumination time. Filled circles denote the measurements with error bars derived from three-times fit through the Gaussian distribution of the (100) Bragg peak. The shaded areas display the modeled (111) peaks, reflecting a non-uniform shrinkage for all lattice directions. (e) Evolution of radial GIWAXS profiles integrated over all azimuthal angles (pseudo-XRD profiles) during operation for MAFA PSCs in vacuum, and simulated MAFA, $FAPbI_3$, and $MAPbBr_3$ perovskite XRD scattering patterns. (f) Crystallite orientation evolution during operation for MAFA perovskite under vacuum (stronger colour patterns indicate the orientation of crystals after longer operation times) reconstructed from the tube cuts of the 2D GIWAXS data at the (210) Bragg peak. The schematic diagram shows the evolution of the crystallite orientation. Reprinted with permission from [59]. Copyright 2021, Nature energy.

tion of the tetragonal perovskite phase caused by a non-uniform lattice shrinkage, which was also found by a previous study due to a composition change [118].

I further use the Williamson-Hall analysis for azimuthally integrated line profiles to track the film strain evolution under both atmospheres (Fig. 6.8). During the operation of PSCs under vacuum, the strain of the MAFA perovskite layer increases first, then decreases slightly after the phase segregation into a minor phase $FAPbI_3$, and a major phase $(MAPbBr_3)_{0.17+x}(FAPbI_3)_{0.83-x}$ appears. In contrast, the film strain releases slightly under operation in a nitrogen atmosphere, and is below the film strain found in vacuum. In

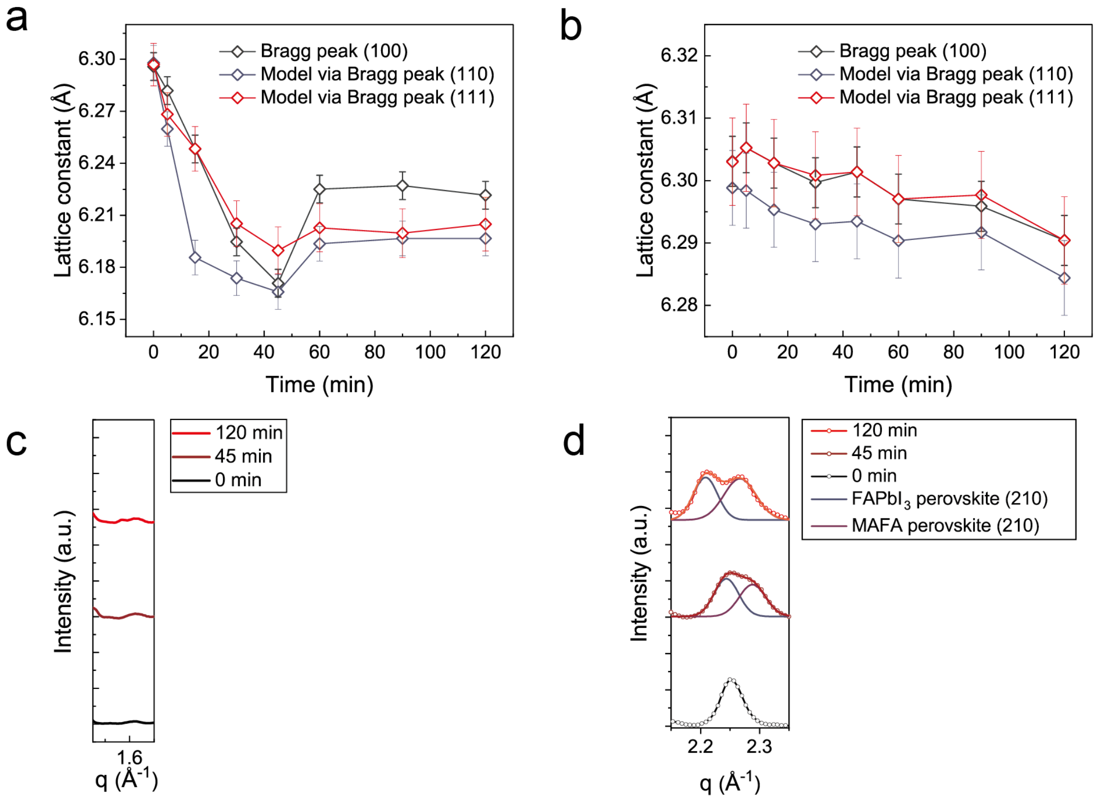

Figure 6.7: Lattice evolution for different atmospheres as a function of operation time. (a) Vacuum, (b) nitrogen. The deviations of the cubic model reflect non-uniform lattice compression. (c) Confirmation of a non-uniform compression deduced from the signal of the tetragonal phase shown at a q range of 1.5-1.7 $\AA^{-1}$. (d) Detailed fits for the evolution of the (210) Bragg peak under vacuum conditions to extract values of and for the misfit calculation of the phase boundary. At 120 min, is 2.536 $\AA^{-1}$ and is 2.458 $\AA^{-1}$. Reprinted with permission from [59]. Copyright 2021, Nature energy.

addition, the (210) Bragg peak of MAFA splits up with the increase of the operation time under vacuum, indicating a phase segregation and the formation of the new components MAFA and $FAPbI_3$ as a result of the 45-min operation under vacuum (Fig. 6.6e). The release of the film strain happens with phase segregation at the (210) plane, indicating that this plane is the habit plane due to its low film strain. I calculate the misfit of the separated (210) Bragg peaks at 120 min by using the equation:

$$\delta = \frac{2\left(d_{FAPbI_3} - d_{MAFA}\right)}{d_{FAPbI_3} + d_{MAFA}} \tag{6.2}$$

I obtain $\delta = 0.022$ (< 0.05), which is the certification of the formation of a coherent phase boundary [119]. Coherent phase boundaries have lower energy and can enhance the strength and phase stability of the MAFA perovskite layer [120]. Although condensed

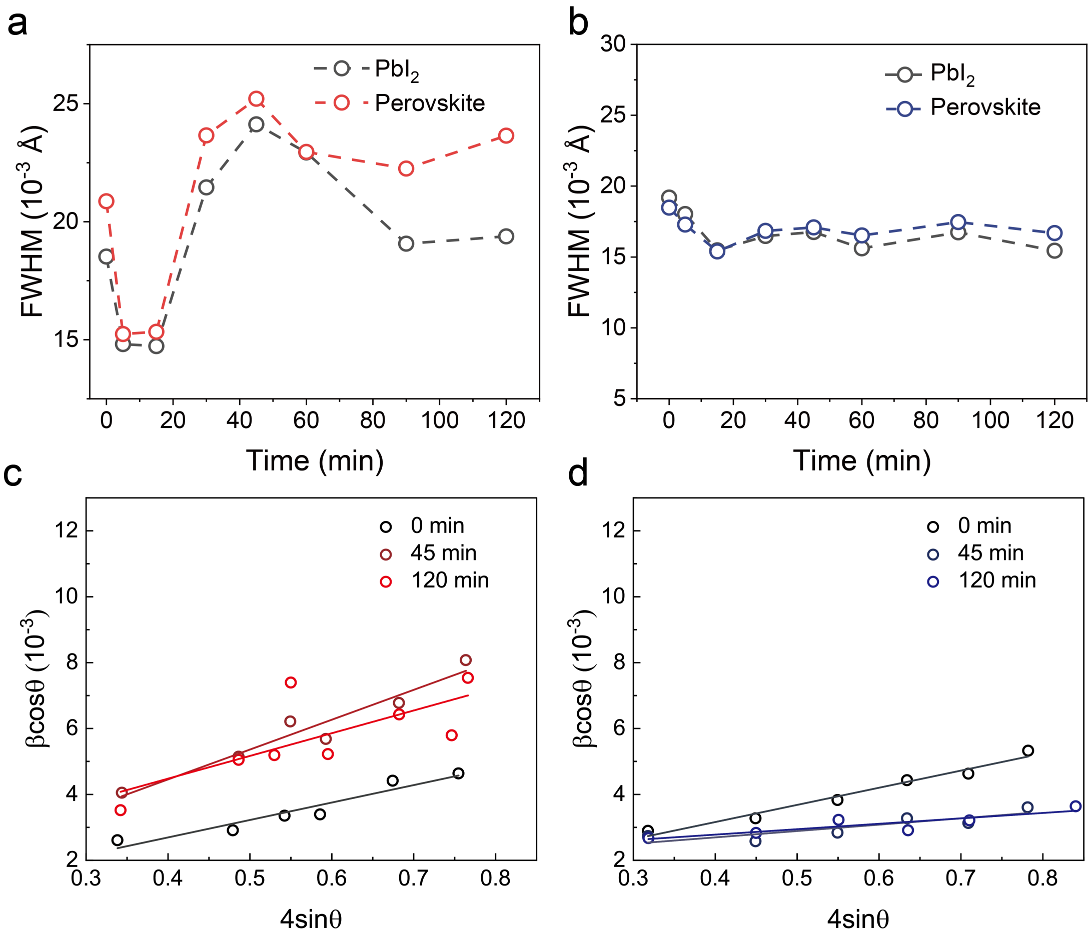

Figure 6.8: Evolution of full width at half maximum for PbI_2, perovskite peaks and strain during operation in different atmospheres for 120 min. (a, c) Vacuum and (b, d) nitrogen. In (c) and (d) linear fits show the strain analysis using Williamson-Hall plots, and the slope of fitted lines reflects the full width at half maximum, the Bragg angle and the strain. Reprinted with permission from [59]. Copyright 2021, Nature energy.

grains are observed by SEM imaging, a local crystal misorientation may exist and produce a local structural strain. Thus, potential phase segregation would be driven by such local crystal misorientations [121]. Such a scenario is also confirmed by Fig. 6.9a, which shows that $FAPbI_3$ crystallite orientations already exists before the phase segregation. This finding indicates that the crystallite orientations of MAFA perovskite films occur already during the fabrication process, which will drive the phase segregation under operation. The broadening of the crystallite orientations seen in Fig. 6.6f and Fig. 6.9 a-e with increasing operation time indicates that the orientations of both, the MAFA and $FAPbI_3$ become more disordered after continuous operation.

The results from measurements on top of the gold top contact also confirm that the struc-

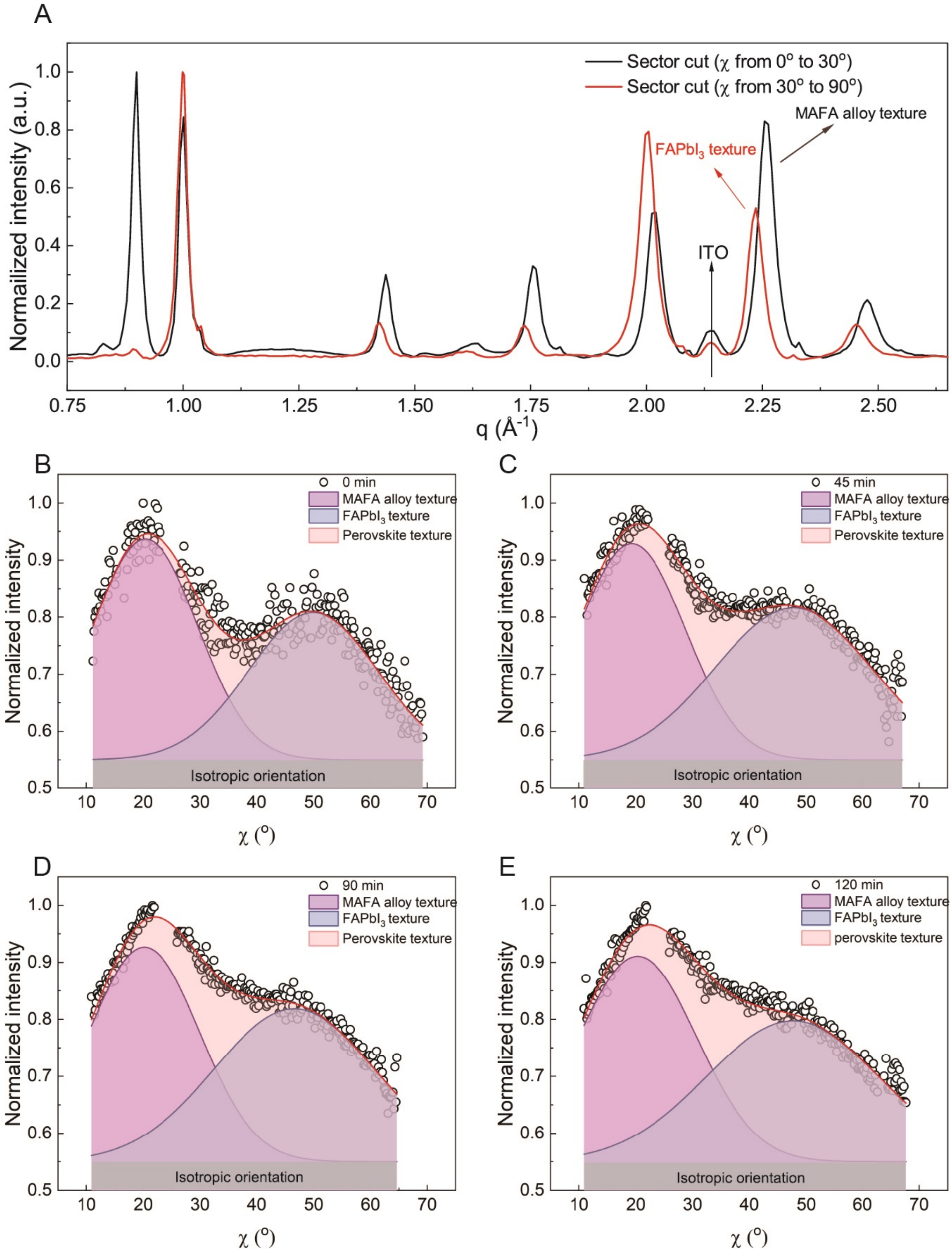

Figure 6.9: Texture analysis based on different integration methods during the operation under vacuum. (a) Line-cuts obtained from the 2D GIWAXS data using different sector cuts during operation in vacuum at 0 min. Evolution of different perovskite textures extracted from the (210) Bragg peak during the operation in vacuum as a function of time after (b) 0 min, (c) 45 min, (d) 90 min and (e) 120 min. Reprinted with permission from [59]. Copyright 2021, Nature energy.

tural evolution is not affected whether the monitoring positions are on the electrode or just beside the electrode (Fig. 6.10a, b, c and f). When PSCs operate under the ISOS-L-2I protocol with an increased temperature (55 °C) in nitrogen, the perovskite lattice shows a slightly stronger lattice shrinkage tendency (Fig. 6.10d and g). The Fig. 6.10e and h confirm that PbI_2 and δ-$FAPbI_3$ phases are less likely to affect the lattice distortion because PSCs with the pure-phase component $Cs_{0.1}FA_{0.9}PbI_3$ also experience a lattice shrinkage under operational conditions (ISOS-L-1I). According to the above observations, I claim that the mixed cation lead mixed halide perovskites experience lattice shrinkages and phase segregation during the operation of the PSCs under vacuum. A nitrogen atmosphere with a standard atmospheric pressure serves as one useful condition to minimize the effects of lattice shrinkages and phase segregation during the operation of the PSCs.

6.4 Morphology Changes under the Operation of Devices

I use grazing-incidence small-angle X-ray scattering (GISAXS) to investigate the morphology evolution of PSCs under operation in different atmospheres (Fig. 6.11a and d). To quantify our results from the 2D GISAXS data, I survey the temporal evolution of the intensities in the horizontal line cuts and model these data with form and structure factors (Fig. 6.12). The superposition of Gaussian distributed form factors used for modelling the GISAXS data relates to the crystal size distribution because the intensity scales linearly with the number of crystals of a specific size Fig. 6.11b and c shows that the number of small crystals increases during operation under vacuum. Our results show that crystals with diameters lower than 40 nm break into smaller crystals. These small crystals act as pinholes in the PSCs [122]. The increasing number of crystals also introduces an increasing number of grain boundaries. This phenomenon is known as grain boundary strengthening, which can, in turn, increase the strength of the MAFA perovskite film under operation in vacuum [123]. It can stop a further degradation of the MAFA perovskite film. In contrast, I do not observe a similar phenomenon in nitrogen (Fig. 6.11e).

Eperon et al. showed the existence of porosity in the perovskite film using a gas pycnometer, and this porosity could offer a physical pathway for the origin of the nitrogen adsorption process. To confirm this, I measure the adsorption behavior of the MAFA perovskite material in nitrogen via the Brunauer-Emmett-Teller method (Fig. 6.13). Indeed, the MAFA perovskite can adsorb more nitrogen as the pressure of nitrogen increases. The perovskite sample exhibits a type III isotherm, which indicates the formation of a nitrogen molecule multilayer around the perovskite layer during the operation of PSCs under

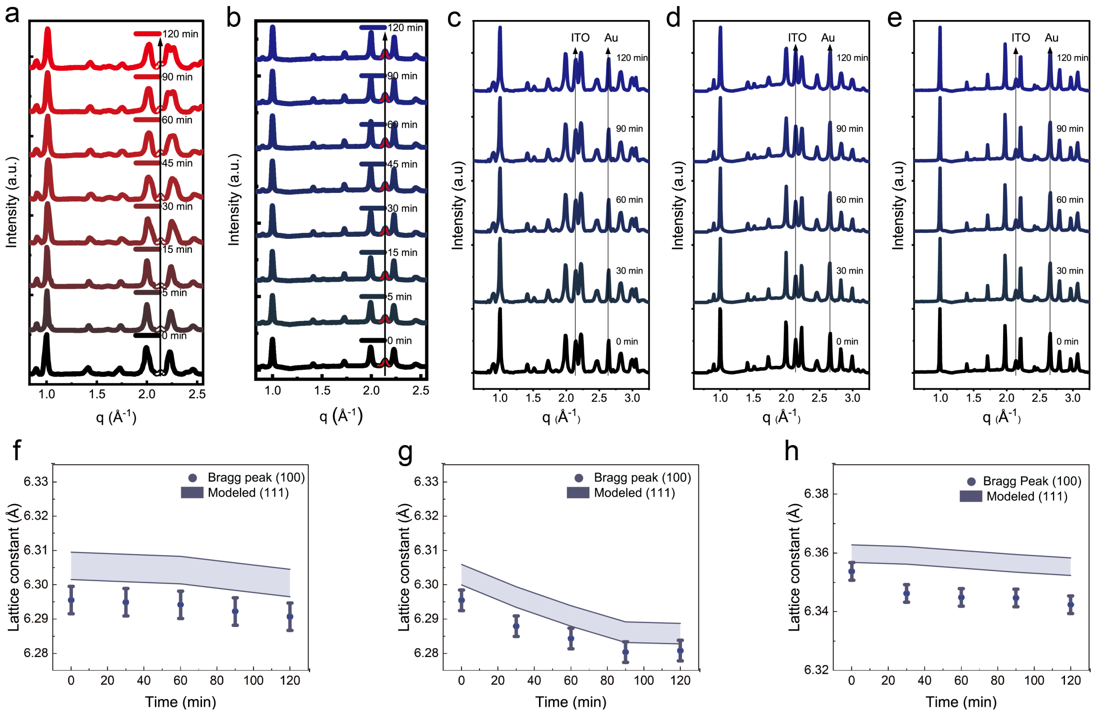

Figure 6.10: Evolution of in situ GIWAXS diffraction cake cuts for different perovskite components of PSCs during operation in different atmospheres for 120 min. (a-e) Temporal evolution of in situ GIWAXS diffraction cake cuts measured for PSCs with the components (a) MAFA under operation in vacuum using the protocol ISOS-L-1I, (b) MAFA under operation in nitrogen using the protocol ISOS-L-1I, (c) MAFA at the position of the gold top contact under operation in nitrogen using the protocol ISOS-L-1I, (d) MAFA at the position of the gold top contact under operation in nitrogen using the protocol ISOS-L-2I (with 55 °C) and (e) $Cs_{0.1}FA_{0.9}PbI_3$ at the position of the gold top contact under operation in nitrogen using the protocol ISOS-L-1I. The arrows indicate the Bragg peak position of ITO. (f-h) Extracted lattice evolution for the (100) Bragg peak (symbols) and the modelled (111) peak (band) in case of measurements on the top gold contacts for (f) MAFA based solar cells in nitrogen using the protocol ISOS-L-1I, (g) MAFA based solar cells in nitrogen using the protocol ISOS-L-2I (with 55 °C) as a function of illumination time. (h) $Cs_{0.1}FA_{0.9}PbI_3$ based solar cells in nitrogen using the protocol ISOS-L-1I as a function of illumination time. The shaded areas display the modelled (111) peaks, reflecting a non-uniform shrinkage for all lattice directions. Reprinted with permission from [59]. Copyright 2021, Nature energy.

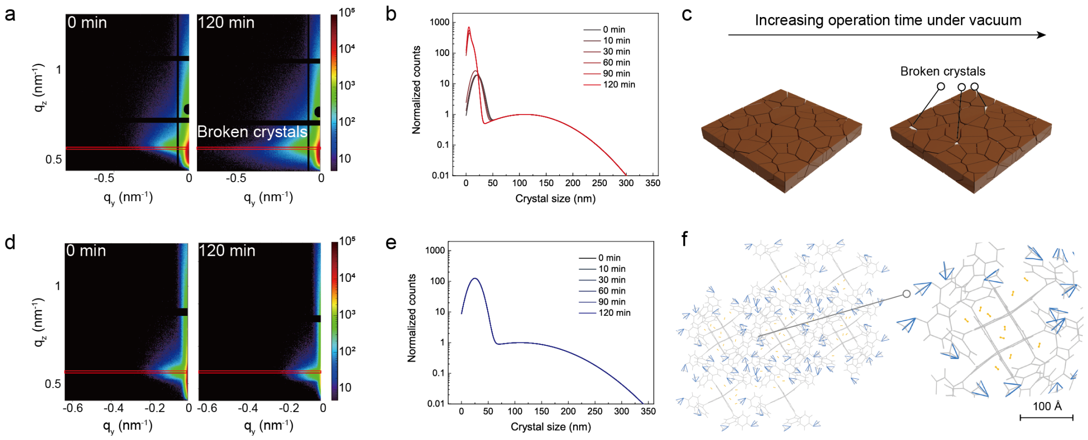

Figure 6.11: Morphology evolution of MAFA PSCs operating in different atmospheres. (a) Time evolution of 2D GISAXS data under operation in vacuum (red line indicates the horizontal line cut at the perovskite Yoneda peak position). (b) Evolution of crystal size distributions under operation in vacuum for different form factors extracted from the model and intensity-normalized to form factor 1 (110 nm). (c) Scheme to illustrate the improved strength of the perovskite film to suppress further deformation through the increase of grain boundaries due to broken crystals. (d) Time evolution of 2D GISAXS data under operation in a nitrogen atmosphere (red line indicates the horizontal cut at the perovskite Yoneda peak position). (e) Evolution of crystal size distributions under operation in a nitrogen atmosphere for different form factors extracted from the model and normalized to form factor 1 (110 nm). (f) Schematic diagram of nitrogen molecules (yellow symbols) diffusing through the spiro-OMeTAD layer expressed by a blue (side chains) and grey (intermolecular π-π stackings) mixed space frame during the operation of solar cells under nitrogen. The zoomed inset indicates the loose structures of the spiro-OMeTAD allowing the diffusion of nitrogen molecules. Reprinted with permission from [59]. Copyright 2021, Nature energy.

nitrogen [124]. For the PSCs used in this study, most of their module area is not covered by electrodes, which means that the majority of spiro-OMeTAD layer can directly contact the atmosphere. The loose space structure of spiro-OMeTAD offers pathways, which allow for the diffusion of nitrogen molecules into the active layer underneath (Fig. 6.11f). Hence, I suggest that a nitrogen atmosphere under standard pressure helps to stabilize the morphology of the perovskite film during operation. Meanwhile, I highlight the importance of large crystals for enhancing the stability of perovskite materials.

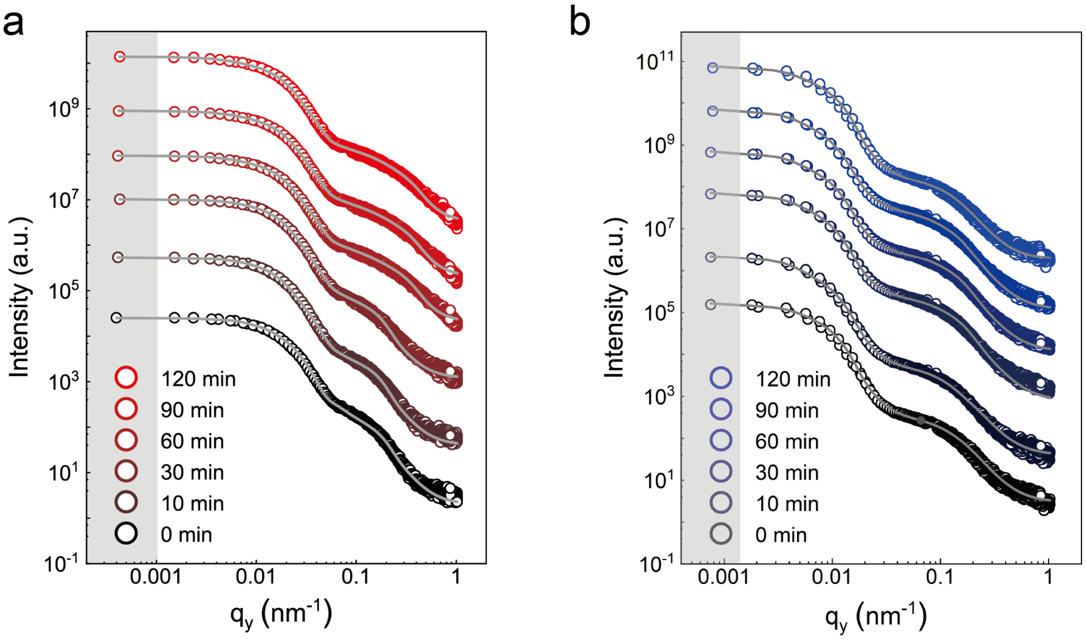

Figure 6.12: Horizontal line cuts of the 2D GISAXS data. Measurements (symbols) are shown together with fits (lines) for different operation times in (a) vacuum and (b) nitrogen. Reprinted with permission from [59]. Copyright 2021, Nature energy.

6.5 Mechanisms of Atmosphere-dependent Operational Stability

To investigate the intrinsic driving force for phase segregation and lattice shrinkage, I combine the aforementioned structure and morphology evolution with thermodynamic kinetics to provide an interpretation. For the calculations, I focus on the

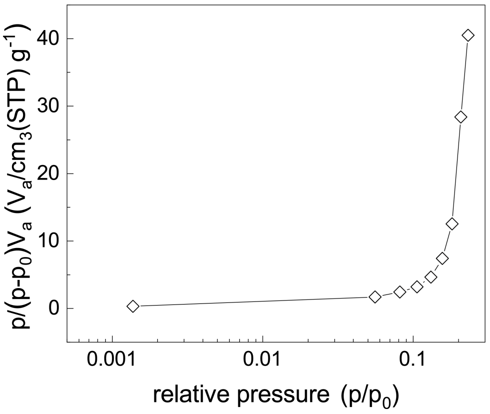

Figure 6.13: Nitrogen gas isotherm. The measurement of the perovskite material is shown on a log scale. Reprinted with permission from [59]. Copyright 2021, Nature energy.

$(MAPbBr_3)_{0.2}(FAPbI_3)_{0.8}$ component. I first use the Gibbs free energy to evaluate the effect of pressure on the free energies of perovskite components, in contrast to a previous report, which applied a GPa-level pressure to suppress the phase segregation of mixed halide perovskites under illumination [112]. Atmospheric pressure can only decrease the Gibbs free energy by 1.29×10^{-7} eV due to the use of relatively low pressure (1.01×10^5 Pa) in our study. Hence, in our study, the increased pressure from the nitrogen atmosphere largely does not affect the free energy and cannot be the reason for the suppression of phase segregation. Thus, I use Helmholtz free energy to calculate the free energy of the mixing perovskite phases below. Previous studies have efficiently proven that the lattice shrinkage can increase the activation energy barrier to suppress phase segregation due to the decrease of ion migrations. However, perovskite films under illumination in vacuum can increase the doping concentration for all hybrid perovskite materials due to the decomposition induced by volatile species or the gas desorption induced defects in the crystal structures [125]. Simultaneously, the relative permittivity of perovskite materials can change when illumination or pressure are applied [126, 127]. Thus, I recalculate the activation energy of the phase segregation under operation conditions in different atmospheres by means of the method used in references to show the potential for phase segregation [113].

I find negative activation energies of the MAFA perovskite under operation in vacuum, indicating that the phase segregation could occur spontaneously at room temperature (Fig. 6.14a). In contrast, positive activation energy in the case of operation in nitrogen indicates a much larger energy barrier for phase segregation, significantly preventing phase segregation. Fig. 6.14b shows that perovskites with different components display different thermodynamic phase stabilities. When the free energy of the mixing perovskite phase ($\Delta\ F_{mix}$) is larger than 0, phase segregation is energetically favorable for the corresponding secondary phases. Additionally, the phase segregation energy ($\Delta\ F_{sep}$) for different concentrations x for $(MAPbBr_3)_x(FAPbI_3)_{1-x}$ illustrates a concave upward curvature of $\Delta\ F_{mix}$ ranging from x = 0 to x = 0.2, indicating a thermodynamically stable mixed phase at room temperature. The concave downward curvature of $\Delta\ F_{mix}$ from x > 0.2 refers to metastable ($\Delta\ F_{mix} < 0$) and unstable states ($\Delta\ F_{mix} > 0$) for the MAFA perovskite. However, $\Delta\ F_{mix}$ will increase if I take the influence of photo-excited carriers (n = 0-0.26/f.u.) into consideration, and this results in a thermodynamic driving force for the phase segregation of the perovskite film. This observation is also consistent with previous reports, which pointed out that perovskite materials tend to be phase-separated as Br content increases [128, 129].

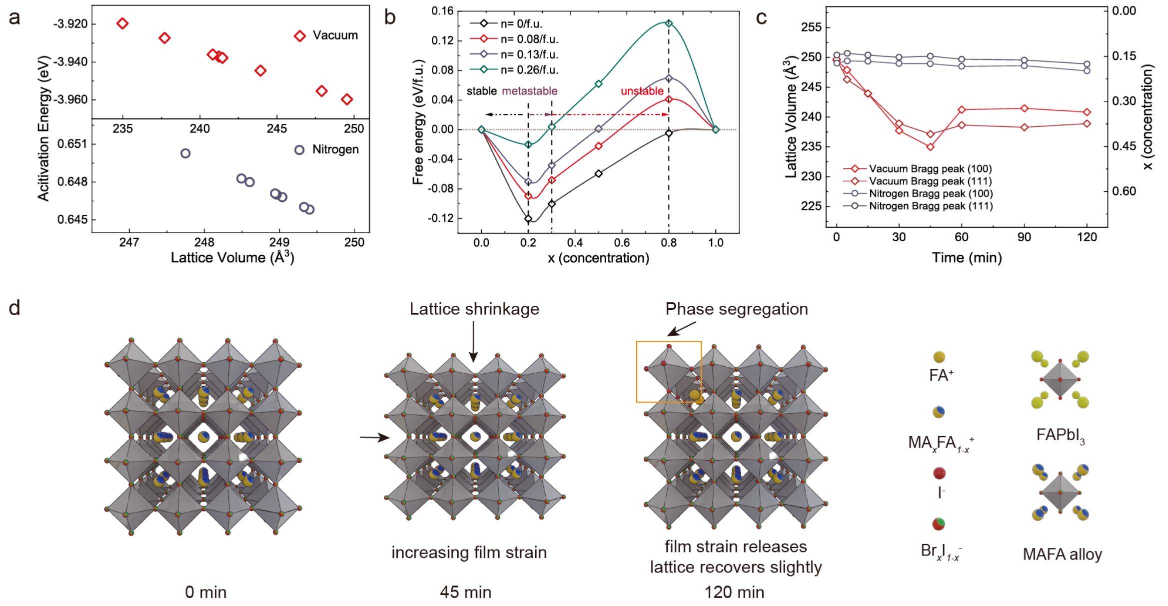

Figure 6.14: The thermodynamic driving force of lattice shrinkage and phase segregation. (a) Evolution of activation energies for phase segregation as a function of lattice volume under vacuum (red) and a nitrogen atmosphere (blue). (b) Density-functional theory calculated Helmholtz free energy of $(MAPbBr_3)_x(FAPbI_3)_{1-x}$ (x= 0, 0.2, 0.3, 0.5, 0.8 and 1) at room temperature (T = 300 K) for different photo-excited charge carrier densities n. The black, purple and red dash lines indicate the stable, metastable and unstable phases for different compositions of the perovskite, respectively. (c) The lattice volume evolution translated to related compositional ratios as a function of the operation time in different atmospheres. (d) Schematic diagram projecting the non-uniform lattice shrinkage during the operation of PSCs in vacuum, followed by the phase segregation of the MAFA perovskite, which is highlighted by an orange frame. Reprinted with permission from [59]. Copyright 2021, Nature energy.

Next, I link the thermodynamic kinetics with the structure and morphology evolution process. Fig. 6.14c shows the lattice volume as a function of the composition ratio of $MAPbBr_3 \ and \ FAPbI_3$. Corresponding changes of MAFA perovskite lattice volumes as a function of operation time in different atmospheres are also taken into consideration. Under vacuum, the operation of PSCs demonstrates a strong lattice shrinkage to suppress the trend of spontaneous phase segregation at room temperature (Fig. 6.14a and Fig. 6.7a). After a 45-min operation in vacuum, the lattice volume reaches about 235 $\AA^3$, which is the expected value for the lattice volume of the component $(MAPbBr_3)_{0.45}(FAPbI_3)_{0.55}$. Hence, the film strain increases dramatically due to such lattice shrinkage. The dramatically compressed lattices perturb the balance between the film strain and the phase stability. The intrinsically different crystallite orientations for the MAFA phase and $FAPbI_3$ offer a starting point for phase segregation. To maintain the metastability of the $(MAPbBr_3)_{0.17}(FAPbI_3)_{0.83}$ PSCs during operation in vacuum, $FAPbI_3$ crystals precipitate from the (210) habit plane, thereby releasing the film strain (Fig. 6.6e and Fig. 6.8c). This process also forms a coherent phase boundary, which could increase the strength of the perovskite film and suppress further phase segregation. Moreover, small size crystals break to maintain the low energy of the whole system and thus introduce a grain-boundary strengthening. Finally, the lattice volume reaches approximately 240 $\AA^3$, which is the expected value for the component $(MAPbBr_3)_{0.28}(FAPbI_3)_{0.72}$. This component has a negative value of free energy even under strong illumination, indicating a metastable mixed perovskite phase state.

I speculate that there are four causes for the observed phase segregation, severe lattice shrinkage, and broken crystals under vacuum, as illustrated in the schemes in Fig. 6.11c and Fig. 6.14d:
1) a significant mismatch between the compressed lattice volume and the real components of the film;
2) intrinsically different crystallite orientations of the MAFA and $FAPbI_3$;
3) the need to decrease the film strain introduced by phase segregation and the formation of the coherent phase boundary;
4) the demand to strengthen the perovskite film to suppress further deformation through the increase of grain boundaries due to broken crystals.

Physical adsorption of gas molecules can decrease the free energy via an exothermic process [130]. Thus, I speculate that the physical adsorption of nitrogen could play an important role in reducing the film strain and maintaining the lattice and phase stability, which is also related to a larger activation energy barrier for phase segregation as discussed above. This observation is similar to the study of Alberti et al., who showed that a nitrogen-assisted process played an important role in the lattice recovery during the annealing process, and that long-term operational stability can be improved by device encapsulation inside a pure nitrogen atmosphere [131].

6.6 Different Degradation Pathways and Relative Performance

I examine the temporal device performance of MAFA PSCs under operation conditions in two different atmospheres. Devices operated in nitrogen show better stability in terms of open-circuit voltage (V_{OC}), fill factor (FF), and PCE, compared with those operating under vacuum. Fig. 6.15a shows a decrease of 20 % for the V_{OC} and 10 % for the FF under vacuum (normalized from 6 devices, Fig. 6.16a and b show the exemplary J-V evolution from one of these devices). In contrast, PSCs show only a 10 % decrease of the V_{OC} in a nitrogen atmosphere (Fig. 6.15b). To identify the mechanisms for these losses, I measure transient absorption (TA) spectra for a MAFA perovskite film within 120 minutes of exposure to a white-light spectrum under vacuum. Fig. 6.15c shows that there is no peak shift for the perovskite film with white light soaking under a high-vacuum condition, indicating that the decrease of V_{OC} is not due to the worse band alignment [132]. Because the power of a white-light lamp is lower than that of the AM1.5 G spectrum, I execute 480-min illumination to obtain a comparable dose of illumination. Detailed analysis (Fig. 6.17) suggests that illumination is less likely to change the non-radiative relaxation of higher electronic states, vibrational relaxations, and radiative relaxations of the perovskite even after 480-min illumination.

To further confirm this finding, I measure the photovoltaic external quantum efficiencies (EQEs) for the fresh PSCs and the same PSCs after the degradation process under vacuum. Indeed, Fig. 6.15d shows that the feature of $FAPbI_3$, as the minority phase, appears after phase segregation. This could be due to an outgassing process of MA molecules from the perovskite layer when the PSCs are operated under vacuum [74]. Hence, phase segregation occurs only when PSCs are operated under vacuum, agreeing well with the GIWAXS study discussed above. This minority phase leads to an increasing charge carrier density due to energetic confinement within a small fraction of the total film volume. All charge carriers tend to funnel into the $FAPbI_3$ having the lowest bandgap. This increased charge carrier density could enhance the radiative recombination, given that the bimolecular radiative recombination process is much stronger than the monomolecular non-radiative recombination [106].

The same study suggested that the V_{OC} loss is pinned by the increasing amount of a low bandgap iodide-rich phase. I execute the device simulation via SCAPS-1D based on the ‘drift-diffusion’ model to simulate the effects on devices by increasing the radiative recombination coefficient of the perovskite materials [77]. Even if the radiative recombination coefficient of the MAFA perovskite increases from 3.16×10^{-12} to 3.16×10^{-6} in the simulation for the perovskite layer, there is only a voltage penalty of 26 mV (Fig. 6.16c and f). Thus, the larger voltage loss observed in vacuum conditions cannot result only from phase segregation.

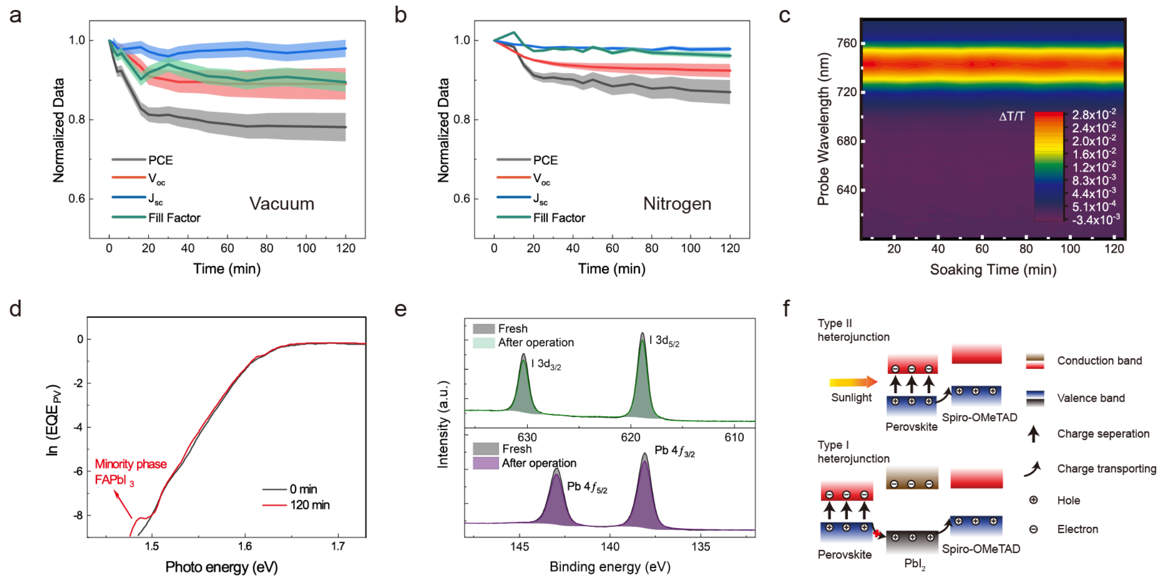

Figure 6.15: Degradation Mechanisms of MAFA PSCs under the ISOS-L-1I protocol in different atmospheres. (a) Evolution of PCE (black), J_{SC} (blue),V_{OC} (red), and FF (green) measured by the reverse scan (from 1.3 V to -0.2 V) under vacuum. (b) Evolution of PCE, J_{SC}, V_{OC}, and FF measured by the reverse scan in nitrogen. For (a) and (b), the shaded areas indicate error bars extracted from the standard deviation of normalized PCE, J_{SC}, V_{OC} and FF values of 6 devices operated are operated under the ISOS-L-1 protocol in different atmospheres. (c) In situ transient absorption spectra (100 to 120 ps average) of the perovskite active layer as a function of illumination time under vacuum (3.4×10^{-3} Pa). The colour bar indicates the change in the transmission (absorption) of the broadband probe pulse when the sample is photoexcited by a pump pulse. (d) Photovoltaic external quantum efficiencies (EQE-PV) of $(MAPbBr_3)_{0.17}(FAPbI_3)_{0.83}$ PSCs measured before and after the operation in vacuum. (e) The change of XPS I3d and Pb4f spectra for $(MAPbBr_3)_{0.17}(FAPbI_3)_{0.83}$ PSCs measured before and after the operation under voltage-bias conditions, and the baseline of data is extracted through a Shirley background correction. (f) Schematic illustration for the effects of the migration of PbI_2 to the interface between perovskite and spiro-OMeTAD. Reprinted with permission from [59]. Copyright 2021, Nature energy.

Given that phase segregation of PSCs does not influence the device performance strongly, I predict that there must be additional changes at interfaces affecting the final device performance significantly. A previous study using advanced in situ transmission electron microscopy revealed that the voltage-bias scan for PSCs could cause the formation of PbI_2 nanoparticles between the perovskite and the spiro-OMeTAD interface. I confirm this phenomenon via an XPS study (Fig. 6.15e). From a detailed quantitative analysis, I find that the I/Pb ratio decreases from 3.11 to 2.71 after a continuous voltage-bias scan

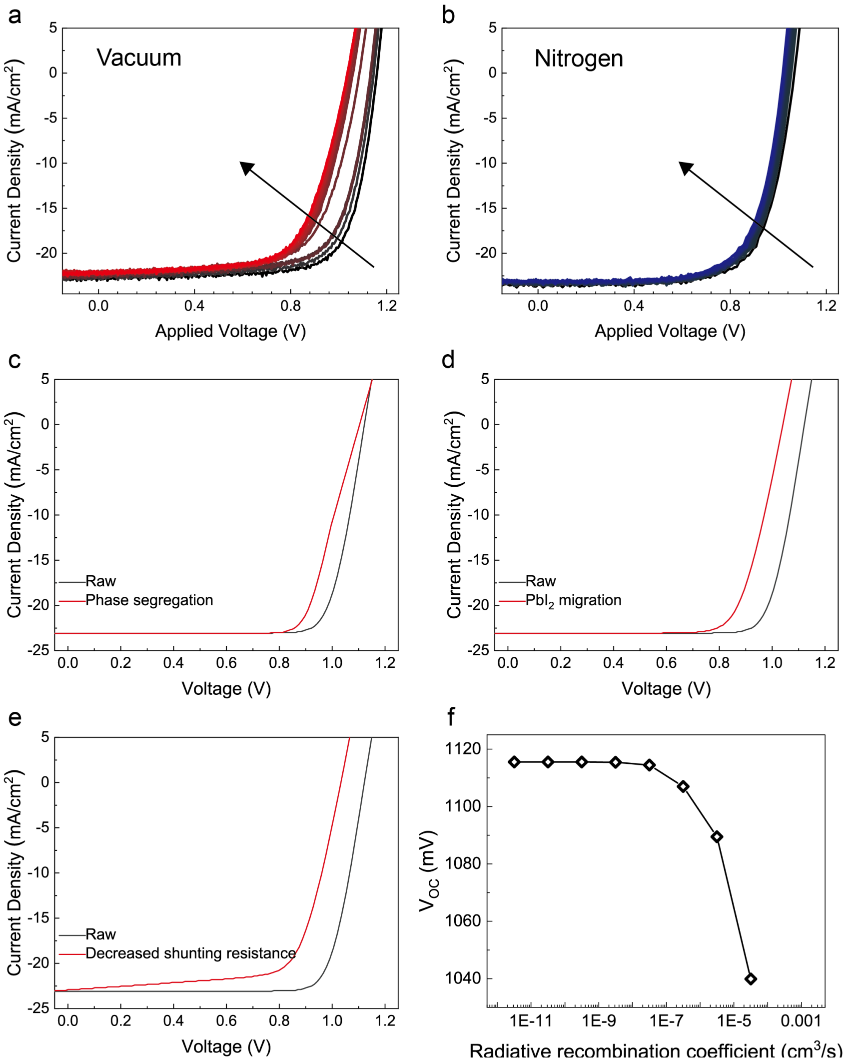

Figure 6.16: PSC data and device simulation via 'drift-diffusion' model based on different situations. J-V evolution of perovskite solar cells under operating conditions for 120 min in (a) vacuum and (b) nitrogen. Calculated J-V curves for (c) phase segregation of PSCs, (d) PbI_2 migrating into the hole transporting layer and (e) shunting pathway introduced into perovskite solar cells. (f) Relation between radiative recombination coefficient and open-circuit voltage calculated with the 'drift-diffusion' model. Reprinted with permission from [59]. Copyright 2021, Nature energy.

for 30 min. The decrease of the I/Pb ratio confirms that PbI_2 migrates into the interface between the perovskite film and spiro-OMeTAD.

I also investigate the effect of existing PbI_2 between the perovskite and the hole-transport layer using a simulation of the 'drift-diffusion' model. I find a voltage loss of 90 mV after inserting a PbI_2 layer between the perovskite and the hole-transport layer, showing that the excess PbI_2 at the interface reduces the V_{OC} dramatically (Fig. 6.16d). In addition,

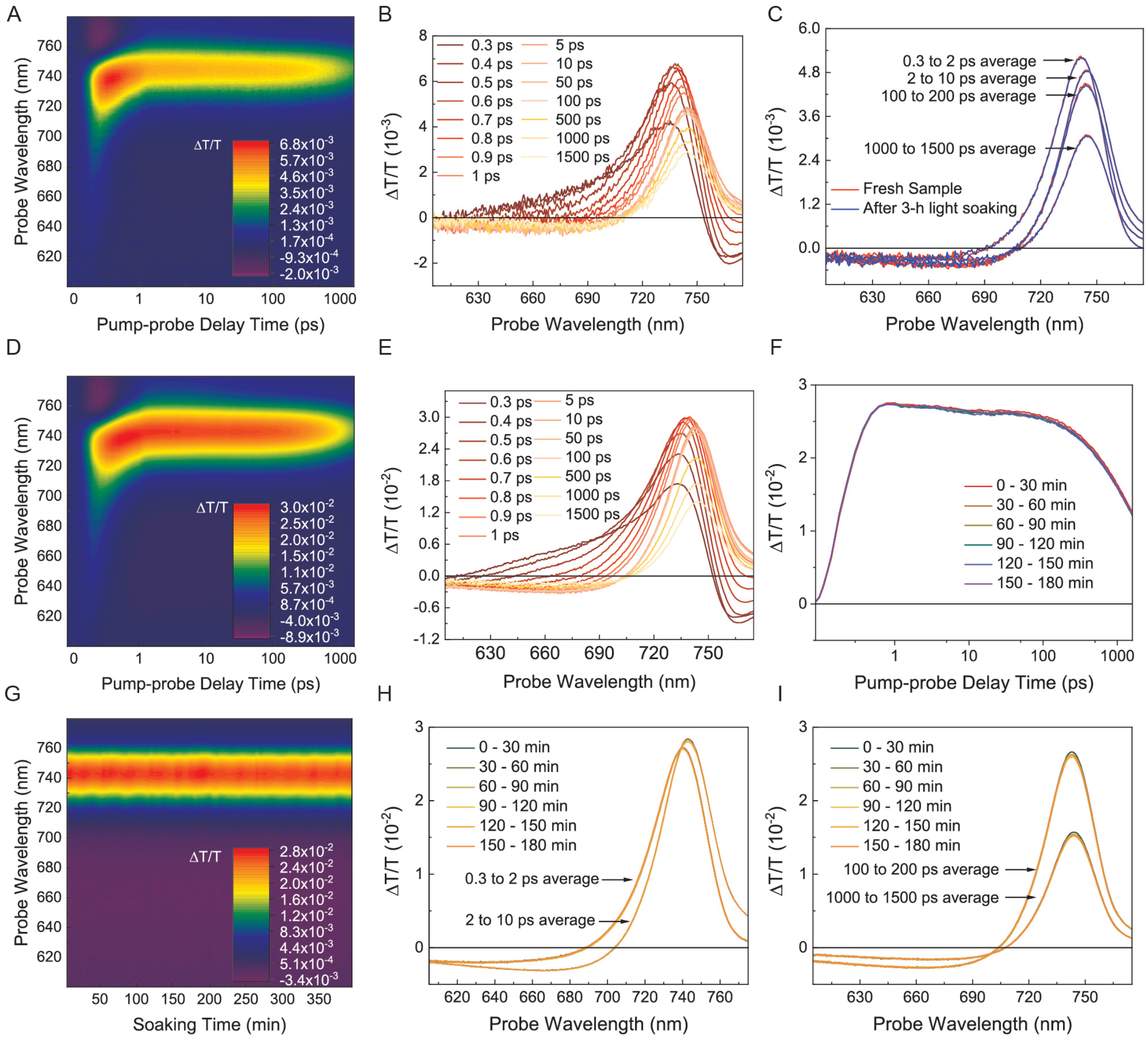

Figure 6.17: Evolution of transient absorption spectra for the perovskite film in vacuum. (a) TA map of the fresh perovskite film under a low-fluence 400-nm pump; (b) Spectra of the fresh perovskite film under a low-fluence 400-nm pump; (c) Spectral comparison between the fresh sample and the illuminated sample; (d) TA map of the as-prepared perovskite film under a high-fluence 400-nm pump; (e) Spectra of the fresh perovskite film under a high-fluence 400-nm pump; (f) Kinetic comparison between the fresh sample and illuminated samples; (g) TA spectra within 400 minutes of exposure to femtosecond laser; (h) Early-time and (i) Late time spectral comparison between the fresh sample and illuminated samples. Reprinted with permission from [59]. Copyright 2021, Nature energy.

a control experiment for PSCs without excess PbI_2 under operation in a different atmospheric condition is executed. The drop of V_{OC} for PSCs is significantly suppressed after 120 min illumination in both, vacuum and nitrogen conditions (Fig. 6.18). Hence, I confirm that, under voltage-bias conditions, excess PbI_2 migrates to the interface between the perovskite and the spiro-OMeTAD layer irrespective of the type of atmosphere, thereby degrading the V_{OC} of the devices. The existence of PbI_2 changes the heterojunction type for PSCs from the staggering gap (type 2) to the straddling gap (type 1) because of the larger bandgap of PbI_2 (Fig. 6.15f). This change forms a worse band alignment for transporting holes. Furthermore, the GISAXS data show that small crystals break up during operation under vacuum, which can create pinholes. This results in shunting pathways, dramatically decreasing the shunt resistance of the devices [133]. From the 'drift-diffusion' simulation, I find that a decrease of the shunt resistance results in a decrease of the FF and V_{OC} of the devices decreases (Fig. 6.16e). This finding supports our results of a stronger degradation during operation under vacuum. Overall, the PbI_2 migration is one mechanism, which causes voltage loss and occurs for PSCs in both atmospheres. The segregation of the minority phase and the formation of small crystals from larger crystals (<40 nm) cause an additional voltage loss and a severe FF loss during operation under vacuum.

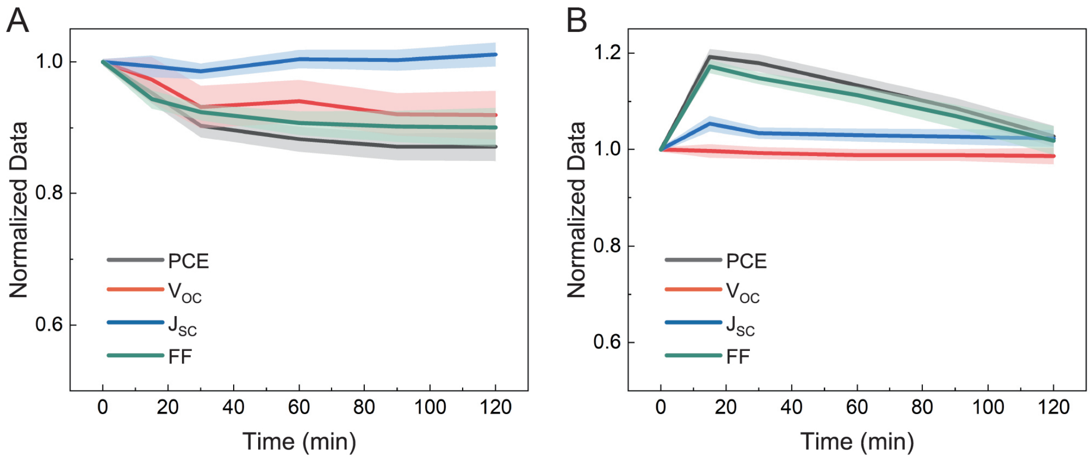

Figure 6.18: Evolution of PCE, J_{SC}, V_{OC} and FF of solar cells without excess PbI_2 in the reverse scan in different atmospheres. (a) Vacuum and (b) nitrogen. Six devices are operated under the ISOS-L-1 protocol in different atmospheres to extract error bars which are shown as the shaded area. Reprinted with permission from [59]. Copyright 2021, Nature energy.

6.7 Summary

I discover the kinetics between structural changes and phase segregation, and explain them in detail regarding thermodynamic theory. I also reveal the atmosphere-dependent degradation mechanisms for PSCs under different operation conditions. Operating PSCs under vacuum causes both, a large degree of lattice shrinkage and a spontaneous process for phase segregation of the mixed cation lead mixed halide PSCs. Importantly, these effects are mitigated in nitrogen. Therefore, I suggest using a nitrogen atmosphere with ambient pressure as a standard atmosphere for guiding scientific research and industrial development in the perovskite field. Furthermore, these new findings provide a constructive way to improve the long-term operational stability of this emerging photovoltaic technology via nitrogen encapsulation or the lattice fine-modification of perovskite materials.

7 Trace Water in Lead Iodide Limits the Performance of Perovskite Solar Cells

The reproducibility of highly efficient perovskite solar cells (PSCs) has long been a source of debate in research laboratories throughout the world. A well-known but little-discussed problem is how minor contaminants in raw materials impair the repeatability of high-performance PSCs. I show that the inevitability of water contamination in PbI_2 impacts device performance repeatability owing to PbI_2 fabrication techniques. I show that a little amount of water in PbI_2 generates a quicker crystallisation process in the perovskite layer during the annealing stage using synchrotron-based structural characterisation. This causes substantial unbalanced charge carrier mobility, which degrades the device performance and solar cell lifespan. Our PSCs obtain a certified PCE of 24.4 % by fine-tuning the water during manufacture.

7.1 Background

PSCs performance has been improved to a certified 25.7 %. However, in the field, consistency in different labs for creating highly efficient PSCs is a big difficulty, and only a few organisations across the globe can generate devices with certified PCE > 23%. For the reproductivity of highly efficient PSCs, it is therefore critical to study the underlying limits throughout the manufacturing process.

The device's repeatability is limited by a few factors: (i) material purity [134–136]; (ii) manufacturing pathway (such as a blend of raw material power or pure perovskite power) [137]; and (iii) processing environment (low-moisture atmospheres with relative humidity 20%). [138]. Material purity is one of these limiting criteria that researchers sometimes neglect because perovskite is a well-known defect-tolerance material. However, in order to attain optimal optoelectronic characteristics, the impact of contaminants on performance must be taken into account [139]. According to a prior study, a dehydrated PbI_2 procedure can boost PSCs' overall performance by twofold [134]. The water-based synthesis technique ”golden rain” reaction, on the other hand, has a basic limitation in terms of dehydration. The presence of residual water in the perovskite precursor, I believe, has an impact on crystal formation, charge carrier dynamics, and device performance.

7.2 Different Synthesis Methods of Lead Iodide and Relative Performance of Solar Cells

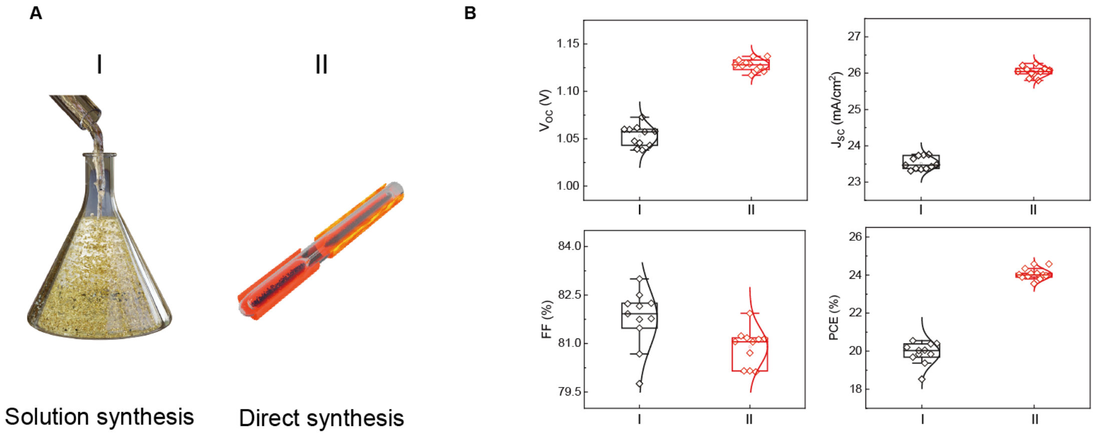

Figure 7.1: (A) Schematic diagram of solution synthesis and direct synthesis. (B) Statistics for 12 devices fabricated by different synthesis methods of PbI_2.

First, I examine the implications of various PbI_2 production techniques on device performance. Due to the water-based synthesis technique, the ”golden rain reaction” is a solution-process PbI_2 synthesis method (Fig. 7.1AI) with a maximum water level of 100 ppm [134]. While direct PbI_2 production by high-temperature evaporation might keep the water content in PbI_2 below 15 ppm [135]. The rising water content of PbI_2 has a syngenetic influence on device performance, as shown in Fig. 7.1B, lowering the open-circuit voltage (V_{OC}), short-circuit current (J_{SC}), and power conversion efficiency (PCE). I further establish that the detrimental effects of water content in PbI_2 on device performance are independent of fabrication techniques by manufacturing perovskite solar cells using the one-step anti-solvent approach for the components of $(MAPbBr_3)_{0.17}(FAPbI_3)_{0.83}$ (Fig. 7.2 [104]).

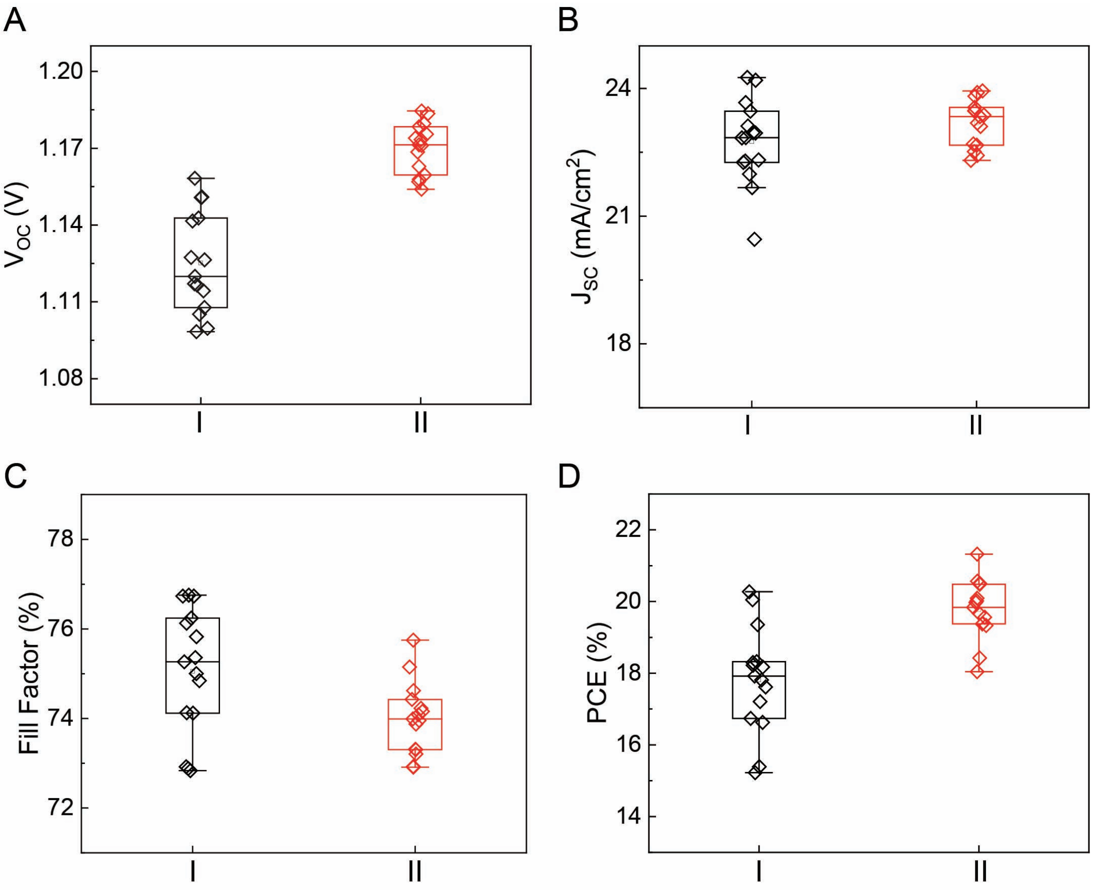

Figure 7.2: Statistical performance of the full batch of 15 of one-step anti-solvent fabricated ($FA_{0.79}MA_{0.16}Cs_{0.05}Pb(I_{0.83}Br_{0.17})_3$) perovskite solar cells. (A) open-circuit voltage; (B) short-circuit current; (C) fill factor; (D) power conversion efficiency.

7.3 Effect of Water Content in Lead Iodide on the Growth of the Perovskite Film

The effects of water concentration in PbI_2 on the kinetics of perovskite crystallisation are investigated using synchrotron-based grazing-incidence wide-angle x-ray scattering (GIWAXS). The perovskite layer is fabricated using a two-step inter-diffusion approach, and the annealing process is monitored at 150 ^oC in the air with a relative humidity of 35 % [88]. The crystallisation process is analysed and the temporal development of two-dimensional GIWAXS data is shown using a line profile integration (Fig. 7.3 and Fig. 7.4- 7.7). During the annealing process, increasing the amount of water in the perovskite films (from 0 ppm to 7000 ppm) consumes perovskite-related complexes ($q = 0.464, 0.508, 0.649$ $\mathring{A}^{-1}$) significantly quicker. With increased amounts of water, the reaction time of these complexes during the annealing process drops from 600 to 50 seconds, resulting in quicker development of the PbI_2 phase ($q = 0.896\ \mathring{A}^{-1}$) in perovskite films. I discovered that increasing water content might promote heterogeneous dominant nucleation for perovskite crystals by a comprehensive investigation of the perovskite-related complex phase ($q = 0.649\ \mathring{A}^{-1}$) using the Avrami equation (Fig. 7.8).

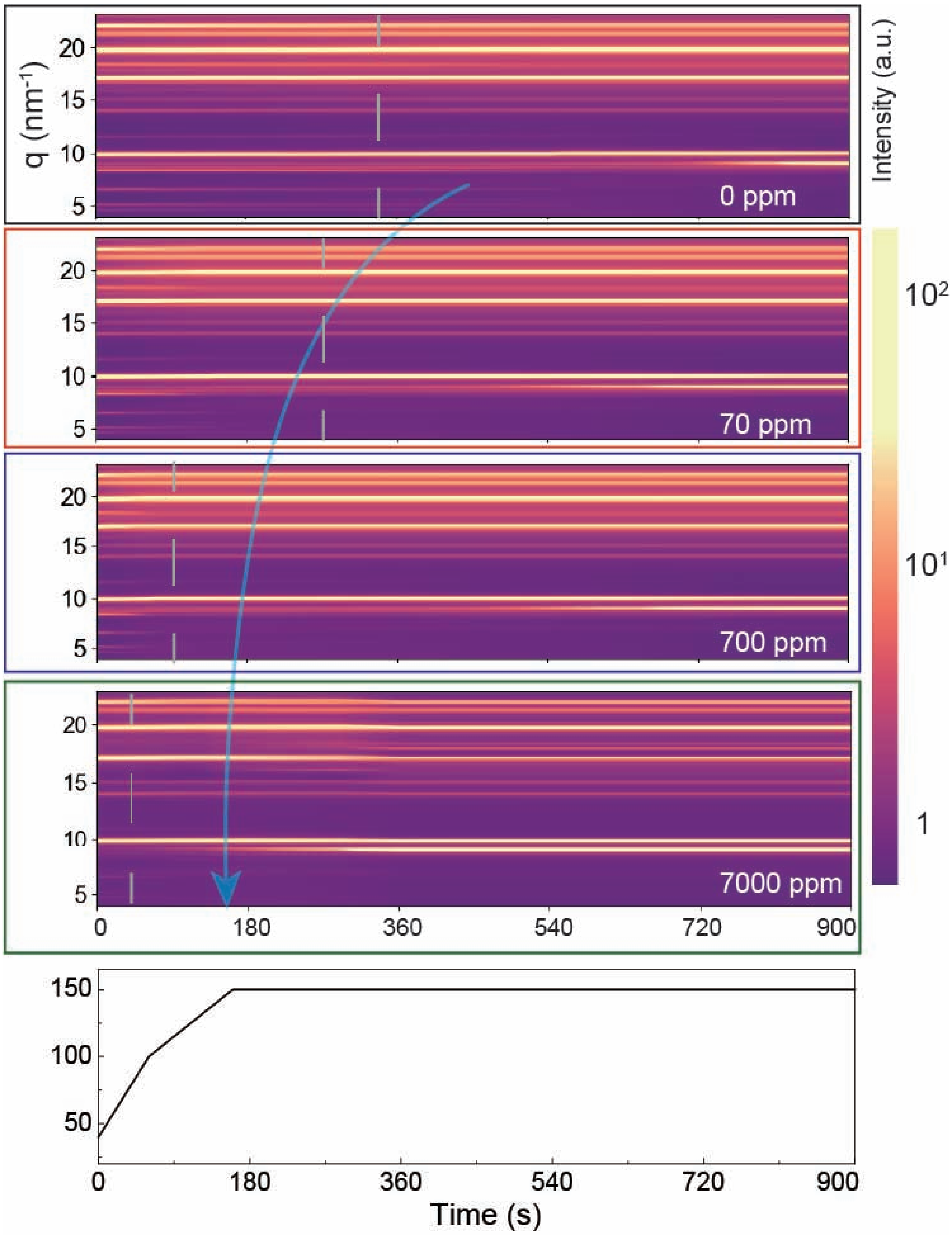

Figure 7.3: The X-ray scattering evolution during the perovskite film annealing process with different water contents in PbI_2 film.

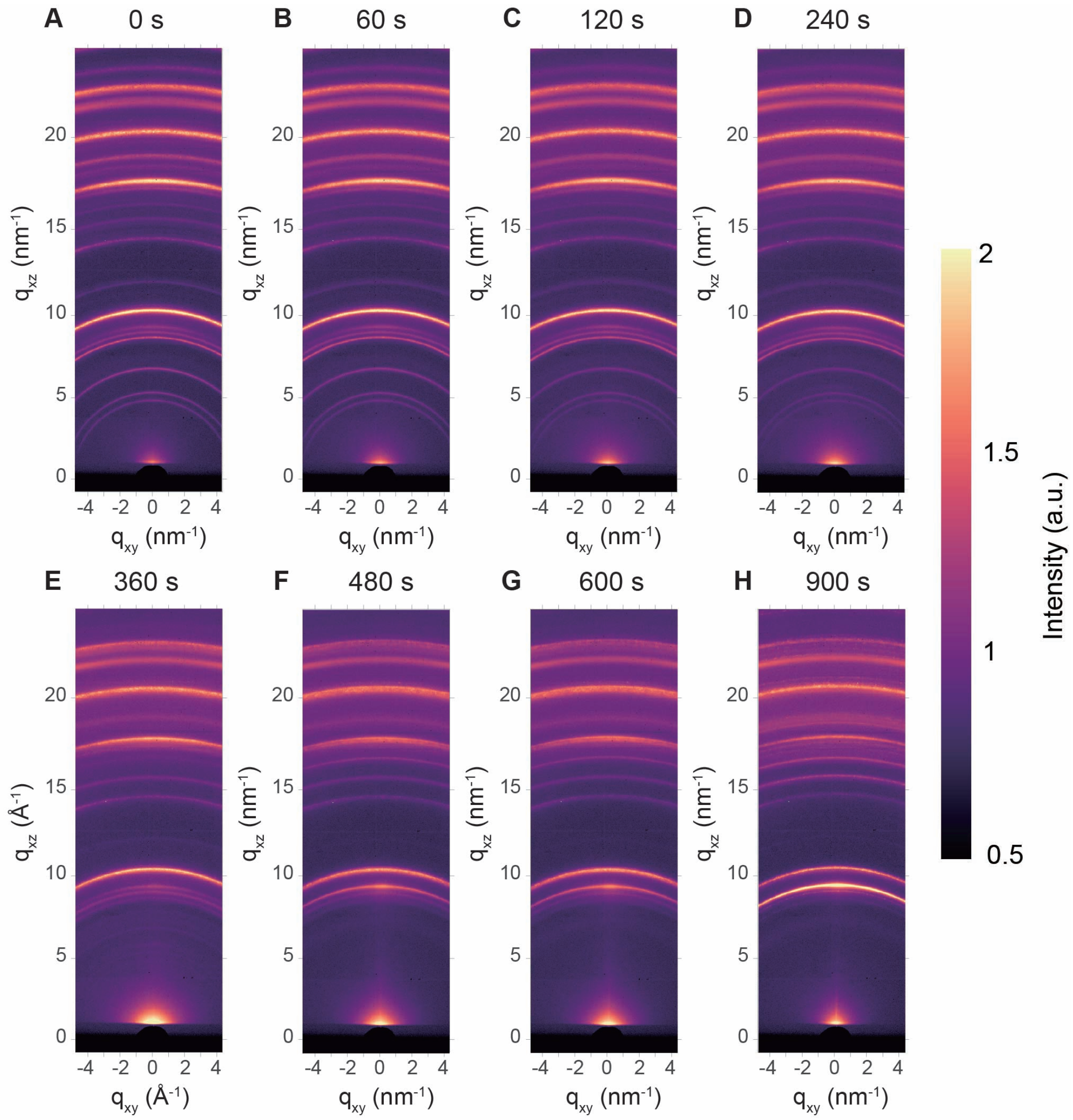

Figure 7.4: Evolution of scattering patterns for perovskite films with 0 ppm water in situ annealed at 150 ^{o}C. (A) 0 s; (B) 60 s; (C) 120 s; (D) 240 s; (E) 360 s; (F) 480 s; (G) 600 s; (H) 900 s.

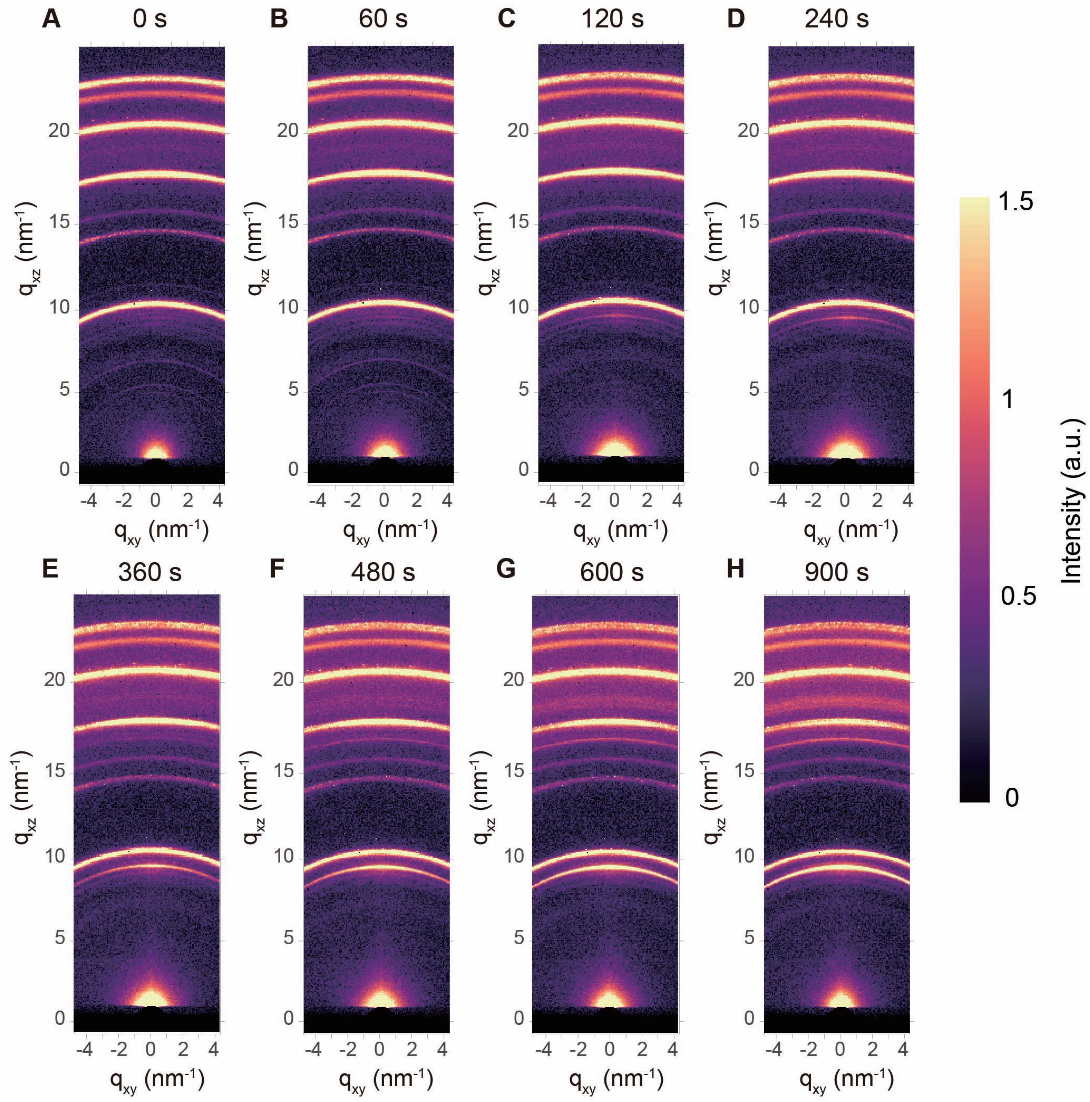

Figure 7.5: Evolution of scattering patterns for perovskite films with 70 ppm water in situ annealed at 150 ^{o}C. (A) 0 s; (B) 60 s; (C) 120 s; (D) 240 s; (E) 360 s; (F) 480 s; (G) 600 s; (H) 900 s.

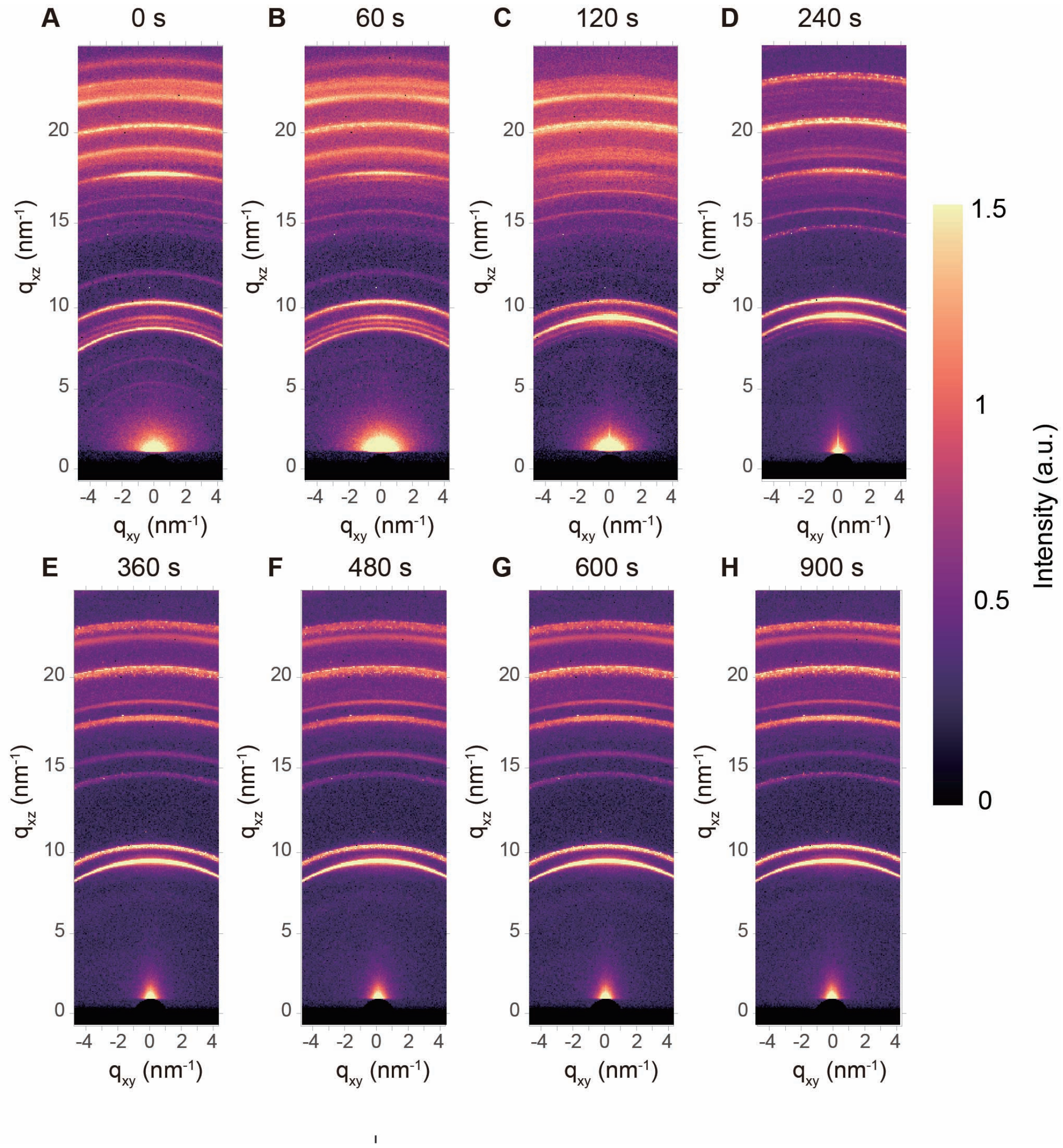

Figure 7.6: Evolution of scattering patterns for perovskite films with 700 ppm water in situ annealed at 150 ^{o}C. (A) 0 s; (B) 60 s; (C) 120 s; (D) 240 s; (E) 360 s; (F) 480 s; (G) 600 s; (H) 900 s.

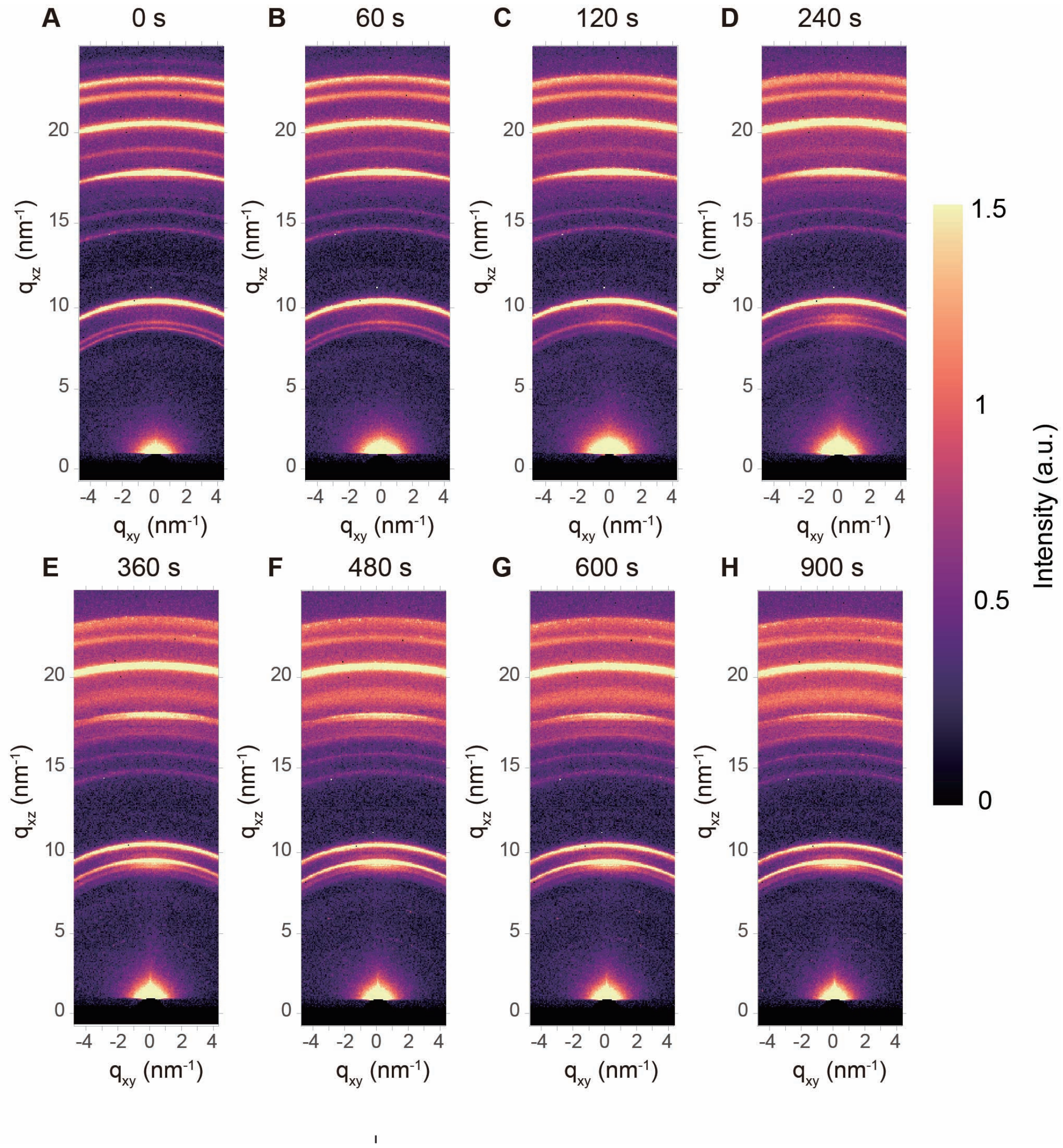

Figure 7.7: Evolution of scattering patterns for perovskite films with 7000 ppm water in situ annealed at 150 ^oC. (A) 0 s; (B) 60 s; (C) 120 s; (D) 240 s; (E) 360 s; (F) 480 s; (G) 600 s; (H) 900 s.

Scanning electron microscopy (SEM) pictures support the existence of heterogeneous dominant nucleation at the macroscopic level, providing proof of its occurrence (Fig. 7.9). Increased water concentration in perovskite films causes a competing process between heterogeneous and homogeneous nucleation, as shown in SEM images. I find that the heterogeneous dominant nucleation also results in the absence of the PbI_2 phase at the perovskite layer's surface, which does not increase device performance according to earlier publications (Fig. 7.10) [102]. I also look at the azimuthal integration of the PbI_2 phase at q = 1.835 $\AA^{-1}$, and I see that the intensity of the PbI_2 texture decreases noticeably

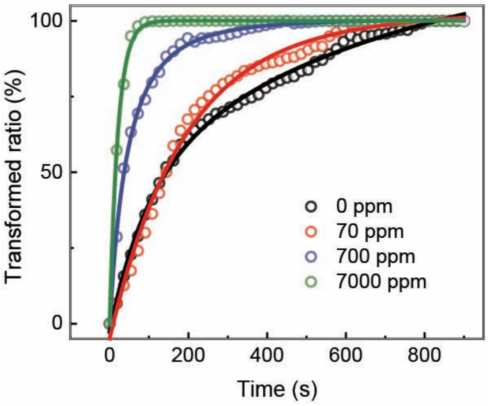

Figure 7.8: Experimental data extracted from 0, 70, 700, 7000 ppm of perovskite films at the peak with q = 0.64 $\mathring{A}^{-1}$ fitted to the Avrami equation, and K indicates the crystallization rate.

(Fig. 7.11 and Fig. 7.12). Due to a quick reaction of complexes, which causes the random distribution of the PbI_2 phase, more disordered textures for PbI_2 with a larger quantity of water in perovskite films are formed.

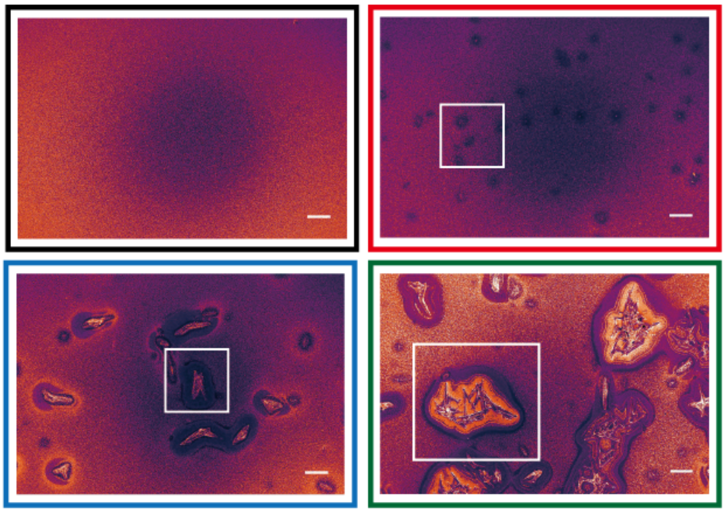

Figure 7.9: SEM images for perovskite films with 0 ppm water (black frame), 70 ppm water (red frame), 700 ppm water (blue frame), 7000 ppm water (green frame), and scale car is 100 μm.

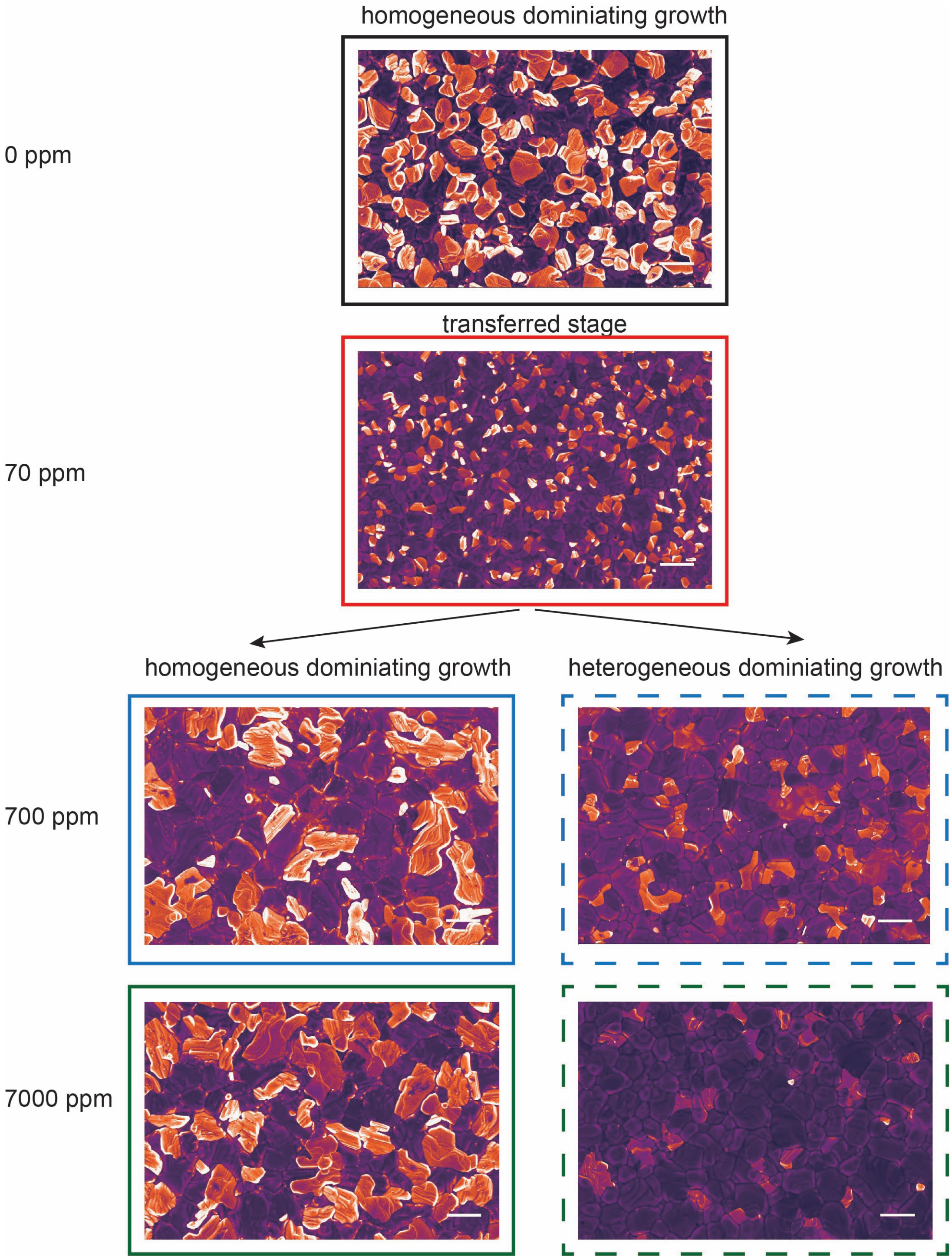

Figure 7.10: SEM images of annealed perovskite films with 0 (black frame), 70 (red frame), 700 (blue frame), and 7000 (green frame) ppm water. A higher amount of water ($>$ 70 ppm) in perovskite films results in the appearance of the homogeneous nucleation area (more lead PbI_2 at the surface, the frame with dash lines) and the heterogeneous nucleation area (less PbI_2 at the surface, the frame with solid lines). The bright area indicates the formation of PbI_2 according to previous reports.

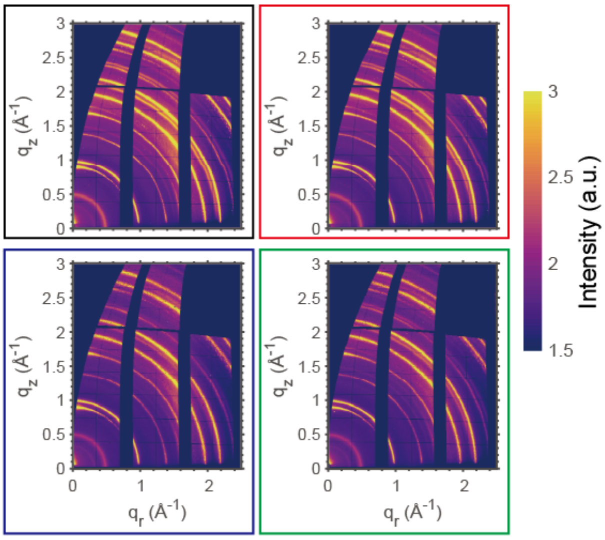

Figure 7.11: 2D GIWAXS data transferred to q-space obtained from the perovskite film with 0 ppm (black), 70 ppm (red), 700 ppm (blue), 7000 ppm (green) water.

I employ the continuous variation approach for expressing the stability constant of the PbI_2-DMSO complex in the perovskite film to investigate the inherent driving force of the quick consumption of perovskite-related complexes in the perovskite film (Fig. 7.13) [140]. As the amount of water in thePbI_2 precursor increases, the stability of complexes decreases considerably, culminating in a suspension (Fig. 7.14). This phenomenon might produce a rapid response of complexes during the annealing process of perovskite films due to a

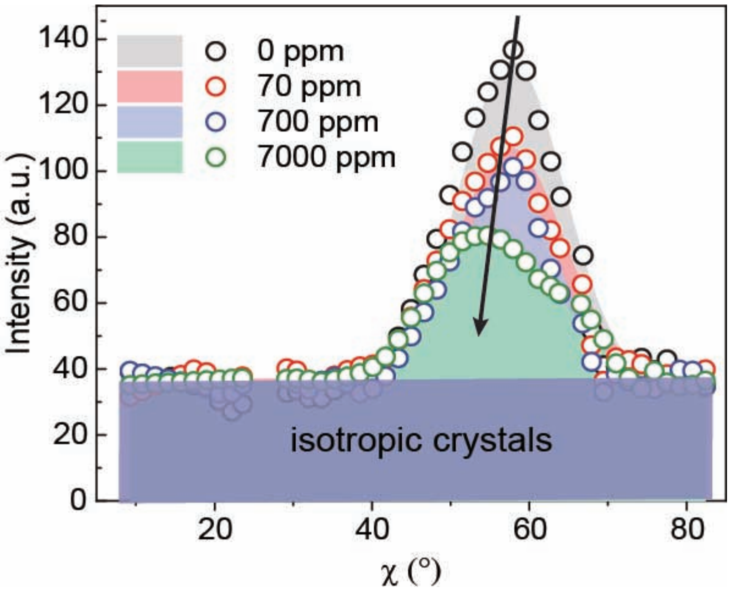

Figure 7.12: Texture evolution of perovskite film with different water content of PbI_2 cooperating during the annealing process.

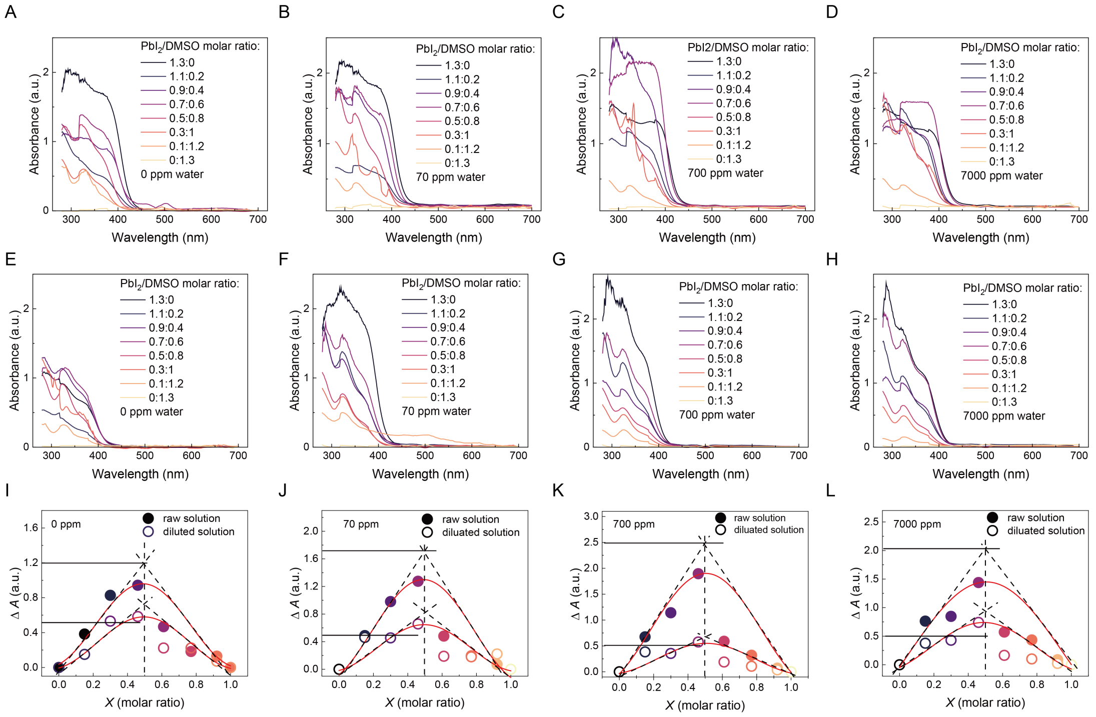

Figure 7.13: Light absorption spectra and continuous variation plots of PbI_2 and DMSO complex with different water content. (A) light absorption of 1.3 M PbI_2/DMSO in DMF solution with 0 ppm water; (B) light absorption of 1.3 MPbI_2/DMSO in DMF solution with 70 ppm water; (C) light absorption of 1.3 M PbI_2/DMSO in DMF solution with 700 ppm water; (D) light absorption of 1.3 M PbI_2/DMSO in DMF solution with 7000 ppm water; (E) light absorption of 0.65 M PbI_2/DMSO in DMF solution with 0 ppm water; (F) light absorption of 0.65 M PbI_2/DMSO in DMF solution with 70 ppm water; (G) light absorption of 0.65 M PbI_2/DMSO in DMF solution with light absorption of 0.65 M PbI_2/DMSO in DMF solution with diluted 700 ppm water; (H) light absorption of 0.65 M PbI_2/DMSO in DMF solution with 7000 ppm water; (I) continuous variation curve for PbI_2/DMSO in DMF solution with 0 ppm water; (J) continuous variation curve for PbI_2/DMSO in DMF solution with 70 ppm water; (K) continuous variation curve for PbI_2/DMSO in DMF solution with 700 ppm water; (L) continuous variation curve for PbI_2/DMSO in DMF solution with 7000 ppm water.

decrease in the quantity of complexes in the films. The PbI_2-DMSO complex possesses a strong coordination bonding with low water content in the film, as illustrated in Fig. 7.15. This causes the PbI_2 phase, which has a highly ordered texture, to crystallise more slowly during the annealing process. Due to the lower stability constant, increasing the amount of water destroys the coordination connection between the PbI_2-DMSO complex. Because of the weaker coordination bonds, the PbI_2 phase crystallises quickly and exhibits randomly oriented textures.

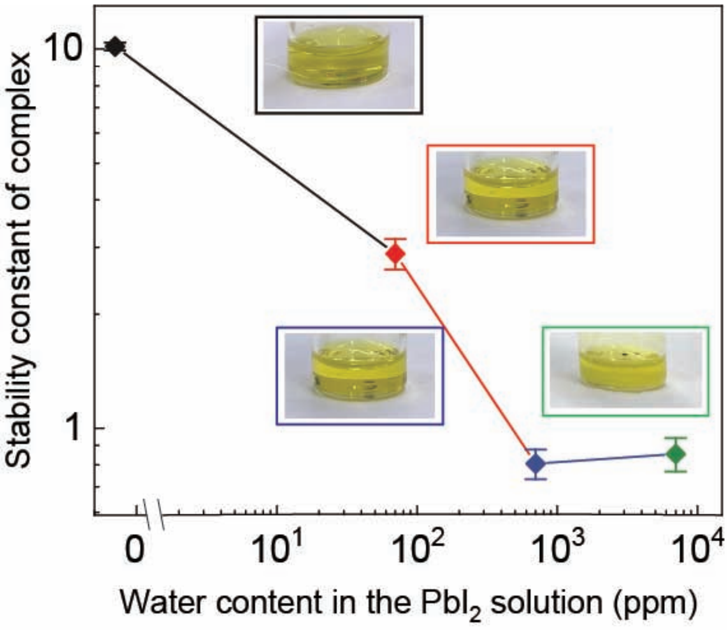

Figure 7.14: Stability constant of PbI_2 solutions with different amount of water.

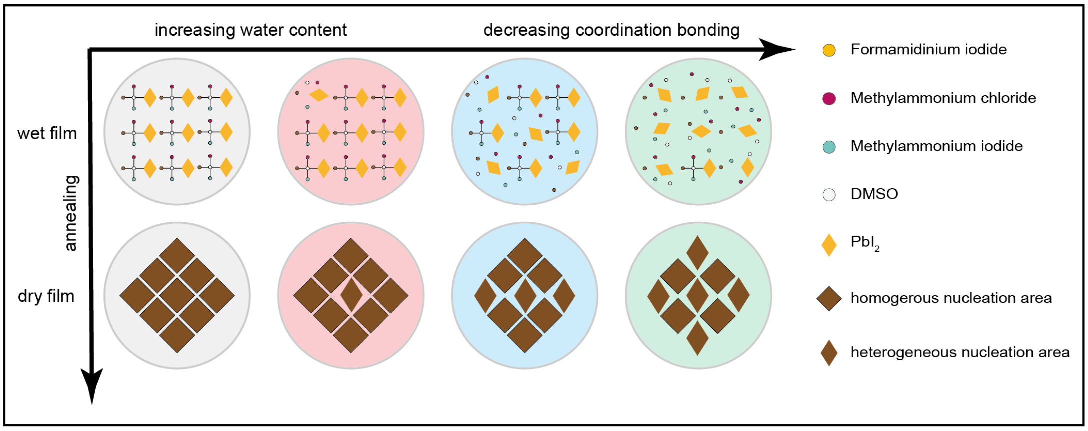

Figure 7.15: Schematic diagrams of the perovskite crystal formation with different water content in PbI_2 complex solution.

7.4 Effect of Water Content on the Performance of Solar Cells

I make PSCs for varying water content perovskite films and discover that the device performance degrades as the number of water on the PSCs increases (Fig. 7.16). I obtain a certified PCE of 24.3 % with a small aperture area and a certified PCE of 22.71 % with a large aperture area by fine-tuning the water content in PbI_2. Figures 7.17 and 7.18 show

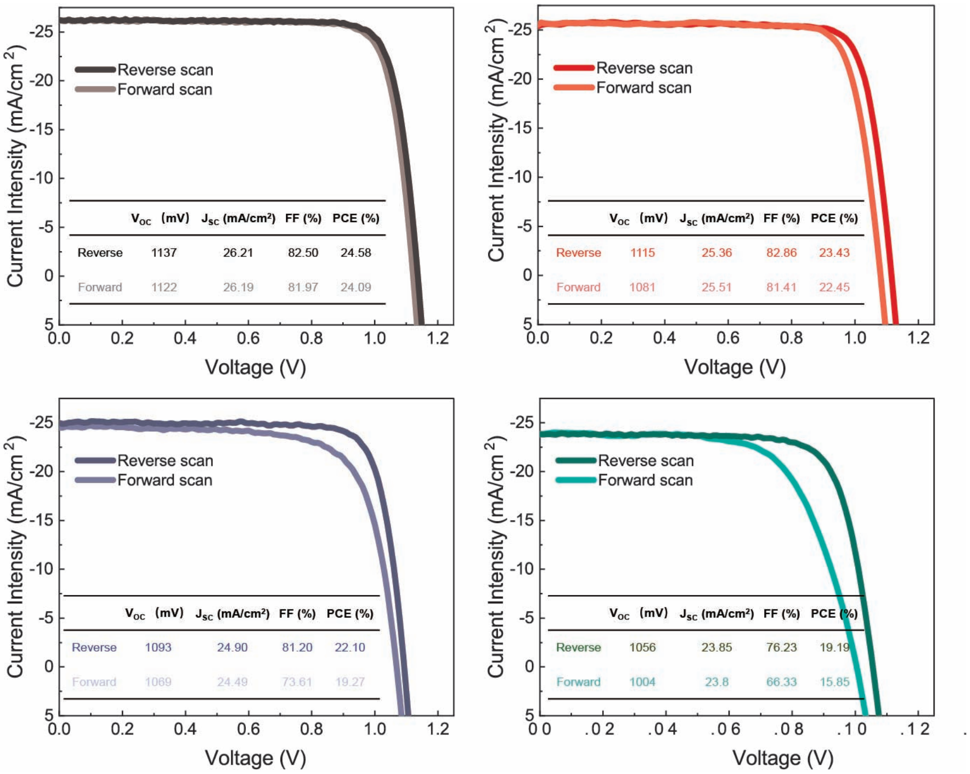

	V_{OC} (mV)	J_{SC} (mA/cm²)	FF (%)	PCE (%)
Reverse	1137	26.21	82.50	24.58
Forward	1122	26.19	81.97	24.09

	V_{OC} (mV)	J_{SC} (mA/cm²)	FF (%)	PCE (%)
Reverse	1115	25.36	82.86	23.43
Forward	1081	25.51	81.41	22.45

	V_{OC} (mV)	J_{SC} (mA/cm²)	FF (%)	PCE (%)
Reverse	1093	24.90	81.20	22.10
Forward	1069	24.49	73.61	19.27

	V_{OC} (mV)	J_{SC} (mA/cm²)	FF (%)	PCE (%)
Reverse	1056	23.85	76.23	19.19
Forward	1004	23.8	66.33	15.85

Figure 7.16: The performance of solar cells with 0 ppm, 70 ppm, 700 ppm, and 7000 ppm water in perovskite films.

the full device data as well as the external quantum efficiency spectrum. I use optical-pump THz-probe (OPTP) spectroscopy and time-resolved photoluminescence (TRPL) to expose the charge carrier dynamics of the perovskite layer with varied quantities of water [141, 142]. With increasing water pollution, Fig. 7.19 shows a decrease in charge-carrier total mobility. A high roughness for the perovskite layer with 700 ppm water, on the other hand, results in an undetectable signal for OPTP spectroscopy (Fig. 7.20).

In perovskite films, linear extrapolation is utilised to anticipate the development of mobility with increasing water. The cumulative charge carrier mobility decreases from 44.84 $cm^2V^{-1}s^{-1}$ (0 ppm) to 37.96 $cm^2V^{-1}s^{-1}$ (7000 ppm), potentially affecting device performance (Fig. 7.21). Meanwhile, due to sunlight recycling effects generated by morphological changes, I see a somewhat lower bimolecular recombination process with the higher water content film (reduction from $3.3{*}10^{-11}$ to $1.78{*}10^{-11}s^{-1}cm^3$). In addition, Fig. 7.22 indicates that with increased water content in perovskite films, the time-correlated single-photon counting (TCSPC) approach with TRPL produces a stronger trap assisted-charge carrier recombination (an increase from $1.33 * 10^6$ *to* $1.74 * 10^6 s^{-1}$.

I apply the 'drift-diffusion' model through SCAPS-1D to simulate device performance to quantify the aforementioned changes in charge carrier dynamics on device perfor-

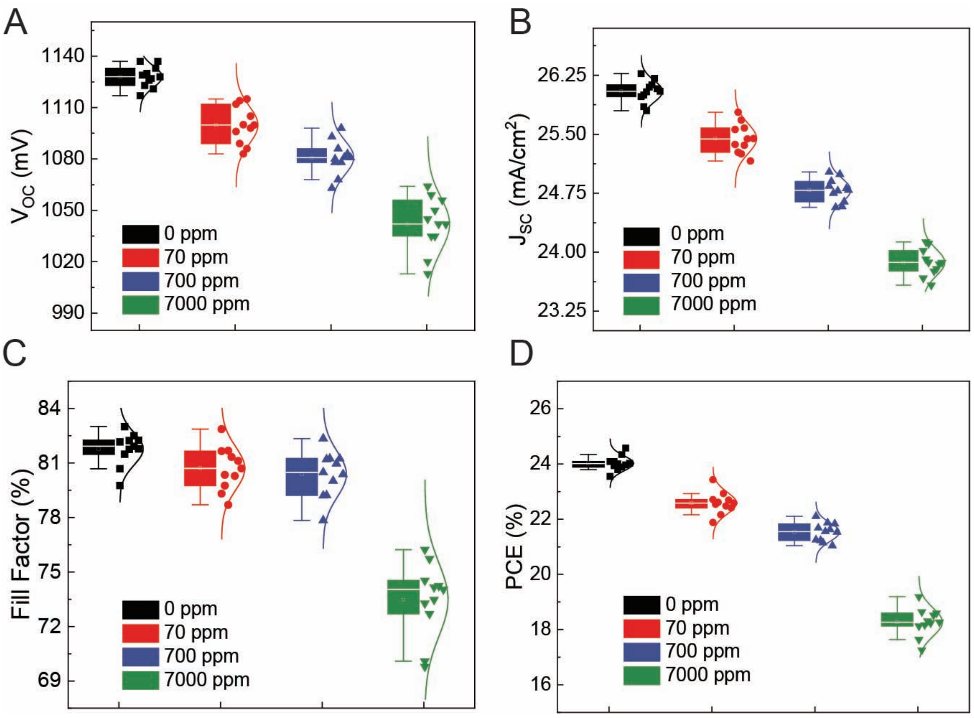

Figure 7.17: Device statistics shown in box plots (center line: average; box limit: standard deviation; whiskers: outliers) for (A) open-circuit voltage, (B) short-circuit current, (C) fill factor, (D) power conversion efficiency for solar cells with water content of 0 ppm (black), 70 ppm (red), 700 ppm (blue), 7000 ppm (green).

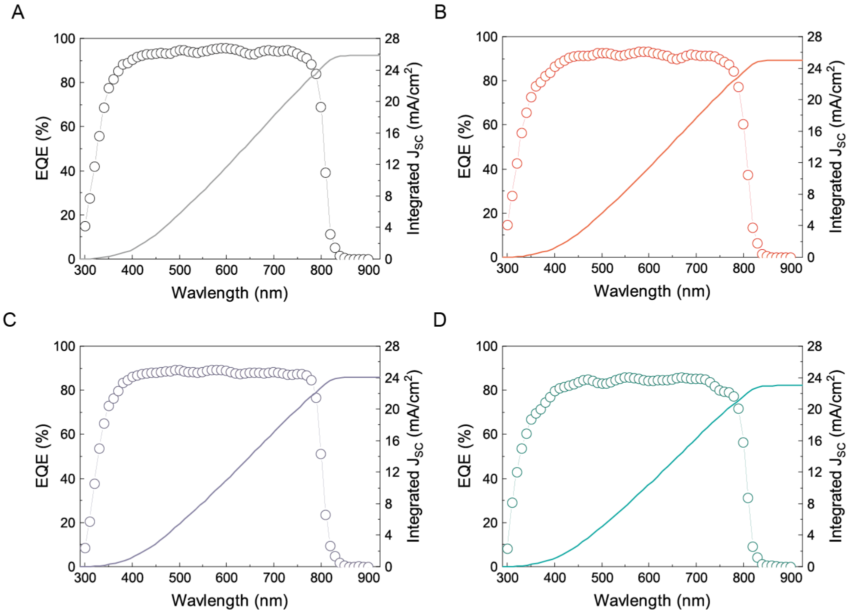

Figure 7.18: EQE and integrated JSC for the perovskite solar cells with 0 ppm (black), 70 ppm (red), 700 ppm (blue), 7000 ppm (green) water.

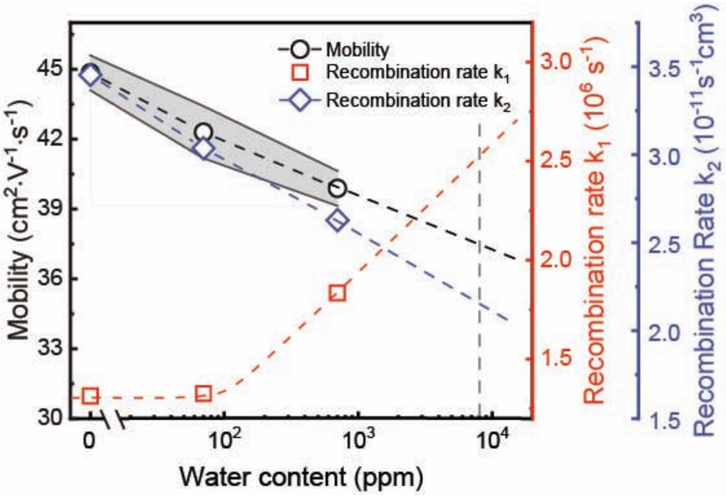

Figure 7.19: Charge carrier sum mobility, trap-assistant recombination rate and bimolecular recombination rate extracted from modelling OPTP and TRPL spectra for different amount of water in the perovskite layer.

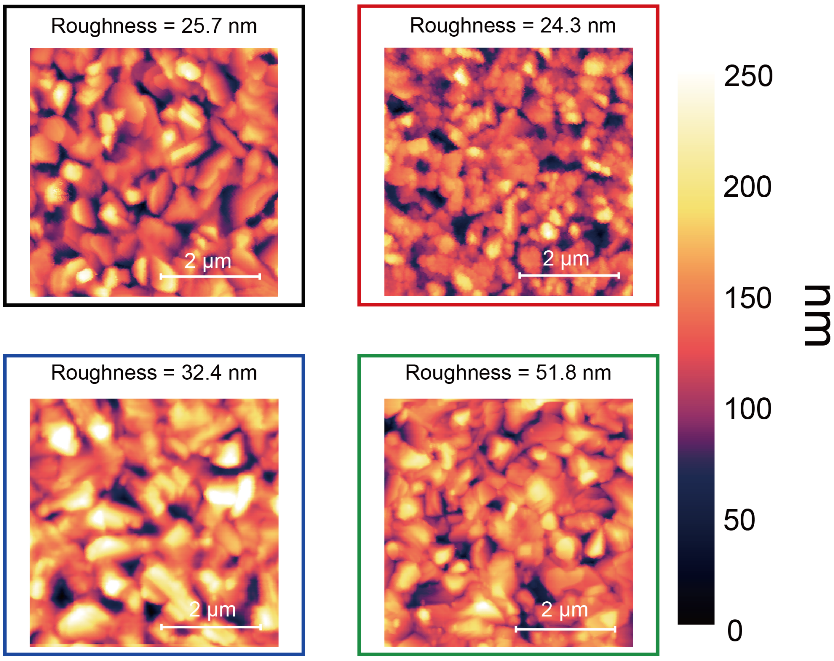

Figure 7.20: AFM images obtained from the perovskite film with 0 ppm (black), 70 ppm (red), 700 ppm (blue), 7000 ppm (green) water.

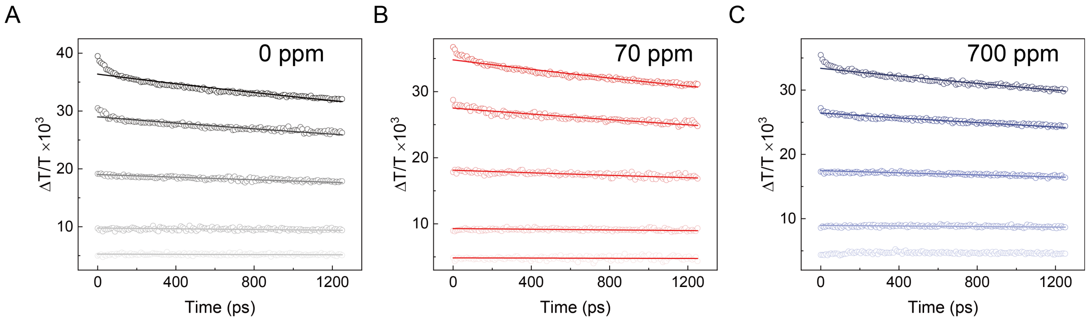

Figure 7.21: Photo-induced terahertz conductivity transients monitored over a 1 ns window following pulsed (15 fs) excitation at 400 nm with a range of pulse fluences for different perovskite films. (A) 0 ppm water; (B) 70 ppm water; (C) 700 ppm water.

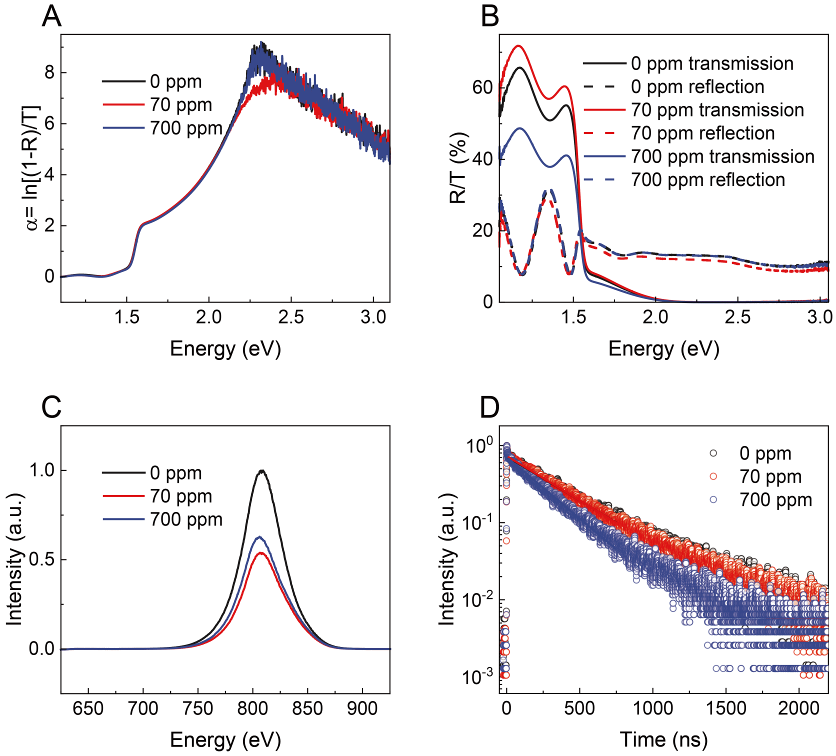

Figure 7.22: Optical properties of perovskite films. (A) the absorption spectrum of different perovskite films obtained from FTIR spectrometer; (B) the fractions of the reflected and transmitted light through different perovskite films; (C) the steady-state photoluminescence spectra of different perovskite films; (D)time-resolved photoluminescence spectra with the time-correlated single photon counting technique for perovskite films with different amount of water.

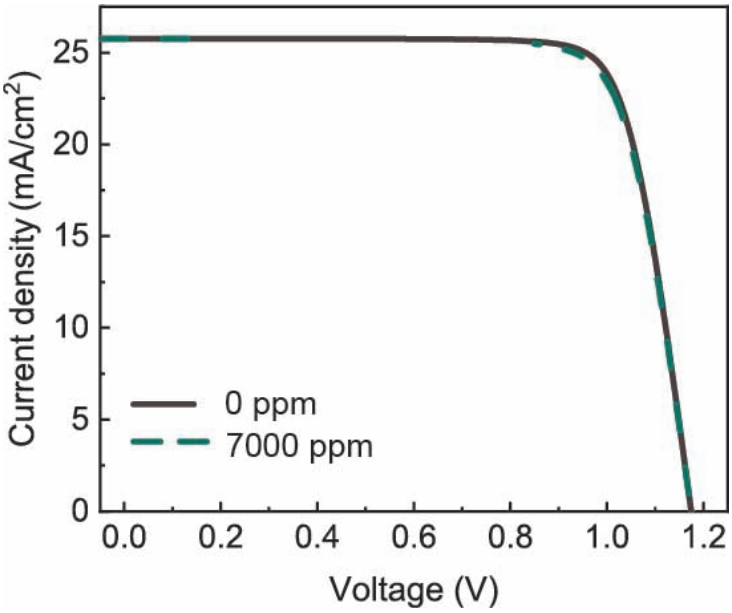

Figure 7.23: Simulated J-V curves with different amounts of water in the perovskite layer.

mance [77]. I first examine the effects of increased trap-assisted recombination rate in relation to trap density and deceased bimolecular recombination rate in relation to radiative recombination. I adjust the trap density, radiative recombination coefficient, and charge carrier mobility in the 'drift-diffusion' model by quantifying carrier density and trap density. The results demonstrate that applying relative modifications reduces device performance slightly (Fig. 7.23).

Due to the limitations of detecting sum charge carrier mobility with OPTP spectroscopy, I hypothesise that the imbalanced hole and electron mobility could lead to a significant drop in device performance as the amount of water in the perovskite layer increases [143].

I employ the space-charge limited current measurement to separate the hole and electron mobility to support our hypothesis (Fig. 7.24) [144]. With increasing amounts of water, I find that hole mobility falls from 13 to 0.02 $cm^2V^{-1}s^{-1}$ for the perovskite layer using hole-only and electron-only architectures as illustrated in Fig. 7.25. The electron mobility, on the other hand, exhibits just a little change when the water content rises. I ensure that the uneven hole and electron mobility in the increased amount of water leads to a severe loss in device performance by modelling the array among different hole and electron mobility for device performance (Fig. 7.26 and Fig. 7.27). The decreased hole carrier mobility severely limits the hole carrier movement. The charge carrier separation process is severely restricted by the decreased hole carrier mobility, resulting in an increased possibility of trap-assisted recombination and radiative recombination (Fig. 7.28).

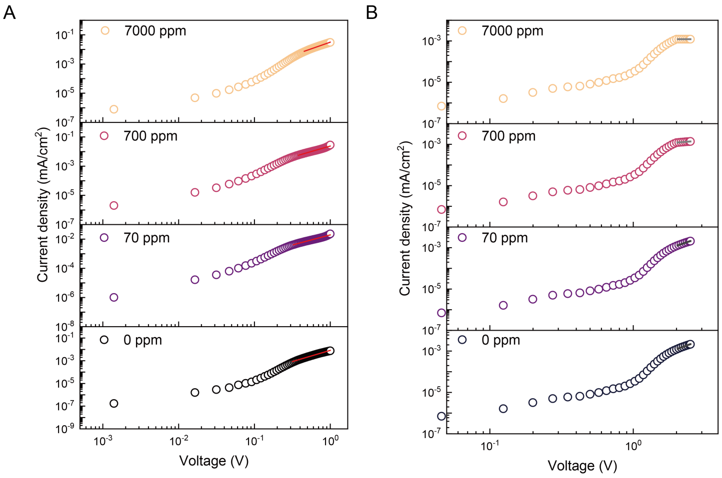

Figure 7.24: Evolution of J-V(log scale) curves from the measurement of SCLC with different water content perovskite films for (A) electron-only devices; (B) hole-only devices.

7.5 Effect of Water Content on the Operational Stability of Solar Cells

The operational stability of PSCs under a max power point tracking (MPPT) scenario must be assessed. As a result, I investigate the impact of water pollution on solar cells' long-term operational stability. Under an MPPT situation, I age type I and type II PbI_2 perovskite solar cells using the ISOS-L-1 technique [56]. After 350 hours of operation, the PSCs made with type I PbI_2 had lost roughly 60% of their relative performance. After 350 hours of continuous operation, the devices made with type II PbI_2 exhibit just a 20% reduction in relative efficiency. These findings show that PbI_2 pollution in water affects

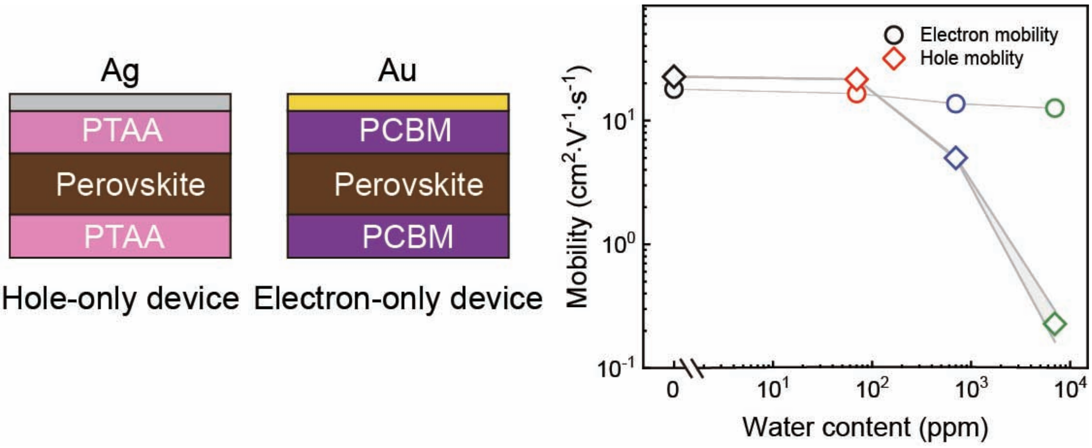

Figure 7.25: Schemes of applied hole-only, and electron-only devices for measuring the hole, and electron mobility separately obtained from pulsed space-charge limited current measurement.

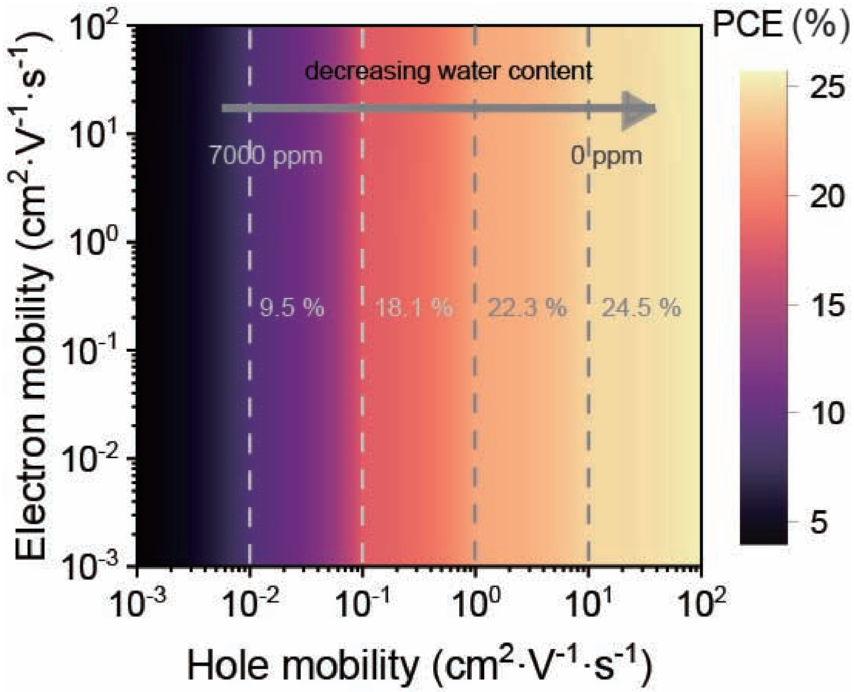

Figure 7.26: Dependence of PCE for solar cells with different electron and hole mobilities extracted from 'drift-diffusion' simulation.

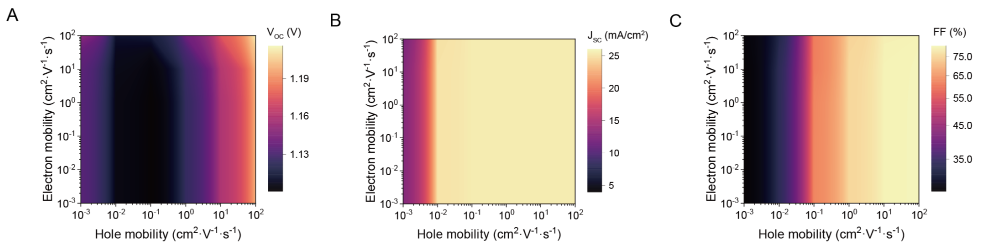

Figure 7.27: Dependence of device performance simulation through the "drift-diffusion" model with different electron and hole mobilities. (A) dependence of open-circuit voltage with different electron and hole mobilities; (B) dependence of short-circuit current with different electron and hole mobilities; (C) dependence of fill factor with different electron and hole mobilities.

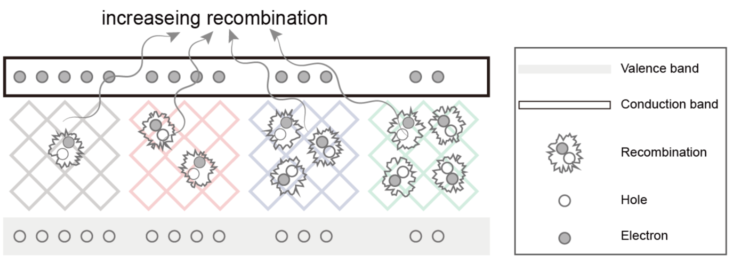

Figure 7.28: Schematic of the increasing recombination process due to the rising water content in different perovskite films.

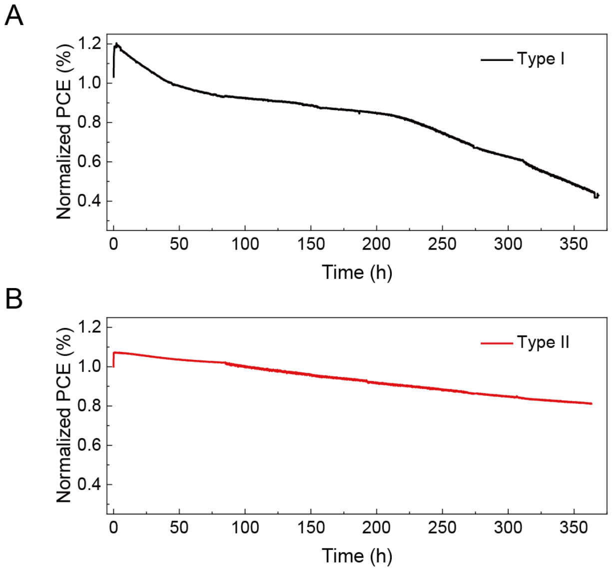

Figure 7.29: (A) Operational stability of perovskite solar cells fabricated by Type I PbI_2 under the ISOS-L-1 protocol (maximum power point tracking, in N_2, continuous one-sun illumination at 25 °C). (B) Operational stability of perovskite solar cells fabricated by Type II PbI_2 under the ISOS-L-1 protocol.

the operational stability of PSCs. Our findings, which show that water contamination in PbI_2 has a significant impact on device performance and operational stability for PSCs, should encourage researchers to pay attention to the purity of raw materials.

7.6 Summary

I demonstrate how the inevitability of water contamination in PbI_2 affects device performance repeatability due to PbI_2 production procedures. Using synchrotron-based structural characterization, I show that a little quantity of water in PbI_2 causes a faster crystallisation process in the perovskite layer during the annealing stage. This results in significant imbalanced charge carrier mobilities, which lowers device performance and solar cell longevity. By fine-tuning the water during manufacturing, our PSCs achieve a certified PCE of 24.4 %.

8 Conclusion

To summarize, this thesis discusses three topics for perovskite solar cells. One is how two-dimensional polymorphs affect the orientation of perovskite crystals, and the other is how atmospheres affect the degradation mechanisms of perovskite solar cells. Also, how the trace water affects the performance and operational stability is discussed. The focus is on perovskite solar cells with n-i-p planar architecture devices, which are compatible with large-scale industrial fabrication due to their low-temperature solution-based methods. I mainly use GIWAXS and GISAXS to analyze the scientific questions in the perovskite field, and I figure out how to modify the orientation of perovskite crystals. Combining characterization techniques like UV-vis, SEM, TRPL and I-V measurement, I understand the relationship between device performances and crystal orientations. Synchrotron-based operando experiments enable us to understand the intermediate status of how atmospheres affect the degradation mechanisms of perovskite solar cells. With the support of DFT, EQE, XPS and SCAPS-1D simulation, the comprehensive degradation mechanisms of atmospheres of perovskite solar cells are figured out. Synchrotron-based in-situ annealing experiments make us understand how trace water in lead iodide can affect the crystallization process, and cause a heterogeneous growth for the perovskite material. Combining with the help of TRPL, OPTP and SCAPS-1D, I further understand that heterogeneous crystallization can cause imbalanced mobility for electrons and holes, which decreases the performance of PSCs.

For the first project in Chapter 5, I discovered that adding varying concentrations of p-f-PEAI results in the formation of a novel face-on texture of the cubic phase of perovskite films, as well as an increase in texture strength. TRPL measurements reveal a trade-off mechanism for p-f-PEAI doping of perovskite materials in terms of charge carrier dynamics. I hypothesise that the change in morphology and textural strength caused by doping with p-f PEAI suppresses the charge carrier quenching effect and is advantageous to charge extraction. Furthermore, by carefully controlling the p-f-PEAI content, I enhance the PCE distribution in terms of a decreased PCE spread of PSCs without sacrificing the possible PCE. As a result, increasing texture strength may have an impact on the charge-carrier dynamics of perovskite films. Equally significant, I have demonstrated a crucial step toward the manufacture of PSCs with both a high and reproducible PCE. Such advancements are required to achieve real-world applications. This, I hope that, will have an impact on future advancements in perovskite-related optoelectronic devices, as well as open the way for a greater understanding of structure-dependent material properties and the creation of theoretical models.

For the second project in Chapter 6, I explore the kinetics of structural changes and phase segregation and explain them thoroughly using thermodynamic theory. I also describe the atmospheric-dependent deterioration mechanisms of PSCs under various operating situations. When PSCs are operated under vacuum, they experience significant lattice shrinkage as well as spontaneous phase segregation of the mixed-cation lead mixed-halide PSCs. Importantly, nitrogen mitigates these effects. As a result, I propose that a nitrogen atmosphere at ambient pressure be used as a standard environment to guide the scientific study and industrial development in the perovskite field. Furthermore, these discoveries give constructive strategies (nitrogen encapsulation or lattice fine-modification of perovskite materials) to improve the long-term operational stability of this developing solar technology.

For the third project in Chapter 7, I demonstrate that the water content of the lead iodide used to fabricate perovskite film is the most crucial parameter that restricts the reproducibility and performance of PSCs, based on a comprehensive study. The presence of trace water in PbI_2 causes a heterogeneous crystallisation process and affects the microstructure of PbI_2 in perovskite films, according to our findings. As the quantity of water in the PbI_2 precursor increases, the stability constants of perovskite complexes in the precursor drop, causing distinct crystallisation processes and textures. I show that when the quantity of water in the PbI_2 precursor increases, charge carrier mobility decreases and non-radiative recombination processes enhance. The device's performance is limited by the highly unbalanced hole and electron mobilities in high water content films. All of these findings show that a trace quantity of water in PbI_2 can impact the reproducibility and PCE of PSCs by altering the crystallisation process of the perovskite, causing additional non-radiative recombination centres, and affecting the crystallisation process of the perovskite. Finally, I obtain a certified 24.4 % PCE for a tiny aperture area by fine-tuning the quantity of trace water in PbI_2. Meanwhile, I use the same method to get a certified 23.0 % PCE for big aperture solar cells, indicating that up-scaling manufacturing is a viable option.

In recent years, achievements have been made rapidly in understanding the outstanding features of perovskite solar cells and why these materials may produce highly efficient solar cells. Many studies have discussed the outstanding optoelectronic properties of perovskite materials, and they have attempted to link these features with device operating mechanisms and device performance. Many key material properties of perovskite films, such as light absorption, the concentration of trap states, exciton binding energies, and the diffusion lengths of charge carriers, are comparable or better than the best properties of photovoltaic materials with covalent bands (such as Si, GaAs, and CdTe) by high-temperature and vacuum technique. Many distinctive features including defect tolerance and ion migration, have been investigated in detail [145].

Although the big lattice constant and soft nature of perovskite materials lead to an obvious ion migration effect, it is unclear how these features lead to big dielectric constants and affect structural stability. Ion migration mechanisms have yet to be fully understood. Furthermore, one must learn how ion migrations affect carriers recombination in the perovskite layer and at adjunct interfaces, and researchers in the field should focus on the topics like charge separation, the suppression of current-voltage hysteresis, and the enhancement of perovskite stability. It is almost certain that fascinating and novel properties will be discovered in perovskite materials in the future. The enhanced understanding of perovskite materials' unique optoelectronic features would result in the development of prospective perovskite materials for less toxicity and better operational stability [145].

Bibliography

[1] M. A. Green, E. D. Dunlop, J. Hohl-Ebinger, M. Yoshita, N. Kopidakis, and X. Hao, "Solar cell efficiency tables (version 60)," *Progress in Photovoltaics: Research and Applications*, vol. 30, no. 7, pp. 629–638, 2022.

[2] Y. Cui, Y. Xu, H. Yao, P. Bi, L. Hong, J. Zhang, Y. Zu, T. Zhang, J. Qin, J. Ren, *et al.*, "Single-junction organic photovoltaic cell with 19% efficiency," *Advanced Materials*, vol. 33, no. 41, p. 2102420, 2021.

[3] M. Hao, Y. Bai, S. Zeiske, L. Ren, J. Liu, Y. Yuan, N. Zarrabi, N. Cheng, M. Ghasemi, P. Chen, *et al.*, "Ligand-assisted cation-exchange engineering for high-efficiency colloidal cs1- xfaxpbi3 quantum dot solar cells with reduced phase segregation," *Nature Energy*, vol. 5, no. 1, pp. 79–88, 2020.

[4] B. Sun, A. Johnston, C. Xu, M. Wei, Z. Huang, Z. Jiang, H. Zhou, Y. Gao, Y. Dong, O. Ouellette, *et al.*, "Monolayer perovskite bridges enable strong quantum dot coupling for efficient solar cells," *Joule*, vol. 4, no. 7, pp. 1542–1556, 2020.

[5] J. J. Yoo, G. Seo, M. R. Chua, T. G. Park, Y. Lu, F. Rotermund, Y.-K. Kim, C. S. Moon, N. J. Jeon, J.-P. Correa-Baena, *et al.*, "Efficient perovskite solar cells via improved carrier management," *Nature*, vol. 590, no. 7847, pp. 587–593, 2021.

[6] X. Zhao, T. Liu, Q. C. Burlingame, T. Liu, R. Holley III, G. Cheng, N. Yao, F. Gao, and Y.-L. Loo, "Accelerated aging of all-inorganic, interface-stabilized perovskite solar cells," *Science*, p. eabn5679, 2022.

[7] P. Müller-Buschbaum, "The active layer morphology of organic solar cells probed with grazing incidence scattering techniques," *Advanced materials*, vol. 26, no. 46, pp. 7692–7709, 2014.

[8] J. Schlipf and P. Müller-Buschbaum, "Structure of organometal halide perovskite films as determined with grazing-incidence x-ray scattering methods," *Advanced Energy Materials*, vol. 7, no. 16, p. 1700131, 2017.

[9] A. Stokes and A. Wilson, "The diffraction of x rays by distorted crystal aggregates-i," *Proceedings of the Physical Society (1926-1948)*, vol. 56, no. 3, p. 174, 1944.

[10] P. Scherrer, "Bestimmung der größe und der inneren struktur von kolloidteilchen mittels röntgenstrahlen," *Nachrichten von der Gesellschaft der Wissenschaften zu Göttingen, Mathematisch-Physikalische Klasse*, vol. 1918, pp. 98–100, 1918.

[11] J. I. Langford and A. Wilson, "Scherrer after sixty years: a survey and some new results in the determination of crystallite size," *Journal of applied crystallography*, vol. 11, no. 2, pp. 102–113, 1978.

[12] G. Hölzer, M. Fritsch, M. Deutsch, J. Härtwig, and E. Förster, "$k\alpha_{1,2}$ and $k\beta_{1,3}$ x-ray emission lines of the $3d$ transition metals," *Phys. Rev. A*, vol. 56, pp. 4554–4568, Dec 1997.

[13] G. C. Website, "Gi missing wedge." `http://gisaxs.com/index.php/GI_missing_wedge`, Last accessed on 2022-03-13.

[14] J. L. Baker, L. H. Jimison, S. Mannsfeld, S. Volkman, S. Yin, V. Subramanian, A. Salleo, A. P. Alivisatos, and M. F. Toney, "Quantification of thin film crystallographic orientation using x-ray diffraction with an area detector," *Langmuir*, vol. 26, no. 11, pp. 9146–9151, 2010.

[15] D. M. DeLongchamp, R. J. Kline, and A. Herzing, "Nanoscale structure measurements for polymer-fullerene photovoltaics," *Energy & Environmental Science*, vol. 5, no. 3, pp. 5980–5993, 2012.

[16] J. Rivnay, S. C. Mannsfeld, C. E. Miller, A. Salleo, and M. F. Toney, "Quantitative determination of organic semiconductor microstructure from the molecular to device scale," *Chemical reviews*, vol. 112, no. 10, pp. 5488–5519, 2012.

[17] Z. Jiang, "Gixsgui: a matlab toolbox for grazing-incidence x-ray scattering data visualization and reduction, and indexing of buried three-dimensional periodic nanostructured films," *Journal of Applied Crystallography*, vol. 48, no. 3, pp. 917–926, 2015.

[18] Y. Yoneda, "Anomalous surface reflection of x rays," *Phys. Rev.*, vol. 131, pp. 2010–2013, Sep 1963.

[19] A. Hexemer and P. Müller-Buschbaum, "Advanced grazing-incidence techniques for modern soft-matter materials analysis," *IUCrJ*, vol. 2, no. 1, pp. 106–125, 2015.

[20] P. Müller-Buschbaum, "Grazing incidence small-angle x-ray scattering: an advanced scattering technique for the investigation of nanostructured polymer films," *Analytical and bioanalytical chemistry*, vol. 376, no. 1, pp. 3–10, 2003.

[21] P. Müller-Buschbaum, "Gisaxs and gisans as metrology technique for understanding the 3d morphology of block copolymer thin films," *European Polymer Journal*, vol. 81, pp. 470–493, 2016.

[22] G. Renaud, R. Lazzari, and F. Leroy, “Probing surface and interface morphology with grazing incidence small angle x-ray scattering,” *Surface Science Reports*, vol. 64, no. 8, pp. 255–380, 2009.

[23] J. R. Levine, J. Cohen, Y. Chung, and P. Georgopoulos, “Grazing-incidence small-angle x-ray scattering: new tool for studying thin film growth,” *Journal of Applied Crystallography*, vol. 22, no. 6, pp. 528–532, 1989.

[24] R. Lazzari, “Isgisaxs: a program for grazing-incidence small-angle x-ray scattering analysis of supported islands,” *Journal of Applied Crystallography*, vol. 35, no. 4, pp. 406–421, 2002.

[25] R. Hosemann, W. Vogel, D. Weick, and F. Balta-Calleja, “Novel aspects of the real paracrystal,” *Acta Crystallographica Section A: Crystal Physics, Diffraction, Theoretical and General Crystallography*, vol. 37, no. 1, pp. 85–91, 1981.

[26] M. A. Green, A. Ho-Baillie, and H. J. Snaith, “The emergence of perovskite solar cells,” *Nature photonics*, vol. 8, no. 7, pp. 506–514, 2014.

[27] S. Pratap, F. Babbe, N. S. Barchi, Z. Yuan, T. Luong, Z. Haber, T.-B. Song, J. L. Slack, C. V. Stan, N. Tamura, *et al.*, “Out-of-equilibrium processes in crystallization of organic-inorganic perovskites during spin coating,” *Nature communications*, vol. 12, no. 1, pp. 1–9, 2021.

[28] S. Pratap, J. Schlipf, and P. Müller-Buschbaum, “Hierarchical structures from nanocrystalline colloidal precursors within hybrid perovskite thin films: implications for photovoltaics,” *ACS Applied Nano Materials*, vol. 3, no. 12, pp. 11701–11708, 2020.

[29] J. Schlipf, Y. Hu, S. Pratap, N. Hohn, L. Porcar, T. Bein, P. Docampo, and P. Müller-Buschbaum, “Shedding light on the moisture stability of 3d/2d hybrid perovskite heterojunction thin films,” *ACS Applied Energy Materials*, vol. 2, no. 2, pp. 1011–1018, 2019.

[30] J. Schlipf, P. Docampo, C. J. Schaffer, V. Körstgens, F. Hanusch, N. Giesbrecht, S. Bernstorff, T. Bein, and P. Müller-Buschbaum, “A closer look into two-step perovskite conversion with x-ray scattering,” *The journal of physical chemistry letters*, vol. 6, no. 7, pp. 1265–1269, 2015.

[31] A. Kojima, K. Teshima, Y. Shirai, and T. Miyasaka, “Organometal halide perovskites as visible-light sensitizers for photovoltaic cells,” *Journal of the american chemical society*, vol. 131, no. 17, pp. 6050–6051, 2009.

[32] M. M. Lee, J. Teuscher, T. Miyasaka, T. N. Murakami, and H. J. Snaith, “Efficient hybrid solar cells based on meso-superstructured organometal halide perovskites,” *Science*, vol. 338, no. 6107, pp. 643–647, 2012.

[33] M. Liu, M. B. Johnston, and H. J. Snaith, "Efficient planar heterojunction perovskite solar cells by vapour deposition," *Nature*, vol. 501, no. 7467, pp. 395–398, 2013.

[34] J. Burschka, N. Pellet, S.-J. Moon, R. Humphry-Baker, P. Gao, M. K. Nazeeruddin, and M. Grätzel, "Sequential deposition as a route to high-performance perovskite-sensitized solar cells," *Nature*, vol. 499, no. 7458, pp. 316–319, 2013.

[35] J. H. Heo, S. H. Im, J. H. Noh, T. N. Mandal, C.-S. Lim, J. A. Chang, Y. H. Lee, H.-j. Kim, A. Sarkar, M. K. Nazeeruddin, *et al.*, "Efficient inorganic–organic hybrid heterojunction solar cells containing perovskite compound and polymeric hole conductors," *Nature photonics*, vol. 7, no. 6, pp. 486–491, 2013.

[36] H. Min, D. Y. Lee, J. Kim, G. Kim, K. S. Lee, J. Kim, M. J. Paik, Y. K. Kim, K. S. Kim, M. G. Kim, *et al.*, "Perovskite solar cells with atomically coherent interlayers on sno2 electrodes," *Nature*, vol. 598, no. 7881, pp. 444–450, 2021.

[37] W. Shockley and H. J. Queisser, "Detailed balance limit of efficiency of p-n junction solar cells," *Journal of applied physics*, vol. 32, no. 3, pp. 510–519, 1961.

[38] J.-F. Guillemoles, T. Kirchartz, D. Cahen, and U. Rau, "Guide for the perplexed to the shockley–queisser model for solar cells," *Nature photonics*, vol. 13, no. 8, pp. 501–505, 2019.

[39] T. W. Crothers, R. L. Milot, J. B. Patel, E. S. Parrott, J. Schlipf, P. Müller-Buschbaum, M. B. Johnston, and L. M. Herz, "Photon reabsorption masks intrinsic bimolecular charge-carrier recombination in ch3nh3pbi3 perovskite," *Nano letters*, vol. 17, no. 9, pp. 5782–5789, 2017.

[40] R. Brendel, J. H. Werner, and H. J. Queisser, "Thermodynamic efficiency limits for semiconductor solar cells with carrier multiplication," *Solar energy materials and solar cells*, vol. 41, pp. 419–425, 1996.

[41] H.-S. Kim, C.-R. Lee, J.-H. Im, K.-B. Lee, T. Moehl, A. Marchioro, S.-J. Moon, R. Humphry-Baker, J.-H. Yum, J. E. Moser, *et al.*, "Lead iodide perovskite sensitized all-solid-state submicron thin film mesoscopic solar cell with efficiency exceeding 9%," *Scientific reports*, vol. 2, no. 1, pp. 1–7, 2012.

[42] K. Yao, F. Li, Q. He, X. Wang, Y. Jiang, H. Huang, and A. K.-Y. Jen, "A copper-doped nickel oxide bilayer for enhancing efficiency and stability of hysteresis-free inverted mesoporous perovskite solar cells," *Nano Energy*, vol. 40, pp. 155–162, 2017.

[43] X. Zheng, B. Chen, J. Dai, Y. Fang, Y. Bai, Y. Lin, H. Wei, X. C. Zeng, and J. Huang, "Defect passivation in hybrid perovskite solar cells using quaternary ammonium halide anions and cations," *Nature Energy*, vol. 2, no. 7, pp. 1–9, 2017.

[44] Y. Bai, Q. Dong, Y. Shao, Y. Deng, Q. Wang, L. Shen, D. Wang, W. Wei, and J. Huang, "Enhancing stability and efficiency of perovskite solar cells with crosslinkable silane-functionalized and doped fullerene," *Nature communications*, vol. 7, no. 1, pp. 1–9, 2016.

[45] T. Liu, K. Chen, Q. Hu, R. Zhu, and Q. Gong, "Inverted perovskite solar cells: progresses and perspectives," *Advanced Energy Materials*, vol. 6, no. 17, p. 1600457, 2016.

[46] D. Luo, W. Yang, Z. Wang, A. Sadhanala, Q. Hu, R. Su, R. Shivanna, G. F. Trindade, J. F. Watts, Z. Xu, *et al.*, "Enhanced photovoltage for inverted planar heterojunction perovskite solar cells," *Science*, vol. 360, no. 6396, pp. 1442–1446, 2018.

[47] Z. Ku, Y. Rong, M. Xu, T. Liu, and H. Han, "Full printable processed mesoscopic ch3nh3pbi3/tio2 heterojunction solar cells with carbon counter electrode," *Scientific reports*, vol. 3, no. 1, pp. 1–5, 2013.

[48] A. Mei, X. Li, L. Liu, Z. Ku, T. Liu, Y. Rong, M. Xu, M. Hu, J. Chen, Y. Yang, *et al.*, "A hole-conductor–free, fully printable mesoscopic perovskite solar cell with high stability," *science*, vol. 345, no. 6194, pp. 295–298, 2014.

[49] M. Stolterfoht, M. Grischek, P. Caprioglio, C. M. Wolff, E. Gutierrez-Partida, F. Peña-Camargo, D. Rothhardt, S. Zhang, M. Raoufi, J. Wolansky, *et al.*, "How to quantify the efficiency potential of neat perovskite films: Perovskite semiconductors with an implied efficiency exceeding 28%," *Advanced Materials*, vol. 32, no. 17, p. 2000080, 2020.

[50] M. Stolterfoht, P. Caprioglio, C. M. Wolff, J. A. Márquez, J. Nordmann, S. Zhang, D. Rothhardt, U. Hörmann, Y. Amir, A. Redinger, *et al.*, "The impact of energy alignment and interfacial recombination on the internal and external open-circuit voltage of perovskite solar cells," *Energy & environmental science*, vol. 12, no. 9, pp. 2778–2788, 2019.

[51] D. W. DeQuilettes, S. Koch, S. Burke, R. K. Paranji, A. J. Shropshire, M. E. Ziffer, and D. S. Ginger, "Photoluminescence lifetimes exceeding 8 μs and quantum yields exceeding 30% in hybrid perovskite thin films by ligand passivation," *ACS Energy Letters*, vol. 1, no. 2, pp. 438–444, 2016.

[52] I. L. Braly and H. W. Hillhouse, "Optoelectronic quality and stability of hybrid perovskites from mapbi3 to mapbi2br using composition spread libraries," *The Journal of Physical Chemistry C*, vol. 120, no. 2, pp. 893–902, 2016.

[53] M. Saliba, M. Stolterfoht, C. M. Wolff, D. Neher, and A. Abate, "Measuring aging stability of perovskite solar cells," *Joule*, vol. 2, no. 6, pp. 1019–1024, 2018.

[54] M. Aghaei, A. Fairbrother, A. Gok, S. Ahmad, S. Kazim, K. Lobato, G. Oreski, A. Reinders, J. Schmitz, M. Theelen, *et al.*, “Review of degradation and failure phenomena in photovoltaic modules,” *Renewable and Sustainable Energy Reviews*, vol. 159, p. 112160, 2022.

[55] R. Guo, M. V. Khenkin, G. E. Arnaoutakis, N. A. Samoylova, J. Barbé, H. K. H. Lee, W. C. Tsoi, and E. A. Katz, “Initial stages of photodegradation of mapbi3 perovskite: accelerated aging with concentrated sunlight,” *Solar RRL*, vol. 4, no. 2, p. 1900270, 2020.

[56] M. V. Khenkin, E. A. Katz, A. Abate, G. Bardizza, J. J. Berry, C. Brabec, F. Brunetti, V. Bulović, Q. Burlingame, A. Di Carlo, *et al.*, “Consensus statement for stability assessment and reporting for perovskite photovoltaics based on isos procedures,” *Nature Energy*, vol. 5, no. 1, pp. 35–49, 2020.

[57] R. Guo, A. Buyruk, X. Jiang, W. Chen, L. K. Reb, M. A. Scheel, T. Ameri, and P. Müller-Buschbaum, “Tailoring the orientation of perovskite crystals via adding two-dimensional polymorphs for perovskite solar cells,” *Journal of Physics: Energy*, vol. 2, no. 3, p. 034005, 2020.

[58] W. Chen, R. Guo, H. Tang, K. S. Wienhold, N. Li, Z. Jiang, J. Tang, X. Jiang, L. P. Kreuzer, H. Liu, *et al.*, “Operando structure degradation study of pbs quantum dot solar cells,” *Energy & Environmental Science*, vol. 14, no. 6, pp. 3420–3429, 2021.

[59] R. Guo, D. Han, W. Chen, L. Dai, K. Ji, Q. Xiong, S. Li, L. K. Reb, M. A. Scheel, S. Pratap, *et al.*, “Degradation mechanisms of perovskite solar cells under vacuum and one atmosphere of nitrogen,” *Nature Energy*, vol. 6, no. 10, pp. 977–986, 2021.

[60] N. Li, R. Guo, W. Chen, V. Körstgens, J. E. Heger, S. Liang, C. J. Brett, M. A. Hossain, J. Zheng, P. S. Deimel, *et al.*, “Tailoring ordered mesoporous titania films via introducing germanium nanocrystals for enhanced electron transfer photoanodes for photovoltaic applications,” *Advanced Functional Materials*, vol. 31, no. 34, p. 2102105, 2021.

[61] S. Liang, W. Chen, S. Yin, S. J. Schaper, R. Guo, J. Drewes, N. Carstens, T. Strunskus, M. Gensch, M. Schwartzkopf, *et al.*, “Tailoring the optical properties of sputter-deposited gold nanostructures on nanostructured titanium dioxide templates based on in situ grazing-incidence small-angle x-ray scattering determined growth laws,” *ACS Applied Materials & Interfaces*, vol. 13, no. 12, pp. 14728–14740, 2021.

[62] L. K. Reb, M. Böhmer, B. Predeschly, S. Grott, C. L. Weindl, G. I. Ivandekic, R. Guo, C. Dreißigacker, R. Gernhäuser, A. Meyer, *et al.*, “Perovskite and organic solar cells on a rocket flight,” *Joule*, vol. 4, no. 9, pp. 1880–1892, 2020.

[63] PerkinElmer, “Lambda uv/vis/nir and uv/vis spectrophotometers – 950, 850, and 650 , high-performance systems,” 2004. `https://resources.perkinelmer.com/lab-solutions/resources/docs/BRO_Lambda950850650Americas.pdf`, Last accessed on 2022-05-25.

[64] J. Schlipf, *The Morphology of Hybrid Perovskite Thin Films for Photovoltaic Application.* PhD thesis, Technische Universität München, 2018.

[65] Wikipedia, “X-ray photoelectron spectroscopy.” `https://en.wikipedia.org/wiki/X-ray_photoelectron_spectroscopy`, Last accessed on 2022-05-25.

[66] Wikipedia, “Photoluminescence.” `https://en.wikipedia.org/wiki/Photoluminescence`, Last accessed on 2022-05-26.

[67] PicoQuant, “Time-resolved photoluminescence.” `https://www.picoquant.com/applications/category/materials-science/time-resolved-photoluminescence`, Last accessed on 2022-05-26.

[68] Wikipedia, “Time-resolved spectroscopy, Transient-absorption spectroscopy.” `https://en.wikipedia.org/wiki/Time-resolved_spectroscopy`, Last accessed on 2022-05-26.

[69] PvEducation, “Measurement of solar cell efficiency, Electronics.” `https://www.pveducation.org/pvcdrom/characterisation/electronics`, Last accessed on 2022-05-27.

[70] PvEducation, “Solar cell operation, Quantum Efficiency.” `https://www.pveducation.org/pvcdrom/solar-cell-operation/quantum-efficiency`, Last accessed on 2022-05-27.

[71] G. Benecke, W. Wagermaier, C. Li, M. Schwartzkopf, G. Flucke, R. Hoerth, I. Zizak, M. Burghammer, E. Metwalli, P. Müller-Buschbaum, *et al.*, “A customizable software for fast reduction and analysis of large x-ray scattering data sets: applications of the new dpdak package to small-angle x-ray scattering and grazing-incidence small-angle x-ray scattering,” *Journal of applied crystallography*, vol. 47, no. 5, pp. 1797–1803, 2014.

[72] Wikipedia, “Scanning electron microscope.” `https://en.wikipedia.org/wiki/Scanning_electron_microscope`, Last accessed on 2022-05-27.

[73] Wikipedia, “Density functional theory.” `https://en.wikipedia.org/wiki/Density_functional_theory`, Last accessed on 2022-05-27.

[74] N. Li, Y. Luo, Z. Chen, X. Niu, X. Zhang, J. Lu, R. Kumar, J. Jiang, H. Liu, X. Guo, *et al.*, “Microscopic degradation in formamidinium-cesium lead iodide perovskite solar cells under operational stressors,” *Joule*, vol. 4, no. 8, pp. 1743–1758, 2020.

[75] S. Draguta, O. Sharia, S. J. Yoon, M. C. Brennan, Y. V. Morozov, J. S. Manser, P. V. Kamat, W. F. Schneider, and M. Kuno, "Rationalizing the light-induced phase separation of mixed halide organic–inorganic perovskites," *Nature communications*, vol. 8, no. 1, pp. 1–8, 2017.

[76] Wikipedia, "Diffusion current." `https://en.wikipedia.org/wiki/Diffusion_current`, Last accessed on 2022-05-27.

[77] M. Burgelman, P. Nollet, and S. Degrave, "Modelling polycrystalline semiconductor solar cells," *Thin solid films*, vol. 361, pp. 527–532, 2000.

[78] Y. Bi, E. M. Hutter, Y. Fang, Q. Dong, J. Huang, and T. J. Savenije, "Charge carrier lifetimes exceeding 15 μs in methylammonium lead iodide single crystals," *The journal of physical chemistry letters*, vol. 7, no. 5, pp. 923–928, 2016.

[79] S. D. Stranks, G. E. Eperon, G. Grancini, C. Menelaou, M. J. Alcocer, T. Leijtens, L. M. Herz, A. Petrozza, and H. J. Snaith, "Electron-hole diffusion lengths exceeding 1 micrometer in an organometal trihalide perovskite absorber," *Science*, vol. 342, no. 6156, pp. 341–344, 2013.

[80] Q. Dong, Y. Fang, Y. Shao, P. Mulligan, J. Qiu, L. Cao, and J. Huang, "Electron-hole diffusion lengths¿ 175 μm in solution-grown ch3nh3pbi3 single crystals," *Science*, vol. 347, no. 6225, pp. 967–970, 2015.

[81] S. De Wolf, J. Holovsky, S.-J. Moon, P. Löper, B. Niesen, M. Ledinsky, F.-J. Haug, J.-H. Yum, and C. Ballif, "Organometallic halide perovskites: sharp optical absorption edge and its relation to photovoltaic performance," *The journal of physical chemistry letters*, vol. 5, no. 6, pp. 1035–1039, 2014.

[82] M. Green, E. Dunlop, J. Hohl-Ebinger, M. Yoshita, N. Kopidakis, and X. Hao, "Solar cell efficiency tables (version 57)," *Progress in photovoltaics: research and applications*, vol. 29, no. 1, pp. 3–15, 2021.

[83] G.-J. A. Wetzelaer, M. Scheepers, A. M. Sempere, C. Momblona, J. Ávila, and H. J. Bolink, "Trap-assisted non-radiative recombination in organic–inorganic perovskite solar cells," *Advanced Materials*, vol. 27, no. 11, pp. 1837–1841, 2015.

[84] A. Buin, P. Pietsch, J. Xu, O. Voznyy, A. H. Ip, R. Comin, and E. H. Sargent, "Materials processing routes to trap-free halide perovskites," *Nano letters*, vol. 14, no. 11, pp. 6281–6286, 2014.

[85] H. Tan, A. Jain, O. Voznyy, X. Lan, F. P. García de Arquer, J. Z. Fan, R. Quintero-Bermudez, M. Yuan, B. Zhang, Y. Zhao, *et al.*, "Efficient and stable solution-processed planar perovskite solar cells via contact passivation," *Science*, vol. 355, no. 6326, pp. 722–726, 2017.

[86] W. S. Yang, B.-W. Park, E. H. Jung, N. J. Jeon, Y. C. Kim, D. U. Lee, S. S. Shin, J. Seo, E. K. Kim, J. H. Noh, *et al.*, "Iodide management in formamidinium-lead-halide–based perovskite layers for efficient solar cells," *Science*, vol. 356, no. 6345, pp. 1376–1379, 2017.

[87] D. Bi, W. Tress, M. I. Dar, P. Gao, J. Luo, C. Renevier, K. Schenk, A. Abate, F. Giordano, J.-P. Correa Baena, *et al.*, "Efficient luminescent solar cells based on tailored mixed-cation perovskites," *Science advances*, vol. 2, no. 1, p. e1501170, 2016.

[88] Q. Jiang, Y. Zhao, X. Zhang, X. Yang, Y. Chen, Z. Chu, Q. Ye, X. Li, Z. Yin, and J. You, "Surface passivation of perovskite film for efficient solar cells," *Nature Photonics*, vol. 13, no. 7, pp. 460–466, 2019.

[89] M.-H. Li, H.-H. Yeh, Y.-H. Chiang, U.-S. Jeng, C.-J. Su, H.-W. Shiu, Y.-J. Hsu, N. Kosugi, T. Ohigashi, Y.-A. Chen, *et al.*, "Highly efficient 2d/3d hybrid perovskite solar cells via low-pressure vapor-assisted solution process," *Advanced Materials*, vol. 30, no. 30, p. 1801401, 2018.

[90] Q. Zhou, L. Liang, J. Hu, B. Cao, L. Yang, T. Wu, X. Li, B. Zhang, and P. Gao, "High-performance perovskite solar cells with enhanced environmental stability based on a (p-fc6h4c2h4nh3) 2 [pbi4] capping layer," *Advanced Energy Materials*, vol. 9, no. 12, p. 1802595, 2019.

[91] Y. Hu, E. M. Hutter, P. Rieder, I. Grill, J. Hanisch, M. F. Aygüler, A. G. Hufnagel, M. Handloser, T. Bein, A. Hartschuh, *et al.*, "Understanding the role of cesium and rubidium additives in perovskite solar cells: trap states, charge transport, and recombination," *Advanced Energy Materials*, vol. 8, no. 16, p. 1703057, 2018.

[92] Z. Wang, Q. Lin, F. P. Chmiel, N. Sakai, L. M. Herz, and H. J. Snaith, "Efficient ambient-air-stable solar cells with 2d–3d heterostructured butylammonium-caesium-formamidinium lead halide perovskites," *Nature Energy*, vol. 2, no. 9, pp. 1–10, 2017.

[93] H. Min, M. Kim, S.-U. Lee, H. Kim, G. Kim, K. Choi, J. H. Lee, and S. I. Seok, "Efficient, stable solar cells by using inherent bandgap of α-phase formamidinium lead iodide," *Science*, vol. 366, no. 6466, pp. 749–753, 2019.

[94] I. Volovichev, G. Logvinov, O. Y. Titov, and Y. G. Gurevich, "Recombination and lifetimes of charge carriers in semiconductors," *Journal of Applied Physics*, vol. 95, no. 8, pp. 4494–4496, 2004.

[95] L. M. Herz, "Charge-carrier dynamics in organic-inorganic metal halide perovskites," *Annual review of physical chemistry*, vol. 67, pp. 65–89, 2016.

[96] M. B. Johnston and L. M. Herz, “Hybrid perovskites for photovoltaics: charge-carrier recombination, diffusion, and radiative efficiencies,” *Accounts of chemical research*, vol. 49, no. 1, pp. 146–154, 2016.

[97] J. M. Richter, M. Abdi-Jalebi, A. Sadhanala, M. Tabachnyk, J. P. Rivett, L. M. Pazos-Outón, K. C. Gödel, M. Price, F. Deschler, and R. H. Friend, “Enhancing photoluminescence yields in lead halide perovskites by photon recycling and light out-coupling,” *Nature communications*, vol. 7, no. 1, pp. 1–8, 2016.

[98] P.-W. Liang, C.-Y. Liao, C.-C. Chueh, F. Zuo, S. T. Williams, X.-K. Xin, J. Lin, and A. K.-Y. Jen, “Additive enhanced crystallization of solution-processed perovskite for highly efficient planar-heterojunction solar cells,” *Advanced materials*, vol. 26, no. 22, pp. 3748–3754, 2014.

[99] Q. Chen, H. Zhou, T.-B. Song, S. Luo, Z. Hong, H.-S. Duan, L. Dou, Y. Liu, and Y. Yang, “Controllable self-induced passivation of hybrid lead iodide perovskites toward high performance solar cells,” *Nano letters*, vol. 14, no. 7, pp. 4158–4163, 2014.

[100] X. Zheng, Y. Hou, C. Bao, J. Yin, F. Yuan, Z. Huang, K. Song, J. Liu, J. Troughton, N. Gasparini, *et al.*, “Managing grains and interfaces via ligand anchoring enables 22.3%-efficiency inverted perovskite solar cells,” *Nature Energy*, vol. 5, no. 2, pp. 131–140, 2020.

[101] T. J. Jacobsson, J.-P. Correa-Baena, E. Halvani Anaraki, B. Philippe, S. D. Stranks, M. E. Bouduban, W. Tress, K. Schenk, J. Teuscher, J.-E. Moser, *et al.*, “Unreacted pbi2 as a double-edged sword for enhancing the performance of perovskite solar cells,” *Journal of the American Chemical Society*, vol. 138, no. 32, pp. 10331–10343, 2016.

[102] Q. Jiang, Z. Chu, P. Wang, X. Yang, H. Liu, Y. Wang, Z. Yin, J. Wu, X. Zhang, and J. You, “Planar-structure perovskite solar cells with efficiency beyond 21%,” *Advanced materials*, vol. 29, no. 46, p. 1703852, 2017.

[103] Y. Rong, Y. Hu, A. Mei, H. Tan, M. I. Saidaminov, S. I. Seok, M. D. McGehee, E. H. Sargent, and H. Han, “Challenges for commercializing perovskite solar cells,” *Science*, vol. 361, no. 6408, p. eaat8235, 2018.

[104] N. J. Jeon, J. H. Noh, Y. C. Kim, W. S. Yang, S. Ryu, and S. I. Seok, “Solvent engineering for high-performance inorganic–organic hybrid perovskite solar cells,” *Nature materials*, vol. 13, no. 9, pp. 897–903, 2014.

[105] N. J. Jeon, J. H. Noh, W. S. Yang, Y. C. Kim, S. Ryu, J. Seo, and S. I. Seok, “Compositional engineering of perovskite materials for high-performance solar cells,” *Nature*, vol. 517, no. 7535, pp. 476–480, 2015.

[106] S. Mahesh, J. M. Ball, R. D. Oliver, D. P. McMeekin, P. K. Nayak, M. B. Johnston, and H. J. Snaith, "Revealing the origin of voltage loss in mixed-halide perovskite solar cells," *Energy & Environmental Science*, vol. 13, no. 1, pp. 258–267, 2020.

[107] D. J. Slotcavage, H. I. Karunadasa, and M. D. McGehee, "Light-induced phase segregation in halide-perovskite absorbers," *ACS Energy Letters*, vol. 1, no. 6, pp. 1199–1205, 2016.

[108] H.-S. Kim and A. Hagfeldt, "Photoinduced lattice symmetry enhancement in mixed hybrid perovskites and its beneficial effect on the recombination behavior," *Advanced Optical Materials*, vol. 7, no. 9, p. 1801512, 2019.

[109] H. Tsai, R. Asadpour, J.-C. Blancon, C. C. Stoumpos, O. Durand, J. W. Strzalka, B. Chen, R. Verduzco, P. M. Ajayan, S. Tretiak, *et al.*, "Light-induced lattice expansion leads to high-efficiency perovskite solar cells," *Science*, vol. 360, no. 6384, pp. 67–70, 2018.

[110] N. Rolston, R. Bennett-Kennett, L. T. Schelhas, J. M. Luther, J. A. Christians, J. J. Berry, and R. H. Dauskardt, "Comment on "light-induced lattice expansion leads to high-efficiency perovskite solar cells"," *Science*, vol. 368, no. 6488, p. eaay8691, 2020.

[111] X. Liu, Q. Han, Y. Liu, C. Xie, C. Yang, D. Niu, Y. Li, H. Wang, L. Xia, Y. Yuan, *et al.*, "Light-induced degradation and self-healing inside ch3nh3pbi3-based solar cells," *Applied Physics Letters*, vol. 116, no. 25, p. 253303, 2020.

[112] E. M. Hutter, L. A. Muscarella, F. Wittmann, J. Versluis, L. McGovern, H. J. Bakker, Y.-W. Woo, Y.-K. Jung, A. Walsh, and B. Ehrler, "Thermodynamic stabilization of mixed-halide perovskites against phase segregation," *Cell Reports Physical Science*, vol. 1, no. 8, p. 100120, 2020.

[113] L. A. Muscarella, E. M. Hutter, F. Wittmann, Y. W. Woo, Y.-K. Jung, L. McGovern, J. Versluis, A. Walsh, H. J. Bakker, and B. Ehrler, "Lattice compression increases the activation barrier for phase segregation in mixed-halide perovskites," *ACS energy letters*, vol. 5, no. 10, pp. 3152–3158, 2020.

[114] Y. Jiang, S.-C. Yang, Q. Jeangros, S. Pisoni, T. Moser, S. Buecheler, A. N. Tiwari, and F. Fu, "Mitigation of vacuum and illumination-induced degradation in perovskite solar cells by structure engineering," *Joule*, vol. 4, no. 5, pp. 1087–1103, 2020.

[115] S. Pratap, E. Keller, and P. Müller-Buschbaum, "Emergence of lead halide perovskite colloidal dispersions through aggregation and fragmentation: insights from the nanoscale to the mesoscale," *Nanoscale*, vol. 11, no. 8, pp. 3495–3499, 2019.

[116] K. Domanski, E. A. Alharbi, A. Hagfeldt, M. Grätzel, and W. Tress, “Systematic investigation of the impact of operation conditions on the degradation behaviour of perovskite solar cells,” *Nature Energy*, vol. 3, no. 1, pp. 61–67, 2018.

[117] B. Roose, K. Dey, Y.-H. Chiang, R. H. Friend, and S. D. Stranks, “Critical assessment of the use of excess lead iodide in lead halide perovskite solar cells,” *The Journal of Physical Chemistry Letters*, vol. 11, no. 16, pp. 6505–6512, 2020.

[118] R. E. Beal, N. Z. Hagström, J. Barrier, A. Gold-Parker, R. Prasanna, K. A. Bush, D. Passarello, L. T. Schelhas, K. Brüning, C. J. Tassone, *et al.*, “Structural origins of light-induced phase segregation in organic-inorganic halide perovskite photovoltaic materials,” *Matter*, vol. 2, no. 1, pp. 207–219, 2020.

[119] R. E. Reed-Hill, R. Abbaschian, and R. Abbaschian, *Physical metallurgy principles*, vol. 17. Van Nostrand New York, 1973.

[120] K. Lu, L. Lu, and S. Suresh, “Strengthening materials by engineering coherent internal boundaries at the nanoscale,” *science*, vol. 324, no. 5925, pp. 349–352, 2009.

[121] S. Jariwala, H. Sun, G. W. Adhyaksa, A. Lof, L. A. Muscarella, B. Ehrler, E. C. Garnett, and D. S. Ginger, “Local crystal misorientation influences non-radiative recombination in halide perovskites,” *Joule*, vol. 3, no. 12, pp. 3048–3060, 2019.

[122] Y.-H. Lin, N. Sakai, P. Da, J. Wu, H. C. Sansom, A. J. Ramadan, S. Mahesh, J. Liu, R. D. Oliver, J. Lim, *et al.*, “A piperidinium salt stabilizes efficient metal-halide perovskite solar cells,” *Science*, vol. 369, no. 6499, pp. 96–102, 2020.

[123] C. Bettles and M. Barnett, *Advances in wrought magnesium alloys: fundamentals of processing, properties and applications.* Elsevier, 2012.

[124] S. Brunauer, L. S. Deming, W. E. Deming, and E. Teller, “On a theory of the van der waals adsorption of gases,” *Journal of the American Chemical society*, vol. 62, no. 7, pp. 1723–1732, 1940.

[125] Z. Hu, Z. Liu, L. K. Ono, M. Jiang, S. He, D.-Y. Son, and Y. Qi, “The impact of atmosphere on energetics of lead halide perovskites,” *Advanced Energy Materials*, vol. 10, no. 24, p. 2000908, 2020.

[126] M. Ahmadi, E. S. Muckley, I. N. Ivanov, M. Lorenz, X. Li, O. Ovchinnikova, E. D. Lukosi, J. T. Tisdale, E. Blount, I. I. Kravchenko, *et al.*, “Environmental gating and galvanic effects in single crystals of organic–inorganic halide perovskites,” *ACS applied materials & interfaces*, vol. 11, no. 16, pp. 14722–14733, 2019.

[127] E. J. Juarez-Perez, R. S. Sanchez, L. Badia, G. Garcia-Belmonte, Y. S. Kang, I. Mora-Sero, and J. Bisquert, “Photoinduced giant dielectric constant in lead halide

perovskite solar cells," *The journal of physical chemistry letters*, vol. 5, no. 13, pp. 2390–2394, 2014.

[128] E. T. Hoke, D. J. Slotcavage, E. R. Dohner, A. R. Bowring, H. I. Karunadasa, and M. D. McGehee, "Reversible photo-induced trap formation in mixed-halide hybrid perovskites for photovoltaics," *Chemical Science*, vol. 6, no. 1, pp. 613–617, 2015.

[129] X. Wang, Y. Ling, X. Lian, Y. Xin, K. B. Dhungana, F. Perez-Orive, J. Knox, Z. Chen, Y. Zhou, D. Beery, *et al.*, "Suppressed phase separation of mixed-halide perovskites confined in endotaxial matrices," *Nature communications*, vol. 10, no. 1, pp. 1–7, 2019.

[130] C. Erkey, *Supercritical fluids and organometallic compounds: from recovery of trace metals to synthesis of nanostructured materials.* Elsevier, 2011.

[131] A. Alberti, I. Deretzis, G. Mannino, E. Smecca, F. Giannazzo, A. Listorti, S. Colella, S. Masi, and A. La Magna, "Nitrogen soaking promotes lattice recovery in polycrystalline hybrid perovskites," *Advanced Energy Materials*, vol. 9, no. 12, p. 1803450, 2019.

[132] J. P. C. Baena, L. Steier, W. Tress, M. Saliba, S. Neutzner, T. Matsui, F. Giordano, T. J. Jacobsson, A. R. S. Kandada, S. M. Zakeeruddin, *et al.*, "Highly efficient planar perovskite solar cells through band alignment engineering," *Energy & Environmental Science*, vol. 8, no. 10, pp. 2928–2934, 2015.

[133] P. Kaienburg, P. Hartnagel, B. E. Pieters, J. Yu, D. Grabowski, Z. Liu, J. Haddad, U. Rau, and T. Kirchartz, "How contact layers control shunting losses from pinholes in thin-film solar cells," *The Journal of Physical Chemistry C*, vol. 122, no. 48, pp. 27263–27272, 2018.

[134] A. Wakamiya, M. Endo, T. Sasamori, N. Tokitoh, Y. Ogomi, S. Hayase, and Y. Murata, "Reproducible fabrication of efficient perovskite-based solar cells: X-ray crystallographic studies on the formation of ch3nh3pbi3 layers," *Chemistry Letters*, vol. 43, no. 5, pp. 711–713, 2014.

[135] M. Matuchova, K. Žďánskỳ, M. Svatuška, J. Zavadil, and O. Prochazkova, "Electrical resistivity and photoluminescence of lead iodide crystals," *Chemical Papers*, vol. 61, no. 1, pp. 36–40, 2007.

[136] M. Matuchova, O. Prochazkova, J. Maixner, K. Zdansky, and J. Zavadil, "Influence of rare earth holmium on the properties of lead iodide," *physica status solidi (c)*, vol. 2, no. 4, pp. 1275–1279, 2005.

[137] Y. Zhang, S. Seo, S. Y. Lim, Y. Kim, S.-G. Kim, D.-K. Lee, S.-H. Lee, H. Shin, H. Cheong, and N.-G. Park, "Achieving reproducible and high-efficiency (¿ 21%)

perovskite solar cells with a presynthesized fapbi3 powder," *ACS Energy Letters*, vol. 5, no. 2, pp. 360–366, 2019.

[138] J. You, Y. Yang, Z. Hong, T.-B. Song, L. Meng, Y. Liu, C. Jiang, H. Zhou, W.-H. Chang, G. Li, *et al.*, "Moisture assisted perovskite film growth for high performance solar cells," *Applied Physics Letters*, vol. 105, no. 18, p. 183902, 2014.

[139] H. Jin, E. Debroye, M. Keshavarz, I. G. Scheblykin, M. B. Roeffaers, J. Hofkens, and J. A. Steele, "It's a trap! on the nature of localised states and charge trapping in lead halide perovskites," *Materials Horizons*, vol. 7, no. 2, pp. 397–410, 2020.

[140] J. S. Renny, L. L. Tomasevich, E. H. Tallmadge, and D. B. Collum, "Method of continuous variations: applications of job plots to the study of molecular associations in organometallic chemistry," *Angewandte Chemie International Edition*, vol. 52, no. 46, pp. 11998–12013, 2013.

[141] P. Tiwana, P. Parkinson, M. B. Johnston, H. J. Snaith, and L. M. Herz, "Ultrafast terahertz conductivity dynamics in mesoporous tio2: influence of dye sensitization and surface treatment in solid-state dye-sensitized solar cells," *The Journal of Physical Chemistry C*, vol. 114, no. 2, pp. 1365–1371, 2010.

[142] A. M. Ulatowski, A. D. Wright, B. Wenger, L. R. Buizza, S. G. Motti, H. J. Eggimann, K. J. Savill, J. Borchert, H. J. Snaith, M. B. Johnston, *et al.*, "Charge-carrier trapping dynamics in bismuth-doped thin films of mapbbr3 perovskite," *The Journal of Physical Chemistry Letters*, vol. 11, no. 9, pp. 3681–3688, 2020.

[143] L. M. Herz, "Charge-carrier mobilities in metal halide perovskites: fundamental mechanisms and limits," *ACS Energy Letters*, vol. 2, no. 7, pp. 1539–1548, 2017.

[144] V. M. Le Corre, E. A. Duijnstee, O. El Tambouli, J. M. Ball, H. J. Snaith, J. Lim, and L. J. A. Koster, "Revealing charge carrier mobility and defect densities in metal halide perovskites via space-charge-limited current measurements," *ACS energy letters*, vol. 6, no. 3, pp. 1087–1094, 2021.

[145] J. Huang, Y. Yuan, Y. Shao, and Y. Yan, "Understanding the physical properties of hybrid perovskites for photovoltaic applications," *Nature Reviews Materials*, vol. 2, no. 7, pp. 1–19, 2017.

List of publications

Publications related to the dissertation

- R. Guo, A. Buyruk, X. Jiang, W. Chen, L. K. Reb, M .A .Scheel, T .Ameri, P. Müller-Buschbaum
  Tailoring the orientation of perovskite crystals via adding two-dimensional polymorphs for perovskite solar cells
  JPhys Energy **2**, 034005 (2020)
- R. Guo, D. Han, W. Chen, L. Dai, K. J, Q. X, S. Li, L. K. Reb, M .A .Scheel, S. Pratap, N. Li, S. Yin, A. L. Oechsle, Tian. Xiao, S .Liang, C. L, Weindl, H. Ebert, N. Greenham, S. Stranks, R. Friend, P. Gao, M. Yuan, M. Schwartzkopf, S. V. Roth, P. Müller-Buschbaum
  Degradation mechanisms of perovskite solar cells under vacuum and one atmosphere of nitrogen
  Nat. Energy. **6.10**, 977-986 (2021)

Publications not related to the dissertation

- G. Sebastian, K. Amir, L. K. Reb, and Weindl, C. L, Weindl, R. Guo, S. Yin, K. S. Wienhold, W. Chen, T , Ameri, M. Schwartzkopf, S. V. Roth, P. Müller-Buschbaum
  Solvent Tuning of the Active Layer Morphology of Non-Fullerene Based Organic Solar Cells
  Solar RRL **1**, 2101084 (2022)
- X. Song, K. Zhang, R. Guo, K. Sun, Z. Zhou, S. Huang, H, Linus, M. Reus, J. Zhou, M. Schwartzkopf, S. V. Roth, W. Liu, Y. Liu, W. Zhou, P. Müller-Buschbaum
  Process-Aid Solid Engineering Triggers Delicately Modulation of Y-Series Non-Fullerene Acceptor for Efficient Organic Solar Cells
  Advanced Materials **3**, 2200907 (2022)

- M. A. Reus, L. K. Reb, A. F. Weinzierl, C. L, Weindl, R. Guo, T. Xiao, M. Schwartzkopf, A. Chumakov, S. V. Roth, P. Müller-Buschbaum
  Time-Resolved Orientation and Phase Analysis of Lead Halide Perovskite Film Annealing Probed by In Situ GIWAXS
  Advanced Optical Materials **6**, 2102722 (2022)
- F. Li, Y. Liu, G. Shi, W. Chen,R. Guo, D. Liu, Y. Zhang, Y. Wang, X. Meng, X. Zhang,Y. Lv, W. Deng, Q. Zhang, Y. Shi, Y. Chen, K. Wang, Q. Shen, Z. Liu, P. Müller-Buschbaum, W. Ma
  Matrix Manipulation of Directly-Synthesized PbS Quantum Dot Inks Enabled by Coordination Engineering
  Advanced Functional Materials **31**, 2104457 (2021)
- N. Li, R. Guo, W. Chen, V. Körstgens, J. E. Heger, S. Liang, C. J. Brett, M. A. Hossain, J. Zheng, P. S. Deimel, A. Buyruk, F. Allegretti, M. Schwartzkopf,J. G. C. Veinot, G. Schmitz, J. V. Barth, T. Ameri, S. V. Roth, P. Müller-Buschbaum
  Tailoring Ordered Mesoporous Titania Films via Introducing Germanium Nanocrystals for Enhanced Electron Transfer Photoanodes for Photovoltaic Applications
  Advanced Functional Materials **31**, 2102105 (2021)
- C. Ko, C. Henschel, G. P. Meledam, M. A. Schroer, R. Guo, L. Gaetani, P. Müller-Buschbaum, A. Laschewsky, C. M. Papadakis
  Co-nonsolvency effect in solutions of poly (methyl methacrylate)-b-poly (N-isopropylacrylamide) diblock copolymers in water/methanol mixtures
  Macromolecules **54**, 5825–5837 (2021)
- W. Chen, R. Guo, H. Tang, K. S. Wienhold, N. Li, Z. Jiang, J. Tang, X. Jiang, L. P. Kreuzer, H. Liu, M. Schwartzkopf, X. Sun, S. V. Roth, K. Wang, B. Xu, P. Müller-Buschbaum
  Operando structure degradation study of PbS quantum dot solar cells
  Energy & Environmental Science **14**, 3420–3429 (2021)
- S. Liang, W. Chen, S. Yin, S. J. Schaper, R. Guo, J. Drewes, N. Carstens, T. Strunskus, M. Gensch, M. Schwartzkopf, F. Faupel, S. V. Roth, Y. Cheng, P. Müller-Buschbaum
  Operando structure degradation study of PbS quantum dot solar cells
  ACS applied materials & interfaces **13**, 14728–14740 (2021)
- X. Song, L. Hou, R. Guo, Q. Wei, L. Yang, X. Jiang, S. Tu, A. Zhang, Z. Kan, W. Tang, G. Xing, P. Müller-Buschbaum
  Synergistic interplay between asymmetric backbone conformation, molecular aggregation, and charge-carrier dynamics in fused-ring electron acceptor-based bulk het-

erojunction solar cells
ACS applied materials & interfaces **13**, 2961–2970 (2021)

- H. Zhao, H. B. Naveed, B. Lin, X. Zhou, J. Yuan, K. Zhou, H. Wu, R. Guo, M. A. Scheel, A. Chumakov, S. V. Roth, Z. Tang, P. Müller-Buschbaum, W. Ma
Hot Hydrocarbon-Solvent Slot-Die Coating Enables High-Efficiency Organic Solar Cells with Temperature-Dependent Aggregation Behavior
Advanced materials **32**, 2002302 (2020)

- L. K. Reb, M. Böhmer, B. Predeschly, S. Grott, C. L. Weindl, G. I. Ivandekic, R. Guo, C. Drei*β*igacker, R. Gernhäuser, A. Meyer, P. Müller-Buschbaum, W. Ma
Perovskite and organic solar cells on a rocket flight
Joule **4**, 1880-1892 (2020)

- S. Yin, T. Tian, K. S. Wienhold, C. L. Weindl, R. Guo, M. Schwartzkopf, S. V. Roth, P. Müller-Buschbaum
Key factor study for amphiphilic block copolymer-templated mesoporous SnO_2 *thin film synthesis: Influence of solvent and catalyst*
Advanced materials interfaces **7**, 2001002 (2020)

- K. S. Wienhold, W. Chen, S. Yi, R. Guo, M. Schwartzkopf, S. V. Roth, P. Müller-Buschbaum
Following in Operando the Structure Evolution-Induced Degradation in Printed Organic Solar Cells with Nonfullerene Small Molecule Acceptor
Solar RRL **4**, 2000251 (2020)

- X. Tang, W. Chen, D. Wu, A. Gao, G. Li, J. Sun, K. Yi, Z. Wang, G. Pang, H. Yang, R. Guo, H. Liu, H. Zhong, M. Huang, R. Chen, P. Müller-Buschbaum, X. Sun, K. Wang
In Situ Growth of All-Inorganic Perovskite Single Crystal Arrays on Electron Transport Layer
Advanced Science **7**, 1902767 (2020)

- B. Lin, X. Zhou, H. Zhao, K. Zhou, K. Chen, H. Wu, K. Yi, R. Guo, M. A. Scheel, A. Chumakov, S. V. Roth, Y. Mao, L. Wang, Z. Tang, P. Müller-Buschbaum, W. Ma
Balancing the pre-aggregation and crystallization kinetics enables high efficiency slot-die coated organic solar cells with reduced non-radiative recombination losses
Energy & environmental science **13**, 2467–2479 (2020)

Conference talks

- R. Guo, D. Han, W. Chen, L. Dai, K. J, Q. X, S. Li, L. K. Reb, M .A .Scheel, S. Pratap, N. Li, S. Yin, A. L. Oechsle, Tian. Xiao, S .Liang, C. L, Weindl, H. Ebert, N. Greenham, S. Stranks, R. Friend, P. Gao, M. Yuan, M. Schwartzkopf, S. V. Roth, P. Müller-Buschbaum
  Degradation mechanisms of perovskite solar cells under vacuum and one atmosphere of nitrogen
  10th Soltech conference, 08 – 11 November 2021
- R. Guo, D. Han, W. Chen, L. Dai, K. J, Q. X, S. Li, L. K. Reb, M .A .Scheel, S. Pratap, N. Li, S. Yin, A. L. Oechsle, T. Xiao, S .Liang, C. L, Weindl, H. Ebert, N. Greenham, S. Stranks, R. Friend, P. Gao, M. Yuan, M. Schwartzkopf, S. V. Roth, P. Müller-Buschbaum
  Atmosphere Affecting Lattice and Degradation Mechanisms of High-Efficiency Perovskite Solar Cells
  MRS spring/fall meeting and exhibit, 23 November – 04 December 2020

Conference poster presentations

- R. Guo, D. Han, W. Chen, L. Dai, K. J, Q. X, S. Li, L. K. Reb, M .A .Scheel, S. Pratap, N. Li, S. Yin, A. L. Oechsle, Tian. Xiao, S .Liang, C. L, Weindl, H. Ebert, N. Greenham, S. Stranks, R. Friend, P. Gao, M. Yuan, M. Schwartzkopf, S. V. Roth, P. Müller-Buschbaum
  Degradation mechanisms of perovskite solar cells under vacuum and one atmosphere of nitrogen
  E-conversion meeting, 15 September – 16 September 2021
- R. Guo, D. Han, W. Chen, L. Dai, K. J, Q. X, S. Li, L. K. Reb, M .A .Scheel, S. Pratap, N. Li, S. Yin, A. L. Oechsle, Tian. Xiao, S .Liang, C. L, Weindl, H. Ebert, N. Greenham, S. Stranks, R. Friend, P. Gao, M. Yuan, M. Schwartzkopf, S. V. Roth, P. Müller-Buschbaum
  Degradation mechanisms of perovskite solar cells under vacuum and one atmosphere of nitrogen
  11th Energy Colloquium of the Munich School of Engineering, 28 July – 29 July 2021
- R. Guo, D. Han, W. Chen, L. Dai, K. J, Q. X, S. Li, L. K. Reb, M .A .Scheel, S. Pratap, N. Li, S. Yin, A. L. Oechsle, T. XiaO, S .Liang, C. L, Weindl, H. Ebert, N. Greenham, S. Stranks, R. Friend, P. Gao, M. Yuan, M. Schwartzkopf, S. V. Roth, P. Müller-Buschbaum

Degradation mechanisms of perovskite solar cells under vacuum and one atmosphere of nitrogen
MLZ User Meeting, 07 – 08 December 2021

- R. Guo, D. Han, W. Chen, L. Dai, K. J, Q. X, S. Li, L. K. Reb, M .A .Scheel, S. Pratap, N. Li, S. Yin, A. L. Oechsle, Tian. Xiao, S .Liang, C. L, Weindl, H. Ebert, N. Greenham, S. Stranks, R. Friend, P. Gao, M. Yuan, M. Schwartzkopf, S. V. Roth, P. Müller-Buschbaum
  Atmosphere Affecting Lattice and Degradation Mechanisms of High-Efficiency Perovskite Solar Cells
  The ninth international SolTech conference, 05 October – 08 October 2020
- R. Guo, D. Han, W. Chen, L. Dai, K. J, Q. X, S. Li, L. K. Reb, M .A .Scheel, S. Pratap, N. Li, S. Yin, A. L. Oechsle, T. XiaO, S .Liang, C. L, Weindl, H. Ebert, N. Greenham, S. Stranks, R. Friend, P. Gao, M. Yuan, M. Schwartzkopf, S. V. Roth, P. Müller-Buschbaum
  Atmosphere Affecting Lattice and Degradation Mechanisms of High-Efficiency Perovskite Solar Cells
  MLZ User Meeting, 08 – 09 December 2020
- R. Guo, W. Chen, L. K. Reb, S. Yin, K. Wienhold, B. Predeschly, M. A. Scheel, P. Müller-Buschbaum
  Do different device architectures of perovskite solar cells have different degradation mechanisms?
  The 4th Internal Biennial Science Meeting of the MLZ, Grainau, 24 – 27 June 2019
- R. Guo, W. Chen, L. K. Reb, S. Yin, K. Wienhold, B. Predeschly, M. A. Scheel, P. Müller-Buschbaum
  Do different device architectures of perovskite solar cells have different degradation mechanisms?
  The 9th Energy Colloquium of the Munich School of Engineering, 1 August 2019
- R. Guo, W. Chen, L. K. Reb, S. Yin, K. Wienhold, B. Predeschly, M. A. Scheel, P. Müller-Buschbaum *Do different device architectures of perovskite solar cells have different degradation mechanisms?*
  E-conversion conference, Venice, September 9—13, 2019
- R. Guo, W. Chen, L. K. Reb, S. Yin, K. Wienhold, B. Predeschly, M. A. Scheel, P. Müller-Buschbaum
  What is the initial stage of degradation mechanism for perovskite solar cells?
  8th SolTech Conference, Nürnberg, 30 September – 2 October 2019
- R. Guo, W. Chen, L. K. Reb, S. Yin, K. Wienhold, B. Predeschly, M. A. Scheel, P. Müller-Buschbaum

What is the initial stage of degradation mechanism for perovskite solar cells?
Hot Carrier Dynamics in Advanced Concept Solar Cells, Garching, 28–29 October, 2019

- R. Guo, W. Chen, L. K. Reb, S. Yin, K. Wienhold, B. Predeschly, M. A. Scheel, P. Müller-Buschbaum
  What is the initial stage of degradation mechanism for perovskite solar cells?
  GISAXS Workshop 19, Hamburg, 20–22 November, 2019
- R. Guo, W. Chen, L. K. Reb, S. Yin, K. Wienhold, B. Predeschly, M. A. Scheel, P. Müller-Buschbaum
  What is the initial stage of degradation mechanism for perovskite solar cells?
  MLZ User Meeting, Munich, 10–12 December, 2019

Acknowledgments

I cannot believe that I am so close to the Dr. title. It may sound funny, the fortune teller whom my mom had asked should lose his job since he predicted that I cannot even get a bachelor's degree. Now, it is far away from the error bar of his prediction. Again, science triumphs over superstition!

First and foremost, I would like to appreciate Prof. Dr. Peter Müller-Buschbaum's lasting great support whenever I need one. Also, Peter really guides me so much to do decent scientific research and international collaboration. At the same time, he gives me the freedom to follow through with my ideas and projects. Last, I am really thankful for his time, patience and insightful input in training me as a nice scientist.

Secondly, I would like to thank Prof. Dr. Christine M. Papadakis to supervise my Ph.D. study and offer help always as my mentor.

I would like to thank our E13 group. Wei really taught me how to do science. Volker always helps me revise the beamtime proposal. Lennart and Manuel always help me improve the code and give me great beamline support, and I quite enjoy our discussion about science and life between us. Their effort for the regeneration of gloveboxes makes the solar cells keep great performance. Suzhe and Christian help me a lot in improving my drawing. Tianxiao, Nian and Yanan are my great office mates. Christina taught me a lot of knowledge about scattering. Julia is my best labmate and beamtime mate who made it a lot of fun for me. Xinyu, Tianfu and Shanshan measure a lot of samples with SEM and AFM for me. Senlin shared his card for letting me not be hungry when I do not have such a card. I also quite enjoy my hot-pot time with our Chinese colleagues. The fresh members, Kun, Yuxin, Huaying, Zhuijun, Tianle, Guangjiu, and Zerui also bring me many new views. Christopher is so clever and always can understand me. Last but not least, I am glad to thank all our past or present E13 members, make me become a better myself.

Apart from E13 members, I would also thank the selfless share of Saisai, Qiu, Nairong, and Zeyu for fabricating perovskite solar cells. Now I can fabricate all architectures of

devices with more than 20 %! Also, I really appreciate the support of Linjie and Kangyu for getting me involved with the photo-physics field, which could be my pursuit in my left life. I also thank for Alexander helping me measure THz data, and I thank for Prof. Peng Gao, Prof. Mingjian Yuan, Prof. Laura Herz for measuring different characterizations for me. What's more, I should give a big thanks to beamline scientists from P03. Prof. Dr. Stephan V. Roth, Dr. Matthias Schwartzkopf, Dr. Andrei Chumakov, Marc, Yusuf, Constantin and Benedikt always offer me valuable beamtime whenever I need one and this makes sure the success of my experiments.

I would thank Prof. Dr. Ian Sharp, Prof. Dr. David Egger and Prof. Dr. Peter Müller-Buschbaum, they carefully review this thesis and help me improve the quality of the thesis during the review process. Their serious attitude toward scientific research makes me quite impressed, and I will definitely treat them as role models for my following academic careers. I appreciate their great support for my graduation process.

My biggest thanks of all should go to my family. I quite love my family as they love me, and they always give me financial and spiritual support whenever I need it.

I especially thank my girlfriend, Prof. Sichong Chen, who always motivates me to improve myself and develop my scientific work. She is always super positive and creative about things which we meet, which encourages me to live positively always. I really appreciate the time we have experienced and the time we will experience in future.

Finally, I would like to thank for Chinese Scholarship Council for offering me scholarships to make it possible for me to pursue the knowledge boundary of human beings. Also, the finical support from Deutsche Forschungsgemeinschaft (DFG, German Research Foundation) via Germany´s Excellence Strategy – EXC 2089/1 – 390776260 (e-conversion) and TUM.solar in the context of the Bavarian Collaborative Research Project Solar Technologies Go Hybrid (SolTech) should be acknowledged.